Imperial College London
Department of Chemical Engineering and Chemical Technology

INTERFACIAL PROPERTIES OF RESERVOIR FLUIDS AND ROCKS

Xuesong Li

December 2012

Submitted in part fulfilment of the requirements for the degree of
Doctoral of Philosophy in Chemical Engineering and Chemical Technology
of Imperial College London
and the Diploma of Imperial College London

Declaration of Originality

I hereby declare that this thesis and the work reported herein was composed by and originated entirely from me. Information derived from the published and unpublished work of others has been acknowledged in the text and references are given in the list of sources.

20 July, 2013. London, UK

Xuesong Li

Contents

List of Figures

List of Tables

Acknowledgement

I would like to express my sincere thanks to my three supervisors, Professor J P Martin Trusler, Professor Geoffrey C Maitland and Dr. Edo Boek.

Martin's wide knowledge, sharp thinking and professorial skills added great value to this research. His scientific disposition and passion for study influenced me deeply, the most precious quality I have learned from him. Professor Maitland was always supportive, creating opportunities and encouraging me to improve and enjoy this adventure at Imperial. The numerical simulation carried out on this research wouldn't be possible without the guidance and support of Dr. Edo Boek. His positive attitude encouraged me to go further and deeper on this work.

This work was supported by QCCSRC Qatar Carbonates and Carbon Storage Research Centre and I would like to gratefully acknowledge their financial support.

The internship at Shell International B.V. could not be done without the effort of Dr. Holger Ott. I am undoubtedly grateful to him.

Many people have contributed directly, or indirectly, to the completion of this work: Mr. Gavin Barnes helped with the equipment setup and his fine mechanical skills; Dr. Macdonald Iain assisted me throughout my research experience as QCCSRC project manager; Dr. John Crawshaw and Dr. David Vega Maza always tried their best to give all possible help; and Dr. Apostolos Georgiadis, sharing his experience on experimental research and providing a truly worthy induction on interfacial tension properties.

Abstract

Interfacial phenomena between CO_2, brines or hydrocarbon, and carbonate rocks were investigated with the aim of understanding key aspects on CO_2 storage and enhanced oil recovery (EOR) in carbonate reservoirs.

The interfacial tensions between brines and CO_2 were studied systematically with variation of the salt type and concentration under conditions applicable to the field. The results of the study indicate that, for strong electrolytes, the interfacial tension increases linearly with the positive charge concentration. Empirical models have been developed that represent the results as a function of temperature, pressure and molality with the small absolute average relative deviation of about 2 %. The interfacial tension measured between brine and crude oils indicated that interfacial tension has a strong dependence on both the viscosity of crude oil and the salinity of the brine.

Molecular dynamics (MD) simulations of interfacial tension between water or brine and CO_2 were carried out to investigate microscopic interfacial phenomena and to further understand the dependence of interfacial tension on temperature, pressure, and brine salinity. The simulation results were consistent with the experimental data obtained in this study. In particular, the simulations showed that the interfacial tension is linearly dependent on the positive charge concentration for strong electrolytes, most likely due to desorption of ions on the interface between brine and CO_2.

The contact angle of brine and crude oil on carbonate rocks was measured at both ambient and reservoir conditions. The results indicate

that brine salinity has a strong effect on the wettability of the carbonate rock surface. This thesis provided the first attempt to explain the low salinity effect from the interactions between brine and rocks. Contact angle results and wettability index gathered from the NMR and Amott approaches measured on porous rocks were compared and found to be correlated in (crude oil + brine + calcite) systems at ambient condition.

Molecular dynamics simulations of contact angle were carried out to give a deeper understanding of the underlying mechanism of the effect of brine salinity on wettabilty. Together with the experimental evidence, it can be concluded that increasing the salinity of brine results in an increase of the interfacial tension between calcite and brine. This is the first attempt to simulate contact angles by IFT simulations.

Over all, interfacial phenomena between reservoir rocks and fluids were investigated by interfacial tension and contact angle measurement and by molecular simulation. Based on the wide range of experimental and simulation data obtained, this thesis provides a near complete understanding of the brine and CO_2 interfacial behaviour under reservoir conditions. The empirical models obtained can predict reliably essentially any interfacial tension between brine and CO_2 at reservoir conditions with given brine composition, temperature and pressure. MD simulations together with the experimental evidence, indicate that reducing the salinity of brine generally reduces the adhesion tension of crude oil in brine and calcite system. Thus proving that low salinity water flooding could potentially increase oil recovery from carbonate reservoir. More generally, low salinity aquifers are found to be more favourable for CO_2 trapping.

Chapter 1. Introduction

1.1 Enhanced oil recovery

The world demand for energy has increased progressively in the past 50 years, from 55 million barrels of oil equivalent per day (mboe/d) in 1960 to 227 mboe/d in 2008 [1]. This energy demand will continue to increase, as economies expand, the global population grows and living conditions across the world improve. By 2030, world energy demand is predicted to be more than 40% higher than it is today. In satisfying the world's energy need, case studies show fossil fuels playing the prominent role and remains over 80% throughout the period to 2030. Among Energy mix, oil's leading role will continue with its share above 30% [2].

Oil reservoirs are porous rocks containing oil and gas at high temperatures and pressures deep underground. For the primary production, around 5-20% of the oil can be produced from the field under its own nature mechanism [3]. The underground surplus pressure as a driven force brings oil to the surface. It can be generated by the displacement of connate water oil downward into the well, the expansion of the natural gas at the top of the reservoir, the expansion of gas initially dissolved in the crude oil, or the gravity drainage resulting from the movement of oil within the reservoir from the upper to the lower parts where the wells are located. After this natural reservoir drive diminishes, secondary recovery methods are applied to increase reservoir pressure. Typical techniques are mechanical pump and fluid (water or gas) injection. Typical recovery factor from water-flood operations is about 30%, depending on the properties of oil and the characteristics of the reservoir rock. However, on average, after this secondary recovery still at least 50% of the oil was left behind in the reservoir [4].

Interfacial properties which involve interfacial tension, contact angle and wettability between reservoir rocks and fluids are considered to be important factors that may cause 30% of the OOIP to be unrecoverable by solution gas drive or water flooding alone.

Improved recovery may be obtained by injecting carbon dioxide to displace and dissolve some of the remaining oil [5]. In general, it has been found that such a tertiary processes can enhance oil recovery by (8 to 16%) of the OOIP [6].

Designed water flooding, such as low salinity water or surfactant solutions flooding is another technique that can increases oil production from a reservoir through lowering the salinity of the injection water. It is part of an emerging Enhanced Oil Recovery (EOR) theme built on the notion that not only the physical properties of the injection water matter, but that also its (brine) chemical properties are of great importance for determining eventual oil recovery from a reservoir.

Interfacial properties are considered as underlying mechanism in the above process. Thus the understanding of different factors influencing the interfacial tension and contact angle among reservoir rocks and fluids are of key important.

1.1.1 CO_2 enhanced oil recovery

Further oil recovery can be obtained by injecting carbon dioxide (CO_2) to displace and dissolve the remaining oil [5]. The solvent characteristics of supercritical CO_2 have long been recognized. As a solvent, supercritical CO_2 is miscible with many crude oils, reducing its viscosity and surface tension, thereby allowing for easier displacement of residual crude oil that would not otherwise be recovered. Thermodynamically, CO_2 is said to be in a supercritical state when it exists at pressures and temperatures above its critical pressure of 7.38 MPa and critical temperature of 304.3

K, respectively. Injection of supercritical CO_2 was first identified as a potential means for improving oil recovery in aging fields in the early 1950s. Field tests conducted in the 1960s demonstrated the concept of CO_2 EOR. In 1972, the first commercial scale injection of CO_2 for EOR was initiated in the SACROC (Scurry Area Canyon Reef Operators Committee) Unit of the Kelly -Snyder field in West Texas. This project continues in operation today and is the world's largest CO_2 miscible flood EOR project both in terms of CO_2 injection volume and oil production [7]. Currently, more than 20,000 tons per day of CO_2 are delivered to the oil field for EOR projects over the world [8]. These injection projects have focused on oil with densities between (711–855) $kg \cdot m^{-3}$, and reservoir depths from (760 to 3700) m [3,4]. Along with these projects, extensive research has been focused on the mixtures of CO_2, H_2O, brines, and various oils. Interfacial phenomena play a very important role for oil recovery. These has been emphasized since the first attempts using CO_2 on IOR [6].

In the CO_2-EOR processes, both the relative permeabilities of oil and CO_2 and the residual oil saturation can be related to the oil-CO_2 and brine-CO_2 interfacial tensions through a dimensionless number which compares either the capillary and viscous forces in horizontal displacement processes, or the capillary and buoyancy forces in gravity drainage processes [9-11]. Although there have been some studies of the effects of IFT in oil-CO_2 and water-CO_2 systems on the relative permeabilities in the CO_2 flooding process [12-17], there are insufficient data available in the literature for analyzing the effects of IFT between oil, CO_2 and brine on the CO_2-EOR process. It has been found that the viscosity of an oil-brine system is significantly reduced when CO_2 is injected into an oil reservoir at a high reservoir pressure [18, 19]. The reduced interfacial tension alters the viscous force–capillary force balance and thus lowers the residual oil saturation. Finally, the low

viscosity of supercritical CO_2 puts severe limits on the efficiency of both carbon storage and CO_2-EOR as the sweep efficiency is often reduced due to channelling and fingering effects, associated with reservoir heterogeneity [20]. Therefore, it is of fundamental and practical importance to study the detailed effects of the viscous and capillary forces on various CO_2 flooding processes.

1.1.2 Low salinity water flooding as an EOR technique

Water flooding as a technique for oil recovery has been applied for decades, which increase oil production from a reservoir through the injection of water. But in recent years, increasing oil production by injection of designed water, also known as low salinity water, into a reservoir has recently attracted substantial attention from the oil producing community. It was seen as a highly cost-competitive approach compared to other conventional EOR methods [21]. Reviewing the literature, it can be seen large number of papers on low salinity water flooding studies since 2007, which reflects the increasing interest of this technique [22-25], injecting chemically modified water instead of seawater can lead to incremental oil recoveries.

At present, most of the low salinity water flooding experiments were focused on sandstones [12, 26-33]. Since sandstone reservoirs are always covered by clay, a lot of researches were actually done on clayey sandstone [34, 35], and some directly investigated the interaction between clay mineral and reservoir fluid [27, 28, 32-34, 36-40]. But the study on carbonate reservoir is comparability less well developed.

This ongoing activity seeks to understand the underling mechanism of the low-salinity effect. And the majority of them attribute the low salinity effect to the change of reservoir wettability. There is also field experience which has proved a wettability alteration by injecting low salinity water.

However, researchers have proposed different reasons to explain the change of wettability. Some of them [41-43] confirmed that the type of acid components in crude oil has a strong influence to the wettability on sandstone and silicate glass. Some authors said that the change of wettability is due to the ions exchange between H^+ in water and the cations in the mineral. Interestingly, different ions in low salinity water were found behaving differently in different investigations. There are also some authors investigated the wettability change at a microscopic scale, by measuring the atoms force between reservoir fluid and rocks, or scanning the surface charge or reservoir rocks [12, 26, 28, 43].

Just a few authors [44, 45] related the low salinity effect with the change of capillary pressure rather than wettability. The capillary pressure is determined by both the wettability of the solid surface and the interfacial tension between the fluids on certain porous medium.

1.2 Carbon dioxide capture and storage

According to Intergovernmental Panel on Climate Change (IPCC)'s fourth assessment report, human activities are the main cause of the global warming. The green house gas making the largest contribution from human activities is CO_2 [46]. The concentration of CO_2 in the atmosphere is increasing rapidly year by year. If this trend in global CO_2 emissions continues, the world will not be on a path towards stabilization of greenhouse gas concentrations.

Carbon dioxide capture and storage (CCS) has the potential to significantly reduce CO_2 emissions to atmosphere from power generation and some other industrial processes.

The general idea of CCS is to capture CO_2 from large point sources, such as fossil fuel power plants, fuel processing, and other industrial plant, compress it and then inject it into a suitable underground storage

site, where the CO_2 cannot be released back to the atmosphere. Possible locations for such geological sequestration include deep saline aquifers, unmineable coal seams, and depleted oil or gas reservoirs.

The fundamental trapping mechanisms for CO_2 sequestration in geological media is a combination of physical and geochemical trapping mechanisms. Physical trapping of CO_2 below low-permeability caprocks, such as very-low-permeability shale or salt beds, is the principal means to store CO_2 in geological formations. In some high latitude areas, shallow gas hydrates may conceivably act as a seal. Sedimentary basins have such closed, physically bound traps or structures, which are occupied mainly by saline water, oil and gas. Structural traps include those formed by folded or fractured rocks. In the longer term, significant quantities of CO_2 dissolve in the formation water and then migrate with the groundwater. Where the distance from the deep injection site to the end of the overlying impermeable formation is hundreds of kilometres, the time scale for fluid to reach the surface from the deep basin can be millions of year [47]. Carbon dioxide in the subsurface can undergo a sequence of geochemical interactions with the rock and formation water that will further increase storage capacity and effectiveness. First, when CO_2 dissolves in formation water, a process commonly called solubility trapping occurs. The primary benefit of solubility trapping is that once CO_2 is dissolved, it no longer exists as a separate phase, thereby eliminating the buoyant forces that drive it upwards. Next, it will form ionic species as the rock dissolves, accompanied by a rise in the pH. Finally, some fraction may be converted to stable carbonate minerals, the most permanent form of geological storage [48]. Mineral trapping is believed to be comparatively slow, potentially taking a thousand years or longer. Nevertheless, the permanence of mineral storage, combined with the potentially large storage capacity present in some geological settings, makes this a desirable feature of long-term storage.

1.3 Interfacial phenomena

1.3.1 Interfacial tension

An interface is the area which separates two phases (gas/liquid, liquid/liquid, gas/solid or liquid/solid) from each other.

Strictly speaking, surface tension which refers to the contractive tendency of the surface of a liquid that allows it to resist an external force is also interfacial tension between the liquid and its vapour phase.

Interface is a more general term than surface. Interfaces can also separate two immiscible liquids such as water and oil. These are called liquid-liquid interfaces. Solid-solid interfaces separate two solid phases [49].

At a microscopic scale, interface is not an infinitesimal sharp boundary in the directions of its normal, it has a certain thickness. For the liquid-gas interface, density decreases within a few molecular diameters from bulk liquid phase to the gas phase. Chang's [50] dynamic simulation results of *n*-tridecane showed this density change crossing the interface, see Figure 1. The density and the orientation of the molecules are two parameters most used to define the thickness of an interface.

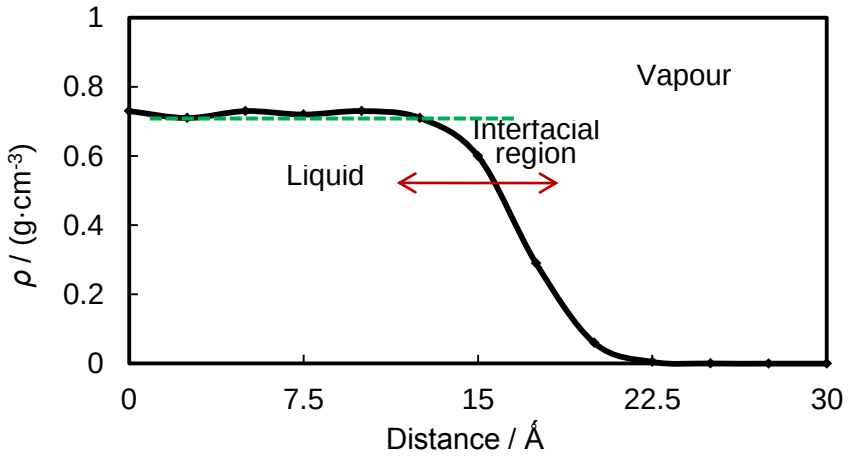

Figure 1. Local density profile of n-tridecane melt film from molecular dynamics simulation of the EA model at 300 K [51]

When two different phases are in contact with each other the molecules at the interface experience an imbalance of forces. Interfacial tension is the cohesive energy present at an interface arising from the imbalance of forces between molecules at an interface.

1.3.2 Contact angle and Wettability

When a drop of a liquid is placed on a surface, contact angle α is the angle under which the liquid L meets the surface S, see Figure 2. The extent of partial wetting of the solid by the value of θ, the better the wetting, the lower the contact angle. Usually wetting means $\theta < 90°$ and non-wetting indicates that $\theta > 90°$.

Young's equation relates the contact angle to the interfacial tensions. In Figure 2, S represents solid phase, while A and B are tow immiscible or partly miscible fluid in contact with the surface of solid S. γ_{SA}, , γ_{SB} and γ_{AB}, are three interfacial tensions on the contact line.

$$\gamma_{SA} = \gamma_{SB} + \gamma_{AB} \cos\theta \tag{1.1}$$

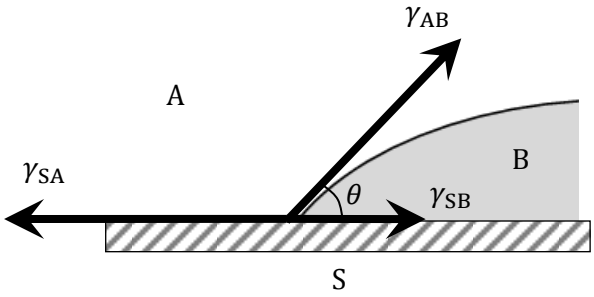

Figure 2. Contact angle for a drop on a horizontal surface

In this equation, only γ_{AB} is measureable. But the interfacial tension between solid and other fluid can't be measured experimentally. Term $\gamma_{AB} \cdot \cos\theta$ is the adhesion tension of fluid B on S in fluid A.

The affinity of a solid to contact one liquid or gas, known as the wetting phase, rather than another is called wettability.

The force that exists between like molecules of a particular liquid is called cohesion. It produces the phenomenon known as surface tension. When an attractive force exists between two unlike materials, such as a liquid and a solid container, the attractive force is known as adhesion. If the adhesive force between the liquid and solid is greater than the cohesive force within the liquid, the liquid is said to wet the surface. In cases where the cohesive force is greater than adhesion, the liquid is said to be non wetting.

In oil reservoir, rocks can be water-wet, oil-wet or intermediate-wet. See Figure 3, the cartoons of typical water-wet and oil wet conditions in porous rocks.

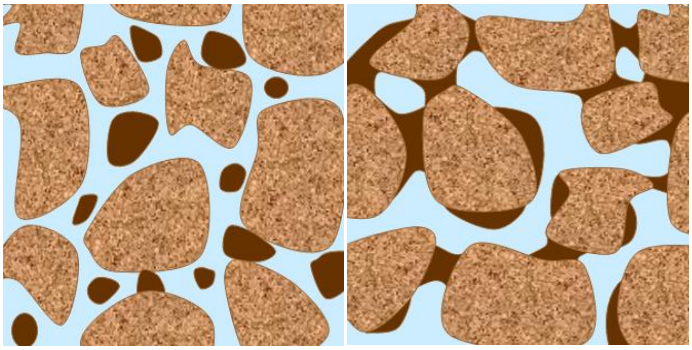

Figure 3. Wetting behaviour of oil reservoir
left: water wet; right: oil wet

Reservoir wetting preference can be determined by measuring the contact angle of crude oil and formation water on silica or calcite crystals or by measuring the characteristics of core plugs in either an Amott imbibition test or a USBM test, and nuclear magnetic resonance (NMR).

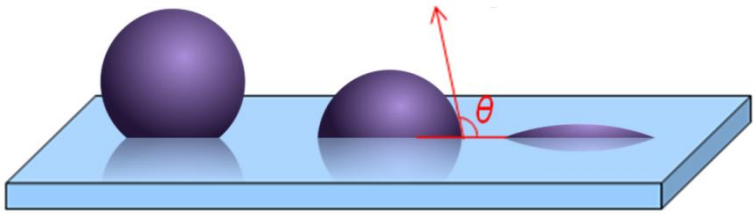

Figure 4. Contact angle measurements on a flat surface

Wettability affects relative permeability, electrical properties, nuclear magnetic resonance relaxation times and saturation profiles in the reservoir. The wetting state impacts water flooding and aquifer encroachment into a reservoir.

1.3.3 Capillary pressure

Capillarity, also known as capillary action, is the tendency of a liquid to rise in a narrow tube or to be drawn into small openings. This is a result of the intermolecular attraction within the liquid and solid materials. A familiar example of capillary actions is the tendency of a tissue to absorbs a liquid by drawing it into the narrow openings between the fibers. J.S. Rowlinson explained capillarity and surface phenomena from

a molecular view point in his book [52]. It is the difference in pressure across the interface between two immiscible fluids which is defined as,

$$p_c = p_{\text{non–wetting phase}} - p_{\text{wetting phase}} \tag{1.2}$$

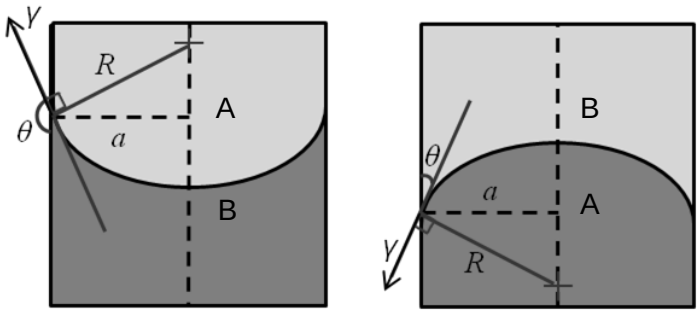

(a) (b)

Figure 5 Capillary pressures at different wetting conditions
(a), fluid B is the wetting phase; (b) fluid A is the wetting phase

The Young-Lapace equation [53] states that this pressure difference is proportional to the interfacial tension, γ, and inversely proportional to the effective radius, a, of the interface, it also depends on the wetting angle, θ, of the liquid on the surface of the capillary. As illustrated in Figure 5, capillary pressure is balanced with the interfacial tension act on the circular cross section with radius a. This relation can be written as the equation below,

$$p_c \cdot \pi a^2 = \gamma \cos\theta \cdot 2\pi a \tag{1.3}$$

Or written as,

$$p_c = \frac{2\gamma \cos\theta}{a} \tag{1.4}$$

The equation for capillary pressure is only valid under capillary equilibrium, which means that there cannot be any flowing phases. In porous media, such as porous rocks, capillary pressure is the force

necessary to squeeze a hydrocarbon droplet through a pore throat and is higher for smaller pore diameter. The expression for the capillary pressure remains as Eq. (1.4). However, the quantities p_{c} , $p_{\mathrm{non-wetting\,phase}}$ and $p_{\mathrm{wetting\,phase}}$ are obtained by averaging these quantities within the pore space of the medium in either a statistical manner or using the volume averaging method.

The Brooks-Corey correlation [54] for capillary pressure is defined as,

$$p_c = cS_w^{-a} \tag{1.5}$$

Where c is the entry capillary pressure, $1/a$ is the pore-size distribution index and S_{w} is the normalized water saturation.

The combination of the adhesive forces and the interfacial tension that arises from cohesion produces the phenomenon of capillarity.

In CO_2 EOR and low salinity water flooding processes, residual oil saturation is related to the wettability of the oil reservoir. A correct evaluation of a reservoir's wetting behaviour is therefore critical. The success or failure of CO_2 sequestration in depleted oil reservoirs relates to the relative permeability of the formation to CO_2 and other reservoir fluids. Interfacial tension and contact angle are two key parameters which control the forces between the reservoir fluids and rocks and strongly influence the residual oil saturation and relative permeability. Therefore, the aim of this research was to investigate the interfacial tension between brine, CO_2 and crude oil, and the contact angle between these fluids and a carbonate mineral surface. The specific objectives of the research are as follows:

- Design and construct new corrosion-resistant experimental devices for high temperature and high pressure interfacial tension, contact angle, and saturated phase density measurements of reservoir fluids.

- Produce representative and reliably experimental data of interfacial tension and contact angle of CO_2, crude oils/hydrocarbons, brines and minerals under high temperatures and elevated pressures.
- Predict the interfacial tension of any (CO_2 + brine) systems with a large range of temperatures and pressures using universal models.
- Calculate interfacial tension of CO_2 and electrolytes and contact angle of CO_2 and electrolytes in contact with calcite minerals using molecular dynamic
- Compare different approaches for measuring the wettability of reservoir rocks.

Chapter 2. Theoretical background and literature review

2.1 Experimental measurement of IFT

Carbon storage and CO_2 enhanced oil recovery requires accurate estimate of the IFT between CO_2 and different reservoir brines under the range of reservoir temperature and pressure conditions [55, 56].

Interfacial tension measurement is actually the measure of the tendency of the interfacial area to become smaller. Thermodynamically, this tendency can be explained together with the change of Gibbs or Helmholtz energy of the system, interfacial tension is treated as the increase of the energy when the area of the interface under consideration is increased reversibly by an infinitesimal amount dA at constant temperature and composition, and at constant volume or constant pressure, respectively.

$$\gamma = \left(\frac{\partial G}{\partial A} \right)_{T,p,n_i} \quad \text{..... (2.1)}$$

Where *G* is Gibbs free energy, *n* is the composition and *A* is the area.

Or,

$$\gamma = \left(\frac{\partial F}{\partial A} \right)_{p,V,n_i} \quad \text{..... (2.2)}$$

Where *F* is Helmholtz free energy, *n* is the composition and *A* is the area.

Mechanically, the interfacial tension is the contractive force per unit length, perpendicular to the infinitesimal dS.

Theoretically, the thermodynamic interfacial tension and mechanical interfacial tension are equivalent at equilibrium. However, only low Deborah number (De , defined as the ratio of the relaxation time characterizing the time it takes for a material to adjust to applied stresses or deformations , and the characteristic time scale of an experiment (or a computer simulation) probing the response of the material. It incorporates both on the elasticity and viscosity of the material.) ($De \ll 1$), fluid has limited time to come to equilibrium, the values obtained at this time is equilibrium value $\gamma_{eq.}$. Accordingly, those values measured under non-equilibrium or dynamic conditions could be called static interfacial tension $\gamma_{non-eq.}$. For a given interface, when only relaxation of the interface takes place, γ must decrease, which in fact is $\gamma_{non-eq.}$ always bigger than $\gamma_{eq.}$. However, when the bulk phases also relax slowly or when the relaxation is determined by adsorption-desorption processed, γ may also increase [57]. This is why some measurements with the same method yield different values in the literature when different relaxation periods were applied. However, unlimitedly extending the relaxation time to achieve $\gamma_{eq.}$ is not suggested in practical experiment. This is because the impurities can lower the interfacial tension and the slow accumulation of such impurities caused the interfacial tension decrease slowly with time.

2.1.1 Overview of the methods for IFT measurement

Interfacial tension can be measured by a variety of methods. Most of the techniques are taken under static condition. But some researches aimed to study the dynamics itself, such as the rate of adsorption of surfactants, as reflected in the rate of decrease of the interfacial tension, dynamic measurement will be taken. Normally, experiments operate at low Deborah number are static measurement, such as the capillary rise method and the drop shape analysis method used in this research. Capillary rise techniques is one of the best method for measuring surface tension because experimental variables can be well controlled and very

precise result can be obtaind. Other method for the interfacial tension measurement on fluid and liquid are maximum bubble pressure [58] , drop weight method [59], potential gradient method [60], Wilhelmy plate method and Du Noüy ring method [61], spinning drop method[62], surface light scattering method [63], and measuring the force to detach the interfaces directly [59]. However, drop shape method is widely applied for the interfacial tension measurement under high temperature and high pressure conditions [64].

The measurement of the pressure dependence of interfacial tension requires a very accurate method due to the fact its value can be quite small [65]. Thus, drop shape method with high degree of accuracy, is used in this research.

2.1.2 Axisymmetric drop shape analysis-profile (ADSA-P)

The interfacial tension in drop shape method is obtained from the drop shape analysis. This technique requires only a small amount of liquid and no direct contact to the interface is required during the measurement. The procedure with operating well developed commercial software is comparatively convenient and efficient. For these reasons, ADSA is selected for the interfacial properties study under high temperatures and elevated pressures [58-60, 62, 66-76].

Commercial software and imaging systems are available for this technique. Interfacial tensions as low as 10^{-3} $mN \cdot m^{-1}$ can be measured under optimum conditions by this method. Both static and dynamic interfacial tension can be studied.

Young-Laplace equation is the essential theory basis of this method. It links the pressure difference crossing the interface with the shape of the droplet. With the help of introducing another potential difference to the

entire drop, such as the gravity, interfacial tension can be calculated with a stretched or squashed drop.

To derive the equation of Young and Laplace we consider a small part of a liquid surface. See Figure 6. First, we pick a point X and draw a line around it with is characterized by the fact that all points on that line are the same distance d away from X. if the liquid surface is planar, this would be a flat circle. On this line we take two cuts that are perpendicular to each other (AXB and CXD).

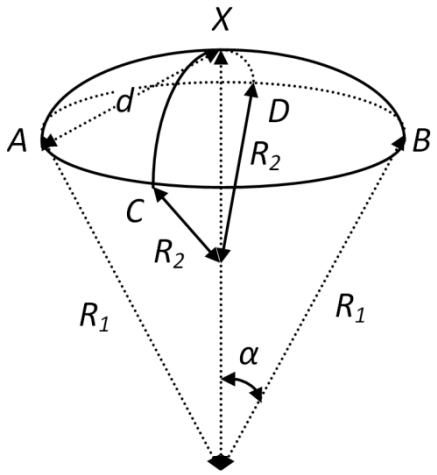

Figure 6. Diagram for deriving the Young-Laplace equation

Consider in B a small segment on the line of length dl, the surface tension pulls with a force γdl. The vertical force on that segment is $\gamma dl \sin\alpha$. For small surface areas (and small α) we have $\sin\alpha \approx d/R_1$ where R_1 is the radius of curvature along AXB. The vertical force component is,

$$\gamma \cdot dl \cdot \frac{d}{R_1} \tag{2.3}$$

The sum of the four vertical components at points A, B, C, and D is

$$\gamma \cdot dl \cdot \left(\frac{2d}{R_1} + \frac{2d}{R_2} \right) = \gamma \cdot dl \cdot 2d \cdot \left(\frac{1}{R_1} + \frac{1}{R_2} \right) \tag{2.4}$$

This expression is independent of the absolute orientation of AB and CD. Integration over the borderline (only 90° rotation of the four segments) gives the total vertical force, caused by the surface tension:

$$\pi d^2 \cdot \gamma \cdot \left(\frac{1}{R_1} + \frac{1}{R_2} \right) \tag{2.5}$$

In equilibrium, this downward force must be compensated by an equal force in the opposite direction. This upward force is caused by an increased pressure Δp on the concave side of $\pi d^2 \Delta p$ .Equating both forces leads to

$$\Delta p \cdot \pi d^2 = \pi d^2 \cdot \gamma \cdot \left(\frac{1}{R_1} + \frac{1}{R_2} \right) \Rightarrow \Delta p = \gamma \cdot \left(\frac{1}{R_1} + \frac{1}{R_2} \right) \tag{2.6}$$

These considerations are valid for any small part of the liquid surface. Since the part is arbitrary the Young-Laplace equation must be valid everywhere.

Mathematically, the integration of the Laplace equation is straightforward only for spherical menisci, i.e., one of the principal curvatures is equal to zero. For a general irregular meniscus, mathematical analysis would be very difficult. For the special case of axisymmetric drops, such as the sessile drop and pendant drops, numerical procedures have been devised.

The earliest efforts in the analysis of axisymmetric drops were those of Bashforth and Adams in 1883 [77]. The interfacial tension and contact angle of and actual drop were gained after comparing with the tabulated profiles. Hartland and Hartley developed a computer program to integrate

appropriate form of the Laplace equation and presented the results in tables [78]. Maze and Burnet developed a more satisfactory scheme for the determination of interfacial tension from the shape of sessile drops [79, 80]. Rotenberg *et al*. developed a technique, called Axisymmetric Drop Shape Analysis-Profile (ADSA_P) which superior to the above mentioned methods and does not suffer from their deficiencies [79]. Cheng *et al*. automated the methodology by means of digital image acquisition and image analysis. The drop profiles were extracted from pictures of pendant or sessile drops acquired from a video camera which attached to a computer [55]. The interfacial tensions were calculated from the above mentioned profile with ADSA-P technique.

Several automatic commercial instruments are available under this technique [80]. They are from different manufacturers such as ADSA, AST, FTA, Krüss, Rame-Hart and Temco. The products from Rame-Hart were selected for this research after a comprehensive comparison on price, product function, efficiency, reliability and services. With advanced software from this manufacture, both interfacial tension and contact angle can be calculated automatically. For the measurement of contact angle, several different methods are selectable. The essential theory of the programme was detailed in two papers published by the same author Hansen [81, 82]. In the software, the surface tension is determined by two-step process. First, the size parameter R_0 and β are calculated from the drop profile, after which surface tension is calculated from these parameters by equation,

$$\gamma = \frac{\Delta\rho g R_0^2}{\beta} \tag{2.7}$$

$\Delta\rho$ is the density difference between the drop and the surrounding medium, g is the gravitational constant, R_0 is the radius of curvature at the drop apex, and β is the shape factor, as defined in Eq. (2.7). Based

on the author's knowledge, this method is first developed by Fordham [83] in 1938, by introducing a new ratio $\sigma = D_S/D_E$, Referring to the lengths and angles defined in Figure 7. Fordham has compared this new ratio σ on different type of and expressed that this shape ration, σ, can be used as the shape factor describing different drop's profiles. He has also tabulated the $\beta - \sigma$ function for pendant drops, see Appendix A.

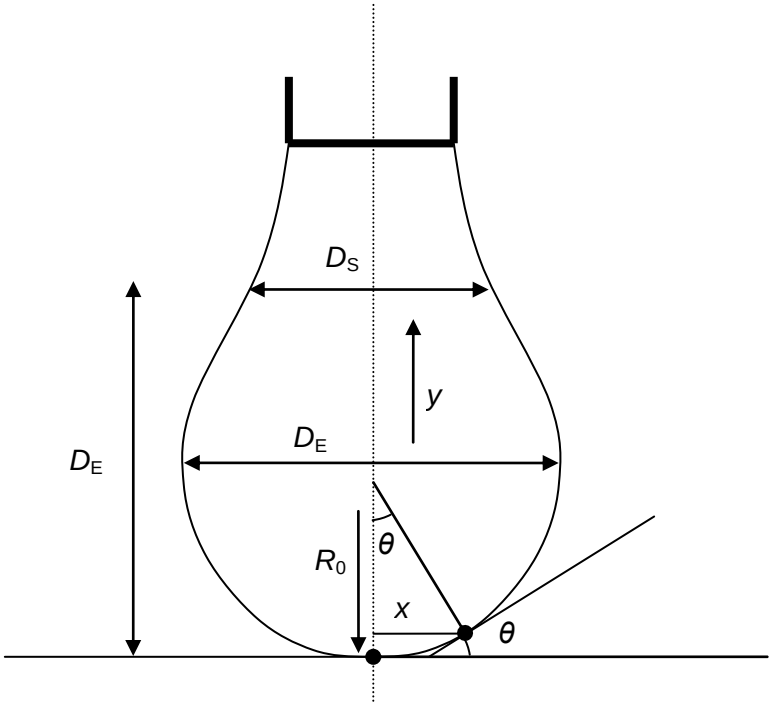

Figure 7. Profile of a pendant drop showing the co-ordinates
R_0 is the radius of curvature at the apex O, while s is the arc length between O and the point P; and y and x are respectively the vertical and horizontal co-ordinates relative to an origin at O

Compared with Fordham's second order polynomial, Hansen improved upon the method by using polynomial regression analysis on σ-data produced form theoretical profiles, which are (2.7), (2.8) and (2.9) three dimensionless equations,

$$\frac{d\theta}{dS} = 2 - \beta Y - \frac{\sin\theta}{X} \tag{2.8}$$

Together with the relations

$$\frac{dX}{dS} = \cos\theta \tag{2.9}$$

and

$$\frac{dY}{dS} = \sin\theta \tag{2.10}$$

where $X = x/R_0$, $Y = y/R_0$, $S = s/R_0$ are dimensionless co-ordinates of a point P on the profile of the drop. A calculation based on these equations has been done by means of Kutta-Merson [84] numerical integration algorithm with automatic step length adjustment. A large number of theoretical dimensionless profiles were calculated for the whole possible β range, from -0.55 to 10^{20}. The final equation was written as below,

$$\beta = 0.12836 + 0.7577\sigma - 1.7713\sigma^2 + 0.5426\sigma^3 \tag{2.11}$$

At the mean time, another equation for $D_E/2R_0$ was found by the same numerical method

$$\frac{D_E}{2R_0} = 0.9987 + 0.1971\beta - 0.0734\beta^2 + 0.34708\beta^3 \tag{2.12}$$

For pendant drops too short to determine D_S and for all sessile drops, drop height value "*H*" was introduced and $R = D_E/2$, with the method similar with above, interfacial tension could be writen in another form,

$$\gamma = \Delta\rho g H^2 / B \tag{2.13}$$

Here, $\Delta\rho$ is the density difference between the drop and the surrounding medium, and g is the gravitational acceleration. In the analysis, the task is to find by trial or otherwise the values of R_0 and β that best match the experimental drop profile; then subject to a given value of $\Delta\rho$ the interfacial tension γ is obtained from Eq. (2.11).

Introduce another ratio $\xi = H/R$, and *B* can be written as,

$$B = \beta \times \left(\frac{H}{R_0} \right)^2 = f(\xi) \tag{2.14}$$

Also the dimensionless ratio H/R_0 will be a function of ξ, and it could be written,

$$\frac{H}{R_0} = g(\xi) \tag{2.15}$$

Then we can get,

$$\beta = \frac{f(\xi)}{g(\xi)^2} \tag{2.16}$$

If we write B as,

$$B = u(g(\xi))^2 = f(\xi) \tag{2.17}$$

Then β could be written as,

$$\beta = \frac{u(g(\xi))}{g(\xi)^2} \tag{2.18}$$

By computing $g(\xi)$, R_0 and β can be calculated. However, to determine this function, a large number of theoretical profiles need to be generated by numerical integration of the Young-Laplace equation. The detail of this process is explained in Hansen's paper published in 1993 [81].

2.2 Literature review of IFT measurement on reservoir fluids

2.2.1 IFT of oil/hydrocarbons and CO_2 system

IFT between oil and CO_2 under high pressure have been studied since the beginning of CO_2 EOR operations. Nagarajan's research group have

done a significant research on the IFTs between oil and CO_2 from 1985 to 1990 [85-89]. The experimental set-up wasn't presented. They have measured IFTs between various hydrocarbons and CO_2 up to 16 MPa, 373 K.

Yang *et al*. measured dynamic IFTs of reservoir brine sample and CO_2 to pressures of up to 31 MPa on two isotherms [18, 19, 90]. The authors showed a decrease of IFT with time that reaches a near plateau after approximately 100 s for both Crude oil/CO_2 brine/CO_2 systems. For the crude oil/brine and CO_2 system however, the value reached after approximately 100 to 200 s, did not seem to be stable but continued to decrease with a smaller rate. With respect to the density of the oil phase, it was assumed to be constant throughout the whole range of pressures while the density of CO_2 was assumed to be as of the pure compound.

Nobakht *et al*. in 2007 published his IFTs of oil samples from the Weyburn oil field with CO_2 at pressures of up to 12 MPa and ambient temperatures, also using the pendant drop method. He showed that the IFT decreases from 17 $mN \cdot m^{-1}$ to 2 $mN \cdot m^{-1}$ linearly with increasing pressure from 0 to 7 MP [91]. More recently, Georgiadis *et al*. published his measurement on CO_2 and n-decane system using pendent drop method [92].

In this study, the interfacial tensions of brines and CO_2 were studied systematically with large variation of salt type and concentration under conditions applicable to the field. The measurements were made at temperatures between (298 and 473) K and pressures up to 50 MPa by means of imaging a pendant drop of CO_2-saturated brine surrounded by a water-saturated CO_2 phase.

2.2.2 IFT of brine/water and CO_2 system

Examination of the literature shows that the IFT of (CO_2 + water) has been measured at pressures up to 60 MPa and temperatures up to 383 K [93-96], and various factors affecting the accuracy of the measurements have been discussed by Georgiadis *et al*. [97]. However, the IFT between CO_2 and brine at high temperatures and pressures has been studied by only a few authors.

Bachu *et al*. and Yang *et al*. [98-100] have measured the IFT of CO_2 against synthetic formation brines, having salinities of up to 334010 $mg \cdot L^{-1}$, at temperatures up to 398 K and pressures up to 27 MPa. Their results show that IFT increases with increasing salinity and decreasing pressure, but a complex dependence of IFT on temperature was found.

The interfacial tension of H_2O/CO_2 system has been measured for temperatures of up to 345 K. and pressures of up to 21 MPa by Chun [93], Park [101] and Hebach [102]. The first two used the capillary rise method while Hebach used the pendant drop method.

Aggelopoulos *et al*. have performed IFT measurements for CO_2 with brines containing NaCl and/or $CaCl_2$ at $p \leq 25$MPa at temperatures of (300, 344 and 373) K for with total salt molality of (0.09 to 3.0) $mol \cdot kg^{-1}$ [103]. They concluded that, at constant temperature and pressure, the IFT increases linearly with the molality of each salt present in the brine.

Chalbaud *et al*. reported IFT measurements between CO_2 and NaCl(aq) with pressure up to 25 MPa and temperature up to 393 K [104, 105]. In contrast with the results of other authors, the IFT data of Chalbaud *et al*. shows a different dependence on pressure: initially decreasing with increasing pressure but then reaching a plateau. However, these results also indicated a linear relationship between IFT and salt concentration when the other conditions are invariant.

Chiquet published his research on interfacial tension between CO_2 water and brine in 2007 [106]. This paper measured interfacial tension between 20 $g \cdot L^{-1}$ NaCl brine and CO_2 at 308 K, in a range of pressure (5-45) MPa.

Massoudi and King [107] have found that the IFT at 298 K for the brine-CO_2 system that indicated a linear relationship between the IFT and the molal concentration of NaCl (up to 5 M) for pressures up to 6 MPa. The $\partial\gamma/\mathrm{m}$ slope was near to 1.58. This work shows that the CO_2/brine IFT values are very close to those of the CO_2/pure water IFTs under similar T and p conditions. Also in this paper, the author noted that the increase of IFT with salinity is fairly independent of pressure and reflects the increase in brine surface tension with salinity at ambient pressure, i.e. with no CO_2 present.

The effect of salinity (type of ions, salt concentration) on water surface tension under ambient conditions is documented in the literature [108, 109]. The presence of salts in brine increases the interfacial tension compared to the pure water case at the same pressure and temperature. The explanation in the reference is that cations have negative affinity for the gas–liquid interface hence they are accumulated in the bulk solution. Water molecules at the interface are attracted by cation solvation towards aqueous bulk phase. This attraction increases along with the concentration of cations and as the ratio of cation charges to cation surface area increases.

To summarize the literature, measurement of IFT between brine and CO_2 under conditions of elevated pressure has been carried out on only a few different salt solutions. The available data are scattered and in some cases contradictory. Thus additional high accuracy measurements would be useful in order to clarify the situation.

2.2.3 IFT of brine/water, oil/hydrocarbons and CO_2 system

As discussed above, there are large gaps in the literature relating to IFTs between brine and the mixture of supercritical CO_2 and hydrocarbons or crude oil under high temperature and high pressure. The representative research could be find are Young [96] and Jaeger's work [15].

Young has measured the IFT between crude oil, CO_2 and brine under reservoir condition, pressures from (0.1 to 31.4) MPa and two temperatures, (300 and 331) K, with the ADSA method in 2005. Both dynamic and equilibrium interfacial tensions were discussed in his research. It's expressed in this paper that the measured dynamic interfacial tensions quickly decrease to constant values at different pressures and two constant temperatures. He explained the reason of dynamic interfacial tension reduction of CO_2 and brine as the adsorption of CO_2 molecules and the reorientation of water molecules at the pendant brine drop surface. For the crude oil CO_2 system, the dynamic interfacial tension reduction is mainly due to the dissolution of CO_2 into the crude oil. In addition, for the crude oil reservoir brine system, he said that the dynamic interfacial tension reduction is primarily caused by the natural surfactants and the generated surfactants in the brine phase due to possible chemical reactions between the crude oil and the reservoir brine. And for the crude oil reservoir brine CO_2 system, he believed that the dissolution of CO_2 into the crude oil is an additional factor to reduce the dynamic interfacial tension. It is also found that for both the reservoir brine CO_2 system and the crude oil CO_2 system the equilibrium interfacial tension is reduced as the pressure increases, whereas it increases as the temperature increases. This is attributed to higher CO_2 solubility at a higher pressure but lower CO_2 solubility at a higher temperature. For the crude oil reservoir brine system and the crude oil reservoir brine CO_2 system. However, he indicated that the equilibrium interfacial tensions remain almost constant at different pressures, whereas they slightly

decrease as the temperature increases. Furthermore, in comparison with the interfacial tension data for the crude oil reservoir brine system at the same pressure and temperature, the equilibrium interfacial tension is reduced if CO_2 is introduced into the crude oil reservoir brine system. The equilibrium interfacial tension of the crude oil reservoir brine CO_2 system is slightly lower at a higher pressure because more CO_2 dissolves into the brine and oil phases.

Jaeger studied the interfacial tension between brine and oil with the presence of CO_2 in 2010. His work was focused on the vanishing IFT between hydrocarbons and CO_2 by changing the pressure and temperature, and significant effect of CO_2 on the IFT between hydrocarbons and brine have been studied.

2.2.4 IFT of brine/water and oil/hydrocarbons system

Comparing with IFT between brine/water and CO_2, more publications can be found between brine/water and oil/hydrocarbons. It has been studied by different authors. In 1951, Michaels *et al*. has measured the interfacial tension between alkanes and water at pressure of up to 70 MPa an temperatures of up to 303 K using pendant drop method [110].

The equipment built by Harvery *et al*. in 1958 could measure IFT up to 137 MPa of pressure and 373 K of temperature between water and benzene. He used pendant drop method as well [111]. His results indicated that the interfacial tensions between benzene and water decreases regularly with increasing pressure at 348K and 368K.

Cai *et al*. studied the interfacial tensions of 10 normal alkane + water/brine and hydrocarbon mixture + water/brine systems using pendent drop instrument [112]. The temperature and pressure ranges are (298 to 353) K and (0.1 to 30) MPa, respectively. The effects of temperature, pressure, and salt content have been studied. His

conclusion is interfacial tensions between water/brine and oil are sensitive to temperature and salt concentration but weakly dependent on pressure and salt species.

Wiegand *et al*. measured the IFT of alkane and water up to a pressure of 300 MPa [113], it most likely was the highest pressure have been measured between alkane and water in the literature.

Susnar *et al*. used ADSA method to determine both the time and pressure dependences of interfacial tension for the pure n-decane-water system in the (0 to 35) MPa pressure range at a temperature around 298 K [114]. His results indicated that the interfacial tension and pressure's relationship is highly linear and that the coefficients are different under different temperatures.

The study by Gaonkar *et al*. focused on the effects of salt and temperature on the interfacial tension behaviours of soybean oil/water interface were investigated at ambient pressure and three different temperatures, 278, 293 and 323 K. He concluded that salt led to a considerable reduction in the IFT of a commercial soybean oil/water system [115]. The differences in the IFT in the absence and presence of salt increased with the temperature.

IFTs between oil and water with the adding of surfactant were studied by Aveyard *et al*. in 1984 [116]. The system he has measured exhibited ultra low interfacial tension between oil and water. He has presented a thermodynamic treatment of the tension variation and checked the conditions required for the minima.

Bartell *et al*. most likely is the first who measured the IFT between crude oil and brine [117, 118]. His results were published in 1928 and 1932. Different from the other authors, he developed the capillary tube method to measure the IFTS. Hocott *et al*. [119] used drop weight method to

measure the IFTs between oil and brine in 1939. The maximum pressure and temperature of his results are 27 MPa and 383 K. Freer *et al*. [120] used pendant drop method to measure dynamic IFTS between crude oil and brine but at ambient conditions. But the research was more focused on the time dependence IFTs. More recently, Ghannam *et al*. [121] publish his results of IFT measurement on different hydrocarbons and brines.

The object of this research is to investigate the dependence of IFT on temperature, pressure and salinity (including both salt type and concentration) over the range of conditions applicable to CO_2 storage in underground reservoirs. One objective is to arrive at a universal model, based on such experimental evidence, for calculating the IFT of any (CO_2 + brine) system.

2.3 Experimental measurement of contact angle

The wetting behaviour of crude-oil/brine/rock systems can have a dominant effect on processes by which oil is recovered from underground reservoirs. Consequently, knowledge of reservoir rocks' wetting behaviour is always needed. The direct approach to determining reservoir wettability is contact angle measurement. However contact angle could vary with a certain number of factors, such as the condition of solid surface, including the surface texture and roughness. The scale of the measurement may also be important: the microscopic and macroscopic contact angle on the same system could be different. The uncertainty by certain analysing approaches. Because of these requirement, the oil industry tend to determine the wettablity of reservoir rocks from other approaches, such as Ammot wettability index (WI), United States Bureau of Mines (USBM) wettability index, and nuclear magnetic resonance (NMR) wettability index. Nevertheless, these index which obtained from porous rock, are combined with other information, such as the permeability and the porosity of the rock samples, the

density of the fluids, the aging procedure and so on, thus difficult to quantify the wettability of the mineral.

In this thesis we applied both contact angle measurement and conventional wettability method, the NMR WI and the USBM WI, to investigate the wetting behaviour of carbonate rocks with low and high salinity brine. It was aimed to correlate the contact angle measured on ideal mineral surface and the wettability index obtained from porous rocks. Meanwhile understand the underlying mechanism of low salinity effect in EOR.

2.3.1 Overview of the methods for contact angle measurement

Contact angle as the most common way to identify solid surface wetting behaviour was widely used in differ area. The discussion of contact angle is always done together with wettability and adhesion. Good *et al*. have done a good review on the theory of contact angle in 1993 [122]. Their discussion is mainly focused on general pure liquids in contact with solid. Regarding experimental measurement of contact angle, the review published by Chau *et al*. compared different techniques which are suitable for mineral surface in 2009 [123]. Krishnan *et al*. have also gave an evaluation of different contact angle methods [124]. Depending on the condition of the solid surface, certain methods can be used, such as drop profile method, drop dimensions method, axisymmetric drop shape analysis, and Wilhelmy method for ideal flat surfaces; capillary rise method for both flat and non-ideal surface or particles; and axisymmetric drop shape analysis of the drop diameter for non ideal surfaces. Generally, the increase of accuracy and reduction of measuring scale result in an increment of investment and complexity of the experiment.

2.3.2 Drop shape analysis for contact angle measurement

The basic idea of drop shape analysis contact angle measurement is determination of the contact angle from the image of a drop on a flat

surface. During the experiment, a CCD image and a computer program are used to determine the contact line or baseline of the surface and the profile of the drop by analysing the grey level values of actual drop image pixels.

Then the imaged drop shape is adapted to fit a mathematical model which is then used to calculate the contact angle. There are several methods corresponding to different mathematical models that can be used for the calculation of contact angle by drop shape analysis. Either the complete drop shape, part of the drop shape or only the area of phase contact are evaluated. Commonly used methods are circle method, conic section method, polynomial method and Yang-Laplace method.

In the circle method, the drop contour is fitted to a segment of a circle. See Figure 8. The contact angle is calculated by fitting the contour to a circular segment function. The advantage of this method is that the result is not so much disturbed by the droplet injection needle remaining in the drop.

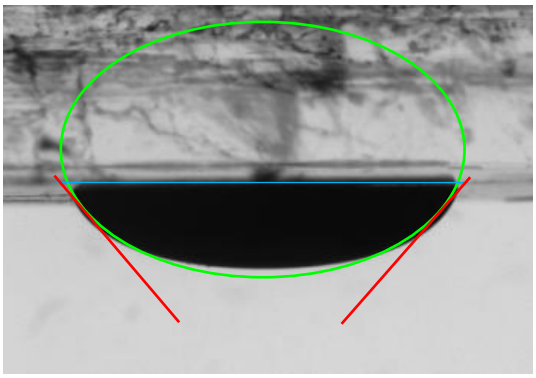

Figure 8. Contact angle calculation by circle fitting method

Another version of circle method is height and width method. See Figure 9. As it named, in this method the height and the width of the drop shape are determined. If the contour line enclosed by a rectangle is regarded as being a segment of a circle, then the contact angle can be calculated

from the height-width relationship of the enclosing rectangle. This method is suitable for small contact angle, because smaller drops are more similar to the theoretically assumed spherical cap form. However a complete drop profile is required. The drop height cannot be determined accurately when the injection needle disturbed the profile of the drop. A disadvantage of the height-width method is that instead of the whole contour only a few pixels at the point of inflection and at both sides are used. The measurement is therefore more susceptible to interference in these areas. Another disadvantage is that the same contact angle is obtained for both sides, thus it's not suitable for tilted baseline advancing and receding contact angle measurement.

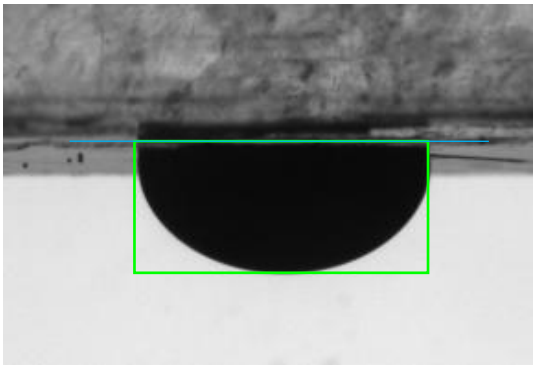

Figure 9. Contact angle calculation by height-width fitting method

The conic section method evaluates the complete drop shape. The profile of a sessile drop is then adapted to fit a general conic section equation. The derivative of this equation at the intersection point of the contour line with the baseline gives the slope at the three-phase contact line and therefore the contact angle.

The polynomial method only evaluates part of the profile of a sessile drop which lies near the baseline. So there is no geometrical requirement for the contour shape. The slope at the three-phase contact point at the baseline and from it the contact angle is determined using the iteratively

adapted parameters. This function is the result of numerous theoretical simulations. See Figure 10.

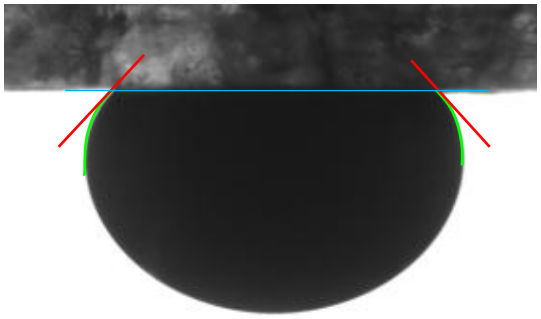

Figure 10. Contact angle calculation by Conic fitting method

The method is mathematically accurate, but is sensitive to distortions in the phase contact area caused by contaminants or surface irregularities at the sample surface. As only the contact area is evaluated, this method is also suitable for advancing and receding contact angle measurement. Nevertheless, this method requires good image quality close to the three-phase contact line.

Young-Laplace method theoretically calculates the contact angle. The complete drop contour is evaluated in this method. See section 2.1.2 for detail. The contact angle is determined as the slope of the contour line at the 3-phase contact point. The IFT between two liquid phases could be calculated together with contact angle if the real dimensions of the droplet are known. However, this method is suitable for large contact angles normally above 30°. Moreover, this model assumes a symmetric drop shape. Therefore, it is not suitable for advancing and receding contact angle measurement.

All methods discussed above calculate the contact angle as tangent at the intersection of the drop contour line with the solid surface base line. Depending on the value of contact angle measurement, the most suitable analysing method should be used.

In this study, more than one suitable method was used to calculate the contact angle of each image. The final contact angle is the one which gives the best fitting.

2.4 Literature review of contact angle measurement on reservoir fluids and rocks

2.4.1 Contact angle measurement on brine and crude oil on mineral rocks

Quite a few authors have investigated the contact angle of brine and crude oil on a solid surface, such and quartz [125-128] and reservoir rocks [129-132].

In Particular, Shedid *et al*. have reviewed the factors which affecting the contact angle measurement on crude oil, brine and reservoir rocks system [130, 131]. They confirmed that pre-saturation conditions have an important effect on the wettability of the rock samples. However the more interesting finding from them is that only at critical brine salinity, sessile drop volume has no effect on contact angle results. This thesis considered that sessile drop shape method itself is affected by the volume of the drop, but it will be influenced by different analysis approach, as discussed in section 2.3.2, since some of these approaches don't take the weigth of the droplet in to account. It could also be a result of the in homogeneity of the pre-saturated porous rock surface.

Xie *et al*. has measured the contact angle on brine, crude oil and quartz system by the Wilhelmy plate technique [126-128]. They have focused on the effect of crude oil composition on contact angle.

Mennella *et al*. also use Wilhelmy plate for contact angle determination on brine, crude oil and solid system. However, they applied dynamic Wilhelmy plate to measure the advancing and receding contact angle.

Rao *et al*. used a modified sessile drop approach, which called 'dual-drop-dual crystal' technique to measure the advancing and receding contact angle of brine, crude oil and quartz/reservoir rock systems [125, 129, 133].

2.4.2 Contact angle measurement on calcite

Form the literature, it was found that contact angle measurement on calcite surface have been done in some studies. But some of the investigations were on non-hydrocarbon system [134, 135], and some of them was focusing on the surface energy of calcite[136]. Just a few authors investigated the system of calcite with hydrocarbons and water/brine [137, 138].

Hansen *et al*. studied calcite wettability with stearic acid/water/n-decane system [138]. They have done contact angle measurement under high pressure conditions. However, only small effect of pressure on contact angle was found. Nevertheless, dissolution of calcite in water was suggested in their paper.

Gomari *et al*. use contact angle measurement to study the effect of acidic species effect on the wettability of calcite surface. The ions in brine and acidic species were discussed by contact angel and IFT measurement.

2.4.2 Contact angle measurement on CO_2 and brine/water

The measurement of contact angle involving CO_2 appears lesser in the literature. Recently, Jung *et al*. investigated the wettabilty of silica surface with the presence of CO_2 and brine. Their results indicated that CO_2 results in an increase of contact angle between water and silica; the contact angel increases with ionic strength.

The study by Bikkina *et al*. was done on CO_2, water and quartz/calcite system. And they found large effect from temperature on contact angle in such systems.

To summarize the literature, measurement of contact angle of crude oil and brine on a calcite surface has been carried out only for investigating the effect of acid components. Thus accurate contact angle measurements on brine, crude oil and calcite system would be useful to understand the wetting behaviour of such systems.

2.5 Experimental prediction of the wettability of reservoir rocks

Wettability relates to the relative attraction of reservoir rock to reservoir fluids. In oil reservoirs with connate or flooding water, the wettability ranges from pure water-wet to oil-wet. It's also is likely to vary over the reservoir, and the stage during the production. Except contact angle measurement, other techniques for wettability measurement are Amott and Amott-Harvey technique [139, 140], USBM wettability index [141], microscopic examination, microscopic examination, nuclear magnetic resonance approach, flotation method, glass slide method, determination from relative permeability, empirical reservoir logs, and dye adsorption.

In practice, most of the wettabilities are identified by wettability index measurement on core samples in the laboratory. The most common approaches are USBM wettability and Amott wettability, and more recently, nuclear magnetic resonance wettability.

2.5.1 USBM wettability index

This method is an industry standard for comparing the wettability of various core plugs and is an empirical measurement of wettability in porous media. It involves four procedures: (1), spontaneous imbibition of water/brine; (2), forced imbibition of water/brine; (3), spontaneous imbibition of crude oil/hydrocarbon; (4), forced imbibitions of crude oil/hydrocarbon. A centrifuge is usually used for forced imbibitions process. The detail of this method is discussed in a paper published by Donaldson *et al*. in 1969 [141].

2.5.2 Nuclear magnetic resonance wettability index

Determining the wettability of rocks from nuclear-magnetic-resonance (NMR) measurement is newer than the other techniques. It is based on the fact that additional nuclear relaxation time is required for fluids when they are in direct contact with the rock surface. Reduction of oil relaxation time away from its bulk value is generally known as a qualitative wettability indicator, assuming external factors to be negligible and/or invariant from one experiment to another. Through detailed modeling of the NMR response, this concept has been developed further to provide a quantitative wettability index. The detail of this technique was discussed in a paper published by Looyestijn *et al*. in 2006 [142].

2.6 Molecular dynamics simulation of IFT

Molecular simulation is a statistical mechanical method to obtain a set of configurations distributed according to a statistical distribution function, or statistical ensemble. Molecular Dynamics (MD) and Monte Carlo (MC) are the two primary types of molecular simulations. In MD, the equations of motions are integrated to track individual atoms. In the simulation, the system is given an initial set of positions and velocities, and the subsequent time evolution is completely determined by Newtonian mechanics. MC is a statistical method to sample phase-space faster by moving the molecules randomly and system properties can be statistically obtained. Several text books have described the methods in detail including Allen and Tildesley [143], Frenkeland [144], Rapaport [145].

The molecular dynamics simulation approach is used in this research. According to statistical mechanics, the interfacial tension, mechanically defined as the contractive force perpendicular to an infinitesimal interface, is related with the intermolecular forces on a molecular level. In a book

written by Rowlinson and Widom, the calculation of interfacial tension from intermolecular forces was deduced [51].

Regarding the surface tension of water, Fowler in 1937 [146] developed a relation between surface tension and the intermolecular forces. He introduced the approximation of a mathematical surface of density discontinuity between the two phases. The density of the vapor is infinite halves is calculated by an isothermal procedure. Finally he obtained the following expression for the surface tension,

$$\gamma = \frac{\pi}{8}\rho_l \int_0^\infty \gamma^4 \frac{d\phi(r)}{dr} g(r) dr \tag{2.19}$$

where ρ_l is the liquid density, $g(r)$ is the radial distribution function and Φ is the interatomic potential. This formula is pretty precise at lower temperature but can produce a large error at higher temperatures near the critical temperature.

In 1992, Harris [147] derived the formula for molecular models, although a similar result had already been derived by a simple analogy between atomic to molecular models. By using his formula with long range correction, Harris calculated the surface tension of alkane oligomers and found that the prediction is 30% higher than experimental values.

Kirkwood *et al*. [148] in 1994 proposed a new method to calculate the surface tension of an atomic liquid, where normal pressure tensor is:

$$P_N = kT\rho_\alpha^{(1)} - \frac{1}{6}\iiint r_{12} \frac{d\phi}{dr} \rho_\alpha^2(r_{12}) dV_{12} \tag{2.20}$$

and tangential pressure is,

$$P_T(x) = kT\rho^{(1)}(x) - \frac{1}{2}\iiint \frac{x_{12}^2}{r_{12}} \frac{d\phi}{dr_{12}} \rho^2(x, r_{12}) dV_{12} \tag{2.21}$$

Here α and β are fluid phases, $\rho^{(1)}(r)$ specifies the average number of molecules in volume dV at point r and Φ is the potential of atoms. However, this formula is only for monoatomic fluids.

In 1995, while using SPC/E model to simulate water, Alejandre *et al*. [149] found that the long range interaction is very important for surface tension. Their calculation domain is a rectangular parallel piped cell with a liquid phase in the middle and vapor on each side of the cell. To obtain the surface tension, they first calculated the pressure tensor by,

$$VP_{\alpha\beta} = \sum_{i=1}^{N} m_i \left(\vec{V}_i\right)_\alpha \left(\vec{V}_i\right)_\beta + \sum_{i=1}^{N-1} \sum_{j>1}^{N} \sum_{a=1}^{3} \sum_{b=1}^{3} \left(\vec{r}_{ij}\right)_\alpha \left(\vec{f}_{iajb}\right)_\beta \qquad (2.22)$$

where N is the number of molecules, V is the volume of system, m_i is the molecular mass, $\vec{\upsilon}_i$ is the velocity of center of mass, $\vec{r}_{ij}$ is the vector between the centre of mass of molecules i and j and

$$\vec{f}_{iajb} = -\frac{\vec{r}_{iajb}}{r_{iajb}} \left[\frac{dU\left(r_{iajb}\right)}{dr_{iajb}} \right] \qquad (2.23)$$

is the force between atom a in molecule i and atom b in molecule j. They calculated the surface tension by

$$\gamma = \frac{1}{2} L_z \left[P_{ZZ} - \frac{1}{2}\left(P_{XX} + P_{YY}\right) \right] \qquad (2.24)$$

They got fairly good results for both density and surface tension of water at various temperatures. The error of surface tension is less than 5 $mN \cdot m^{-1}$. This is also the approach used by Kuznetsova *et al*. [150] for the interfacial tension study between CO_2 and water. Their simulated IFT values have got fairly good agreement with the experimental data.

Chapter 3. Experimental measurement of IFT between CO_2 and brines under reservoir conditions

For carbon storage and CO_2 enhanced oil recovery reliable estimates are required of the IFT between CO_2 and different reservoir brines under the range of reservoir temperature and pressure conditions [55, 56].

This chapter reports the interfacial tension between carbon dioxide and aqueous solutions with total salt molalities between (0.98 and 4.95) $mol \cdot kg^{-1}$. The solutions studied are dissolved with single salts, simple salts mixtures or synthetic brine. The measurements were made at temperatures between (298 and 473) K at various pressures up to 50 MPa by means of imaging a pendant drop of CO_2-saturated brine surrounded by a water-saturated CO_2 phase. The expanded uncertainties at 95% confidence are 0.05 K in temperature, 70 kPa in pressure and, for interfacial tension, the larger of $0.016 \cdot \gamma$ and 0.6 $mN \cdot m^{-1}$.

The results of the study indicate that for the same type of ions, the interfacial tension increases linearly with the molality of the salt solution. For strong electrolyte brines, IFTs linearly depend on the positive charge concentration.

Two empirical models have been developed to represent the present results as a function of temperature, pressure and molality. The first models with an absolute average relative deviation of 2% are essentially applicable to conditions above the supercritical temperature of CO_2, while the second model is also applicable to the subcritical temperature of CO_2 but has a larger absolute average relative deviation of 6%.

A new apparatus for carrying out the IFT measurements on corrosive fluids at high temperatures (up to 473 K) and high pressures (up to 50

MPa) was described. The brine systems studied in this work are listed in Table 1. Ambient condition IFT was explored and it has good agreement with the literature [55, 56].

Table 1. Total salt molalities *m*, temperatures *T* and pressures *p* studied in this work

Brine		*m* (mol·kg^{-1})	*T* K	*p* MPa
1	NaCl + KCl (5:1 Wt%)	0.98	298, 323, 343, 373, 393, 423, 448	2, 4, 6, 8, 10, 12, 14, 16, 18, 20, 25, 30, 35, 40, 45, 50
2		1.98	323, 343, 373, 393, 423	
3		3.15	298, 323, 343, 373, 393, 423	
4		4.95	323, 343, 373, 423	
5	$CaCl_2$	2.50	343, 373, 393, 423	
6		5.00	343, 373, 393, 423	
7	$MgCl_2$	2.50	343, 373, 393, 423	
8		5.00	343, 373	
9	Na_2SO_4	0.49	373	
10		0.98	343	
11	$NaHCO_3$	0.98	343, 373, 393, 423	
12	NaCl	1.0	473	2, 10, 20,30, 35, 40,
13	Qatar brine low		343, 393	
14	Qatar brine high		343, 393	

3.1 Materials

Pure deionised and degassed water (electrical resistivity > 18 MΩ·cm) was used. Carbon dioxide was supplied by BOC with a specific minimum mole fraction purity of 0.99995 in a cylinder fitted with a dip tube to permit withdrawal of liquid. All salts were purchased from Sigma-Aldrich, with mass fraction purities of ≥ 0.995 and ≥ 0.99 % respectively. The un-hydrate salts were dried in an oven at T = 373.15 K. Solutions were prepared gravimetrically with the relative uncertainties in mass being below 0.01 %. Thus, the relative uncertainty of molality was most probably limited only by the purity of the salts and was taken to be approximately 0.5%. The brines were degassed by sonicating in an ultrasonic bath for 15 min immediately prior to use.

3.2 Experimental setup for IFT measurement

As implemented, the apparatus allowed the IFT to be measured at temperatures up to 473 K with pressures up to 50 MPa. Leaks are major concerns in this type of system. The system was therefore thoroughly leak tested over the whole pressure range with both helium and water and exhibited a high-level of integrity.

The new apparatus, shown schematically in Figure 11, was designed and built in this work for the purposes of both IFT and contact angle measurements involving brines, CO_2 and hydrocarbons. All wetted metallic parts are made from either Hastelloy C276 or titanium, both of which are fairly resistant to corrosion in concentrated brines. The core of the apparatus is an autoclave view cell, indicated as C1 in the figure. This cell comprised a hollow cylindrical body, fabricated from Hastelloy C276, closed at either end by Hastelloy and sapphire window assemblies sealed with PTFE o-rings. The vessel was orientated with its axis horizontal and the internal dimensions were: diameter 28mm, length 40 mm. Four threaded fluid ports were machined in the body suitable for connection of 6.35 mm o.d. coned-and-threaded high-pressure tubing. In the present work, reducing unions were fitted to two of these ports to permit connection of 1.6 mm o.d. tubing for fluid injection (N1 and N2); the third was connected to a tee union and thence to both a rupture-disc safety device and the drain valve; and the fourth port was plugged. The two reducing unions were drilled through so that the inlet capillaries (N1 and N2 in Figure 11) could pass to the interior of the cell such that drops or bubbles formed at the ends could be imaged. Pendant drops were formed from the end of capillary N1, which entered through the top of the cell, while sessile drops or bubbles could be created from the tip of capillary N2.

For contact angle measurement, special mineral support which could fit in the view cell were designed, see Appendix G for detail.

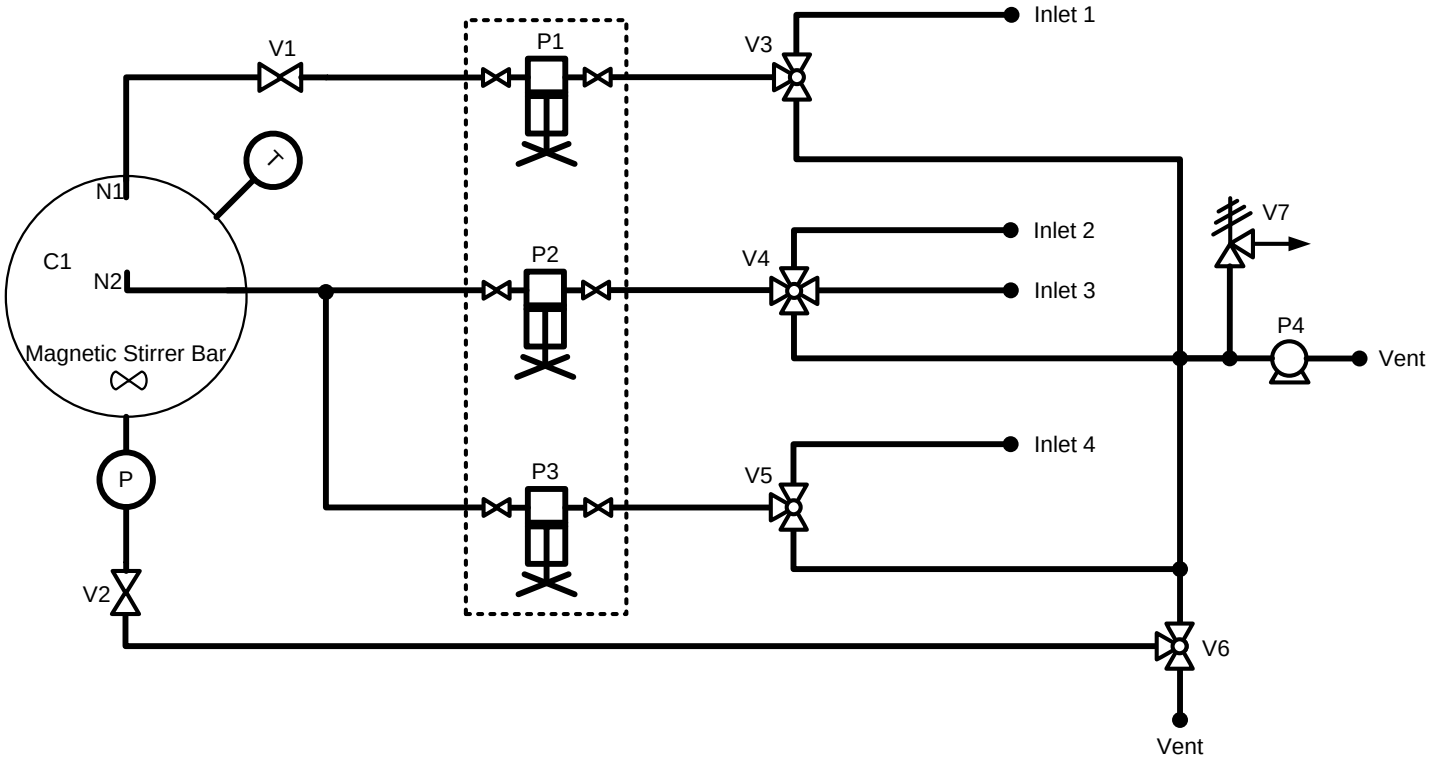

Figure 11. Schematic diagram of the apparatus.
C1: windowed autoclave cell with stirrer; P1, P2, P3: high-pressure Quizix pump; T: temperature sensor (Pt100); P: flow-through pressure sensor (DF2): V1, V2: high-pressure valve (type 2); V3, V5, V6: three-way valve; V4: four-way switch; V7: relief valve; P4: vacuum pump; N1, N2: injection port

A blind axial hole drilled in the vessel wall (5 mm diameter × 50 mm long) accommodated a Pt100 sensor that was used to measure the experimental temperature. In order to achieve a uniform temperature, the cell was enclosed in a five-piece close-fitting aluminium-alloy heater shell insulated on the outside by a jacket of silicone-rubber foam. See Figure 12, four cartridge heaters and an additional Pt100 temperature sensor were accommodated in axial holes bored in the heater shell, and used in conjunction with a PID process controller to regulate the temperature.

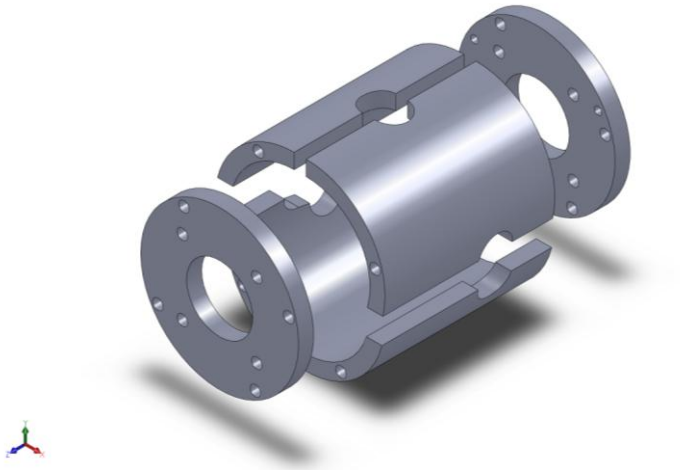

Figure 12. Solidworks drawing of the heating shell

A supporting bracket was used to mount the cell horizontally on a 1 m long optical rail. Also mounted on the rail were an adjustable LED light source, a diffuser, and a monochrome CCD camera (IEEE1394 Digital FireWire camera, Foculus) fitted with a fixed focal length lens.

For this experiment, white light is always preferred as a lighting source. Because it composed of a wide range of wavelengths, chromatic aberration can occur which causes blurring of the image of the drop at the edge [151]. Although this chromatic effect can be reduced if a narrow range of wavelengths is selected by filters [152, 153], white lighting source and a light diffuser were used in this experiment. Figure 13 shows

the light engine and a house designed holder for it. The intensity of the light is adjustable by a programme loaded on the computer.

Figure 13. LED array and engine (holder on the left)

Geometrical distortion and spherical aberration are the most significant problems of a lens in an optical system regardless of the type of illumination used [154]. For this reason, the lens used in this research is a fixed focal length lens. It's a simple way to alleviate the effect of the spherical aberration.

The specification of the digital CCD camera (IEEE1394) is detailed in Table 2. It has a sensor diagonal size of 1/3" and a frame rate of 60 frames per second. This relatively high frame rate is required for dynamic interfacial tension measurement. It's also an important performance for studying the the rheology of crude oils, which might be done on this equipment in the future.

Table 2. Specification of IEEE 1394 Digital CCD Camera

Sensor	1/3"
Resolution	330,000 pixel, VGA
Trigger	External
Frame Rate	60 fps
Camera casing	44 mm x 29 mm x 63 mm
Aspect ratio	4 : 3

Except the discussion above, it was noticed that the actual focal lengths changed a bit when the density of the medium changes. However this change can't be neglected when high accuracy measurement is

expected. Thus a positioned, as shown in Figure 14, is mounted with the camera on the optical rail. This small instrument made it easy to adjust the positions of the camera to obtain the best quality of the image during the experiment.

Figure 14. Positioner for the camera

In this research, commercial software (Advanced DROPimage, Ramé-Hart Instrument co.) was used to perform the experimental procedure. The numerical methods used have been described in two papers by Hansen [81, 82] and make use of the ratio $\sigma = D_S/D_E$ first introduced by Fordham [155] in 1938 for the purposes of obtaining initial estimates of β and R_0 from an experimental drop profile. The final values of these parameter are obtained by a fast optimisation method involving a 3×3 matrix of drop profiles generated from Eq. (2.5) for values of β and R_0 around the initial estimates. The Kutta-Merson [84] numerical integration algorithm is used with automatic step length adjustment. The detail of this method is introduced in Chapter 2. Table 3 is a list of the parameters of a drop involved in the analysis of a drop profile.

Table 3. Type of results from the analysis of the drop or bubble by the software

Surface/ Interfacial tension
Contact angle
Surface energy of Solids
Drop dimensions, such as Height Width Radius of curvature Volume
Surface area
Surface elasticity and viscosity

Mixing of the cell contents was accomplished by means of an internal PTFE-coated magnetic stirrer bar (10 mm long x 3 mm diameter), driven by an external SmCo magnet assembly mounted on a shaft that passed through a small hole on the optical rail to a variable-speed electric motor beneath. See Figure 15.

Figure 15. From left to right; magnetic pair, gear box and motor

A flow-through pressure transducer (DJ Instruments, Model DF2) was connected in the outlet line before valve V2 (see Figure 11). A system of three high-pressure syringe pumps (Quizix Q5000 series, Chandler Engineering) with wetted parts of Hastelloy C276 was used for injection of CO_2, brine and wash water. Each syringe had a capacity of 10 mL and was fitted with its own safety head, pressure transducer and air-actuated fill and dispense valves (not shown in Figure 11). In order to minimize dead volumes, 1.6 mm o.d. $\times$ 0.5 mm i.d. tubing (Hastelloy HC276) was used on all the fluid connections between the pumps and the view cell.

Referring to Figure 11, pump P1 was used for the brine, which was drawn in from the supply bottle through a filter with 10 μm pore size. Pump P2 was used for flushing with pure water and, occasionally, other solvents and was provided with two alternative inlet lines also fitted with 10 μm pore-size filters. Finally, pump P3 was used for CO_2 injection. To permit charging of P3 with liquefied CO_2, the syringe was operated at a temperature of 283 K by passing water from a chiller unit through a jacket. A 0.5 μm pore size particulate filter was fitted in the CO_2 filling line. Valve V1 permitted isolation of the inlet capillary from P1, while valve V2 was used to control the fluid outlet; valve V6 was provided to permit connection of the outlet line to either a waste receiver or to a vacuum pump, the latter being protected from accidental over-pressure by relief valve V7. Details of these high pressure components were listed in Appendix D. The complete set-up is shown in Figure 16.

Figure 16. Experiment set-up of interfacial tension and contact angle measurement. Insert: fluid injection pumps

3.3 Experimental procedure

Using the new apparatus introduced above, the IFT could be measured by imaging either a sessile CO_2 bubble injected through needle N2, in a CO_2-saturated bulk brine phase, or a pendant brine drop injected through needle N1 into a water-saturated CO_2 bulk phase. In theory, both approaches will present the same IFT value after the system reaches equilibrium. In view of the fact that pendant drops tend to be more stable than sessile bubbles, we opted for the second approach in this work. In

practice, it was our experience that the brine drop, having a volume of less than 30 µL, injected into the 25 mL bulk phase required not more than about 10 minutes to be saturated with CO_2. In order to be sure that the CO_2 bulk phase was water saturated, we first injected a few mL of brine into the bottom of the cell and stirred the system for at least 5 minutes.

Prior to first use, the entire system was cleaned very carefully with hexane, acetone, water and CO_2 in sequence, repeated many times. Since a stable pressure is faster to achieve than a stable temperature, each group of IFT measurements was carried out at fixed temperature with rising pressures. Before measuring a new isotherm, the previously-evacuated cell was first flushed several times with CO_2, and subsequently filled with CO_2 to a pressure of around 3 MPa, before closing the outlet valve of the CO_2 syringe pump and setting the desired operating temperature. After temperature stabilization, degassed brine was first compressed in pump P1 to a pressure slightly higher than that of the fluid in the cell, and then valve V1 was opened and a quantity of brine was pumped into the cell. The pressure of the cell was subsequently adjusted by discharging or injecting CO_2. Before measuring a new drop, at least three drops, together accounting for the dead volume downstream of valve V2, were discarded to ensure that every measured drop was independent and identically fresh when the measurement started. Once the measuring drop was formed at the end of needle N1, valve V1 was closed immediately and drop imaging was started.

To ensure that the CO_2 was saturated with water, sufficient brine to fill the lower 1/8th of the cell was injected. The mixing device was turned on after every pressure change, as this greatly reduced the time required for rebalancing the system, but it was then turned off for the measurement.

The changes in the refractive index of the CO_2-rich bulk phase, arising from changes in pressure or temperature, had a marked influence on the focusing of the camera which was readjusted whenever the thermodynamic condition changed. The intensity of the light and the aperture of the lens were also adjusted to achieve satisfactory contrast and depth of field.

For every state point, at least three drops were measured, and each was monitored for at least 600 s with an interval of 6s. As discussed in the literature [97], the value of γ is expected to vary with time following the creation of a fresh drop.

An initial variation with time should occur as CO_2 dissolves in the brine and eventually saturates the entire volume of the drop. The time scale for this is expected to be of the order of 1 min. Following this initial equilibration, the measured γ is expected to be essentially constant for an extended period but, on a much longer time scale, drift is expected as trace impurities diffuse towards the interface.

3.4 Validation and calibration

3.4.1 Data validation

The pendant drop method is well established and so just a few initial experiments were performed for validation purposes. The IFT of (Air + H_2O) was measured at T = 298.15 K and ambient pressure. The interfacial tension was found to be (71.9 ± 0.1) $mN \cdot m^{-1}$, in close agreement with the published value of Pallas *et al*. [156], (71.99 ± 0.05) $mN \cdot m^{-1}$. Additional confidence comes from comparing our results, extrapolated to zero molality, with the data for (CO_2 + H_2O) reported by Georgiadis *et al*. as discussed below [97].

3.4.2 Drop size effect on IFT

Theoretically, the measurement of IFT by means of ADSA-P method is expected to be independent from the volume of the drop. However, in the literature, the effect of drop size on interfacial tension by has been noticed [157, 158]. An example was the surface tension of cyclohexane (with purity greater than 99.9%), which changes (in this case increases) as the volume of the drop decreases.

In practice, for a drop with a well-deformed shape, ADSA-P method calculates the interfacial tension precisely. However, as the drop volume decreases, the drop shape becomes closer to spherical and the results start deviating from the correct value. This error is due to the limitation of the numerical schemes and the noise in the experimental profile. As discussed in chapter 2, for nearly spherical drop shapes, significantly different IFT values correspond to only slightly different drop shapes. Thus, even small errors in the experimental profile detected from the image of the drop can slightly shift the selected Laplace curve, which can cause the surface tension value to deviate dramatically from the true value. For this reason, a study on the drop size effect particularly on our apparatuses was carried out in this research.

As shown in Figure 17, the volume of a brine pendant drop in CO_2 bulk phase and the IFT between them were monitored simultaneously. In the first 2400 second, the volume of the drop oscillated between (0 and 35) µL. Correspondingly, the interfacial tension changed between (0 and 37) $mN \cdot m^{-1}$. But from 2400 to 7200 s, with the drop volume varying between (27 and 35) µL, the interfacial tension varied between (34.5 and 35.5) $mN \cdot m^{-1}$. However, this 1 $mN \cdot m^{-1}$ fluctuation of IFT was consider as a results of re-equilibrium when fresh brine were injected in to the system.

Similar phenomena can be seen from Figure 18, a brine drop varied between (2 and 40) µL in volume obtained large variation of measured

interfacial tension. However, when the volume of the drop changed between (25 and 37) μL, the equilibrated interfacial tension varied in a range the same as above. It was found that, in a range of the drop volume, with well-deformed shape, the IFT measured by ADSA-P method are equivalent.

The same conclusion was made after a comparison of IFTs measured from the drops with different size but under the same conditions. The IFT measurement by ASDA-P approach on well developed drops gives is accurate, and independent from a range of the drop volume.

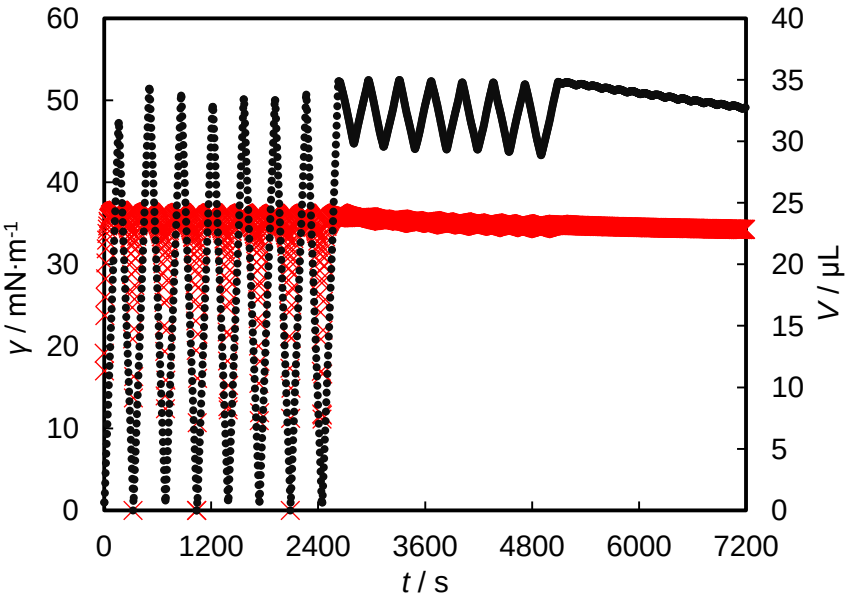

Figure 17. Interfacial tension of (CO_2 + H_2O + NaCl + KCl) system m = 1.98 mol·kg^{-1}, as a function of time at T = 298 K, p = 10MPa: ×, interfacial tension; ●, drop volume

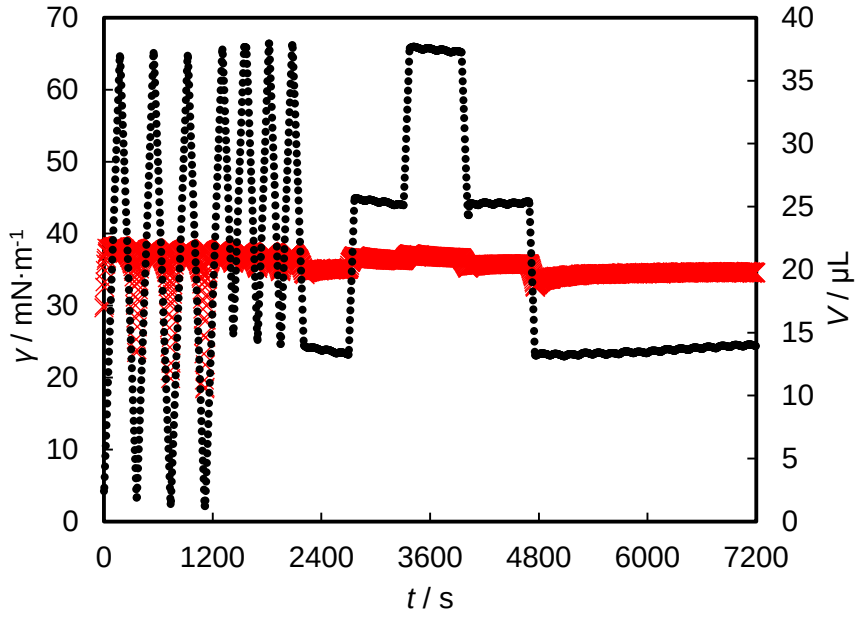

Figure 18. Interfacial tension of (CO_2 + H_2O + NaCl + KCl) system m = 1.98 mol·kg^{-1}, as a function of time at T = 298 K, p = 10MPa: ×, interfacial tension; ●, drop volume

3.4.3 Calibration

The Pt100 thermometer inserted in the body of the high pressure cell was calibrated at the temperature of the triple point of water, and at four further temperatures in the range (323 to 473) K by comparison in a constant-temperature bath with a standard platinum resistance thermometer having an expanded uncertainty of 2 mK. Taking sensor drift and fluctuations of the thermostat into account, we estimate that the overall expanded uncertainty of the cell temperature measurements was 0.05 K, with a coverage factor k = 2.

The model DF2 flow-through pressure transducer was calibrated against a hydraulic pressure balance (DH-Budenberg model 580EHX) having an expanded relative uncertainty of 0.008 % at six pressures up to 50 MPa. The mean and maximum absolute deviations arising from non-linearity and hysteresis were 18 kPa and 47 kPa respectively. However, this

sensor did drift over time and corrections were required. The ambient pressure reading was compared and corrected before every experiment. Any difference was applied as a constant offset to correct subsequent readings in that run. Taking all factors into account, the expanded uncertainty of the pressure in the cell was estimated to be 70 kPa (k = 2).

Since the dimension R_0 appears in Eq. (2.5), it was necessary to calibrate the imaging system against a standard. This was done at the beginning of the experiment and every time after adjusting the lens on the camera. For this purpose, a calibration tool having a ball and a pin both of (4.000±0.001) mm diameter (Precision Combo Calibration Device) was used. As shown in Figure 19. Typical drop sizes, quantified by $R_0 \approx 0.5D_E$, were approximately 2 mm, while an effective resolution of ±0.5 pixels corresponded to ±0.006 mm in the image. Thus the fractional resolution in the determination of R_0 is estimated to be approximately 0.3 %. Hansen [81, 82] reports that, through the benefits of averaging, the effective resolution in edge recognitions can be better than ±0.2 pixels.

Figure 19. Calibration tools for ramé-hart tensiometer

3.5 Densities difference

To calculate the IFT with the pendant drop method, the difference between the densities of the two fluids needs to be known. Since the two

phases have very limited mutual solubility, this difference in densities is expected to be close to the difference between the densities of the pure brine and CO_2 at the temperature and pressure in question. However, at low temperatures and high pressures, where $\Delta\rho$ is small, errors in the phase densities have a large influence on the derived values of interfacial tension. Thus, in the absence of directly measured densities, the estimation of $\Delta\rho$ must be carried out carefully. The densities of coexisting phases in the (water + CO_2) system have been measured by Hebach *et al*. [159] at pressures up to 30 MPa and at temperatures between (284 and 322) K. They found that the density of the CO_2-rich phase did not differ from that of pure CO_2 within the experimental uncertainty of 0.15 %. The density of the aqueous phase was found to exceed that of pure water by an amount that follows the solubility of CO_2 in water, increasing with increasing pressure and declining with increasing temperature. For example, interpolated to T = 298.15 K, the lowest temperature in the present study, the density exceeds that of pure water by 16 kg·m^{-3} at p = 30 MPa. When the mass fraction w of dissolved CO_2 is evaluated from the model of Duan *et al.* [160], the results of Hebach *et al*. [159] conform within experimental uncertainty to the simple model of Pruess and Spycher:[161]

$$1/\rho = (1-w)/\rho_{\mathrm{w}} + w/\rho^{*}_{\mathrm{CO_2}} \tag{3.17}$$

Here, ρ_{w} is the density of water (or brine) and $\rho^{*}_{\mathrm{CO_2}}$ is the inverse of the partial specific volume of CO_2 in solution, which is taken to be 1260 kg·m^{-3} independent of temperature and pressure. Since the model of Duan *et al.* [160] is also applicable to CO_2 solubility in brines, we have applied this with Eq.(3.17) and the same value of $\rho^{*}_{\mathrm{CO_2}}$ to obtain the density of the aqueous phase. The density of the pure brine was obtained from measurements made in our laboratory which have a relative standard uncertainty of 0.015 % [162]. In view of the findings of

Hebach *et al*., [159] we take the density of the CO_2-rich phase to be that of pure CO_2, which we obtained from the equation of state of Span and Wagner [163]. Clearly, our method of estimating $\Delta\rho$ is subject to uncertainty most probably dominated by the effect of CO_2 dissolution on the density of the aqueous phase. For purposes of estimating the uncertainty of γ, we take the uncertainty $\delta(\Delta\rho)$ in the density difference to be one tenth of the difference between the calculated density of the CO_2-saturated brine and the density of the CO_2-free brine: $\delta(\Delta\rho) = 0.1(\rho - \rho_w)$. We note that recalculation of γ is straightforward if more reliable experimental values of the density differences were to become available.

For this reason, we have designed a separate rig to measure at the same time the densities of two fluids with each other saturated in the under different temperature and pressures. Depending on the mixing fractions, both saturated and non-saturated densities of two miscible and immiscible fluids can be measured. As shown in Figure 20, a flow diagram of the apparatus, it is capable to measure fluid densities with a pressure ranges from ambient to 68 MPa and temperature ranges from ambient to 473 K. All wetted metallic parts are made from either Hastelloy C276 or titanium, both of which are fairly resistant to corrosion in concentrated brines. A high temperature and high pressure (HTHP) vessel which has a volume of 50 mL within an oven is connected via high pressure tubing to two fluid injection pumps (Quizix, CMD 5000-10K) and two high pressure densimeters (DMA-HPM). The pumps are used to introduce fluids, including CO_2, water/brines or hydrocarbons, into the vessel, and to compress them further.

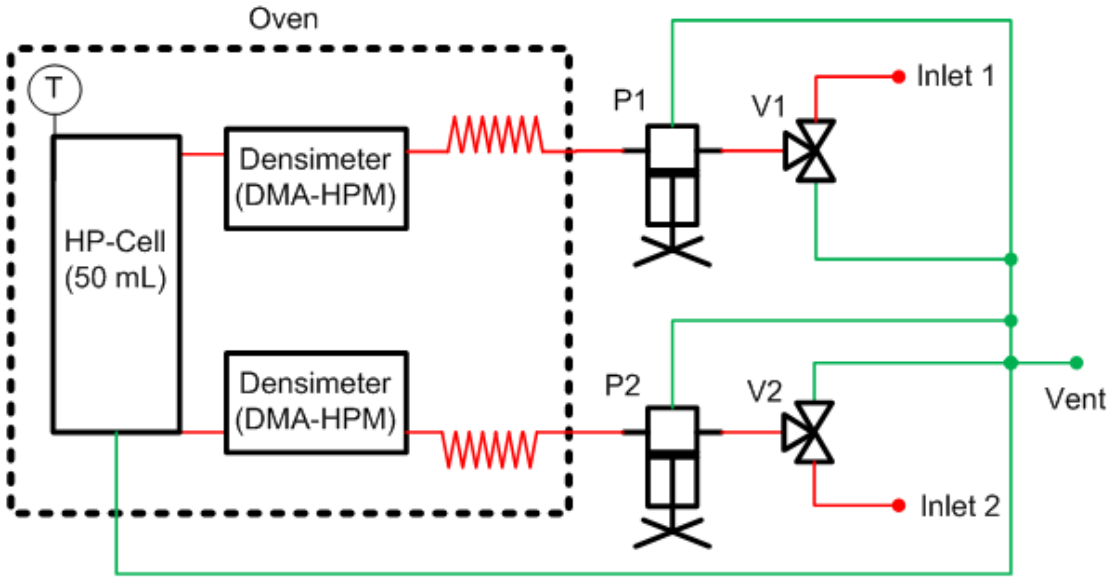

Figure 20. Schematic diagram of the apparatus for density measurement.
HP-Cell: autoclave cell with stirrer; P1, P2: high-pressure Quizix pump; T: temperature sensor (Pt100); V1, V2: high-pressure valve

An image of the apparatus is shown in Figure 21. The temperature of the vessel is regulated by an oven. The pressure is maintained by using the Quizix pumps, or by isolating the vessel with manual valves. The readings of the vessel temperature and pressure are recorded using a custom programmed VEE code.

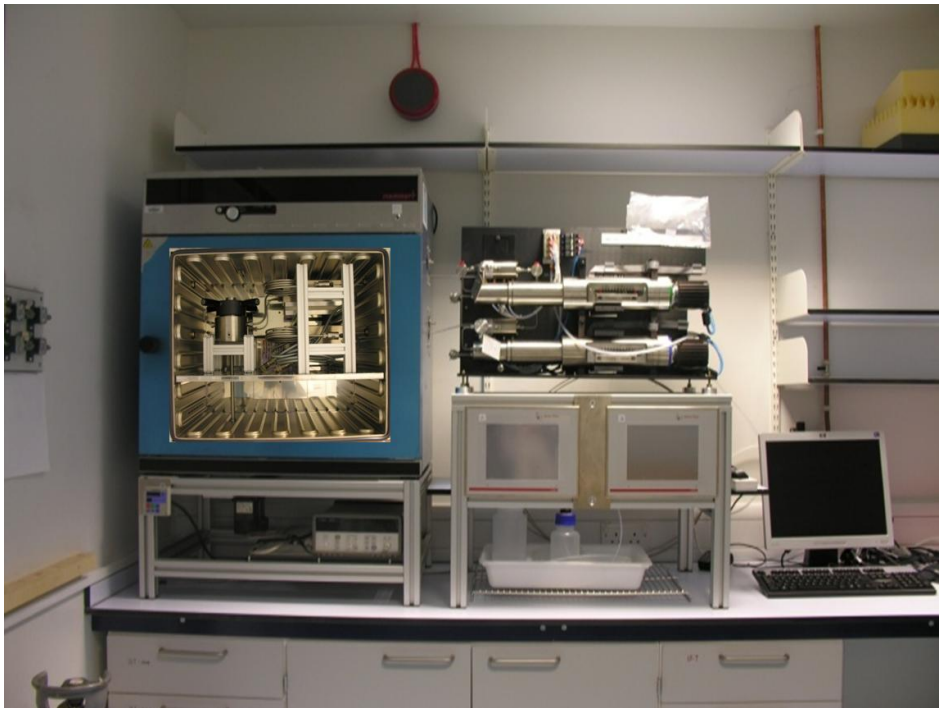

Figure 21. Experimental setup of density measurement

Before starting the measurement, brine and CO_2 are pre-mixed in the high pressure cell by a stirrer bar driven by a pair of magnet underneath the cell under the target thermodynamic conditions. Meanwhile, the two Quizix pumps, P1 and P2 are operated as a pair oscillating the fluids in the systems. After the two phases achieve equilibrium, the pumps are operated in tandem to allow: first, fluid from the top phase to be raised into the upper DMA; and, second, fluid from the lower phase to be lowered in to the lower DMA. In addition, external to the oven are the DMA readouts, pressure and temperature readouts and a controller PC.

The Density of CO_2 saturated water was compared with the reference data. See Figure 22, it indicated a big difference between the density of pure water and CO_2 saturated water.

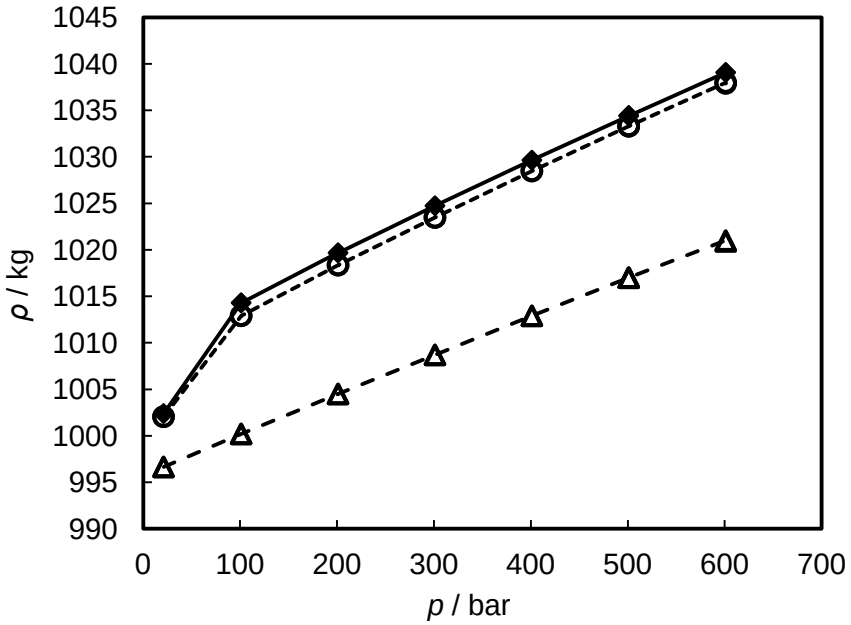

Figure 22. Density of CO_2 saturated H_2O as a function of pressure compared to literature values at T = 303 K
symbols: ■, this work; O, reference modle,; △, pure water density

3.6 IFT results and discussion

The IFT was measured for CO_2 and (0.864 NaCl + 0.136 KCl)(aq) for total salt molalities m, temperatures T and pressures p as detailed in Table 1. The mole fractions of NaCl and KCl of the salt correspond to a mass ratio of 5:1 and total salinities up to 4.95 mol·kg^{-1} were studied. At least four isotherms were measured at each concentration. For each isotherm, 16 pressure points were measured from 2 to 50 MPa. $CaCl_2$(aq) and $MgCl_2$(aq) were studied at molalities of (2.5 and 5.0) mol·kg^{-1}; for Na_2SO_4(aq) the molalities were (0.49 and 0.98) mol·kg^{-1} (restricted by the saturation limit at ambient temperature). Each system was studied at various temperatures between (343 and 423) K and various pressures

between (2 and 50) MPa. NaHCO3 were studied at molalities of 0.98 mol·kg^{-1} between (343 and 423) K and various pressures between (2 and 50) MPa. NaCl were studied at molality of 1.0 mol·kg^{-1} at 473K. Low salinity Qatari brine and high salinity Qatari brine are measured under the same pressure conditions (2 to 50) MPa at 343 K and 393 K. The experimental data, 730 in number, are given in Appendix F.

The relative standard deviation σ(*γ*)/*γ* of the IFT data gathered at each state point was computed from a number of repeated measurements; on average it was 0.7 % and in all cases it was < 2 %. The overall relative standard uncertainty u_r of γ was calculated from the relation

$$u_r^2 = \left[\frac{1}{\gamma}\left(\frac{\partial\gamma}{\partial T}\right)_{p,m}\delta T\right]^2 + \left[\frac{1}{\gamma}\left(\frac{\partial\gamma}{\partial p}\right)_{T,m}\delta p\right]^2 + \left[\frac{1}{\gamma}\left[\frac{\partial\gamma}{\partial m}\right]_{p,T}\delta m\right]^2 + \left[\frac{\delta\Delta\rho}{\Delta\rho}\right]^2 + \left[\frac{\sigma(\gamma)}{\gamma}\right]^2 \quad (3.18)$$

Combining the standard uncertainties δ*T*, δ*p*, δ*m* and δΔ*ρ* in the temperature, pressure, molality and density difference respectively with the largest values of the corresponding partial derivatives found in the ranges investigated, the average u_r for all state points was found to be 0.8 %. Thus the expanded relative uncertainty of *γ* at 95% confidence was 1.6%.

Figure 23 shows a comparison at *T* = 373 K between the interfacial tension of the (CO_2 + H_2O + NaCl + KCl) system studied in this work at *m* = 1.98 mol·kg^{-1} and values of the system (CO_2 + H_2O + NaCl) from two different authors: Bachu [98] *et al*., at *m* = 2.15 mol·kg^{-1}; and Chalbaud [105] *et al*., at *m* = 1.79 mol·kg^{-1}. Assuming that the influence of Na^+ and K^+ ions on the interfacial tension are very similar, the results are comparable and one would expect those of Chalbaud to fall slightly lower (smaller *m*), and those of Bach (larger *m*) above, our data.

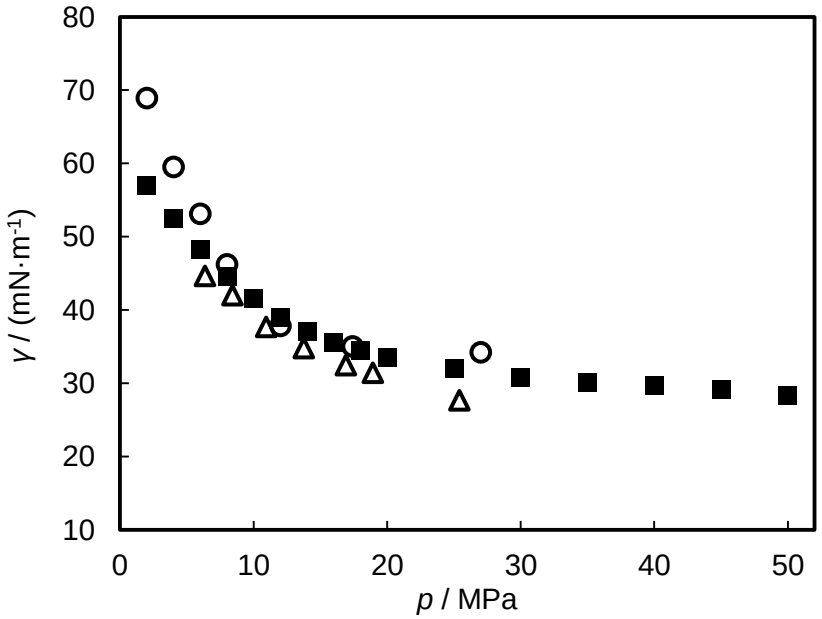

Figure 23. Interfacial tension of the (CO_2 + H_2O + NaCl + KCl) system as a function of pressure compared to literature values at T = 373 K symbols: ■, this work, m = 1.98 mol·kg^{-1}; ○, Bach *et al*., m = 2.15 mol·kg^{-1}; △, Chalbaud *et al*., m = 1.79 mol·kg^{-1}

In Figure 24 we compare our results for the IFT of CO_2 + $CaCl_2$(aq) at T = 373 K and m = 2.5 mol·kg^{-1} with results for the same system from Aggelopoulos *et al*. [103] at m = (1.8 and 2.7) mol·kg^{-1}. Taking into account the differences in salinity, the agreement with the present results is good.

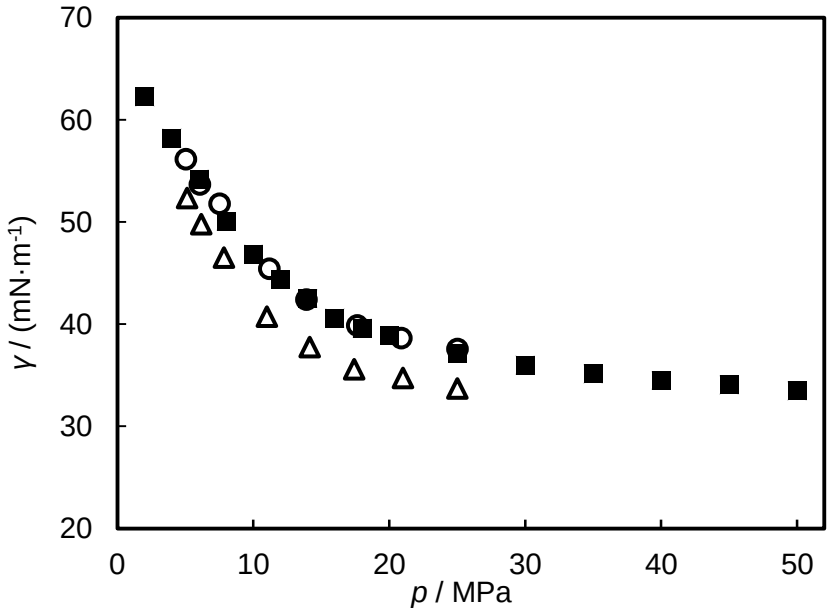

Figure 24. Interfacial tension of the CO_2 + $CaCl_2$(aq) at T = 373 K as a function of pressure
symbols: ■, this work at m = 2.5 mol·kg^{-1}; O, Aggelopoulos *et al*. at m = 2.7 mol·kg^{-1}; △, Aggelopoulos *et al*. at m = 1.8 mol·kg^{-1}

3.6.1 CO_2 and brine IFT dependence on time

For every state point, at least three drops were measured, and each was monitored for at least 600 s with an interval of 6s. As discussed by Georgiadis *et al*. [97], the value of *γ* is expected to vary with time following the creation of a fresh drop. An initial variation with time should occur as CO_2 dissolves in the brine and eventually saturates the entire volume of the drop. The time scale for this is expected to be of the order of 1 min. Following this initial equilibration, the measured *γ* is expected to be essentially constant for an extended period but, on a much longer time scale, drift is expected as trace impurities diffuse towards the interface.

This behaviour was indeed observed but the time dependence of *γ* differed with changes in temperature and pressure. At lower temperatures and high pressures, γ was observed to decrease rapidly in

an initial transition period after the creation of each drop, as reported by many authors [63, 94, 97, 105, 164]. However, the same phenomenon was not obvious at high temperatures or at low pressures, presumably because diffusion coefficients increase rapidly with temperature while CO_2 solubility declines with increasing temperature or reducing pressure. The time evolution of the measured IFT between CO_2 and (0.864 NaCl + 0.136 KCl)(aq) with molality m = 1.97 mol·kg^{-1} is shown in Figure 25 for different pressures at T = 323.15 K.

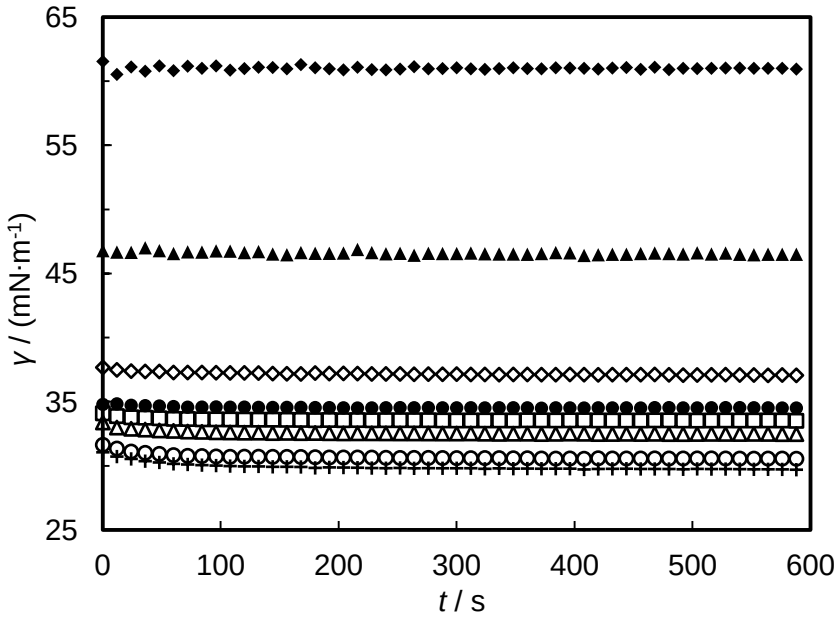

Figure 25. Interfacial tension as a function of time at different pressures (CO_2 + H_2O + NaCl + KCl) system, m = 1.98 mol·kg^{-1}, at T = 323.15 K, symbols: ◆, p = 2 MPa; ▲, p = 6 MPa; ◇, p = 10 MPa; ●, p = 16 MPa; □, p = 20 MPa; △, p = 30 MPa; ○, p = 40 MPa; +, p = 50 MPa

The figure indicates that, at the same temperature, the time dependence is different at different pressures and that a steady value was achieved after about 150 s. This time became shorter with increasing temperature. The reported values of γ were therefore based on a mean computed over the period between (150 and 600) s after the creation of a fresh drop; the standard deviation was also computed.

3.6.2 CO_2 and brine IFT dependence on pressure

At all brine concentrations, *γ* is observed to decrease with increasing pressure when the salinity and the temperature are kept constant. The results for m = 1.98 mol·kg^{-1} NaCl and KCl mixtures are taken as an example and plotted in Figure 26. At the same temperature, the profile of the drop changes dramatically with increasing pressure. To achieve a well developed droplet, the volume of the drops has large difference under different pressures. From Figure 27 on each isotherm, it can be seen that *γ* decreases rapidly with increasing pressure when the pressure is lower than the critical pressure of CO_2; thereafter *γ* decreases more gradually with increasing pressure. The same behaviour can be seen for all of the brines tested. As pressure increases from 0 to 10 MPa the solubility of CO_2 rapidly increases [160] and thus, in the presented interfacial tension versus pressure plots (below) a corresponding rapid decrease in interfacial tension is observed over the 0 to 10 MPa pressure range. The results for $CaCl_2$(aq) for m = 2.5 mol·kg^{-1} are taken as an example and plotted in Figure 28. It is clear that *γ* decreases continuously with increasing pressure, rapidly at first and then more gradually at high pressures.

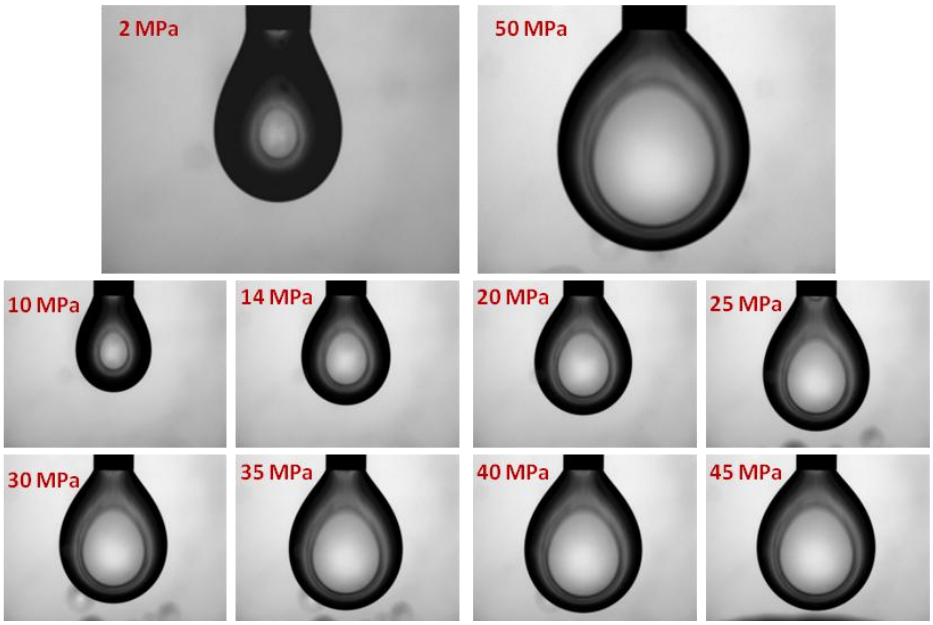

Figure 26. Drop profile as a function of pressures
(CO_2 + H_2O + NaCl + KCl) system, m = 1.98 mol·kg^{-1}, at T = 323.15 K

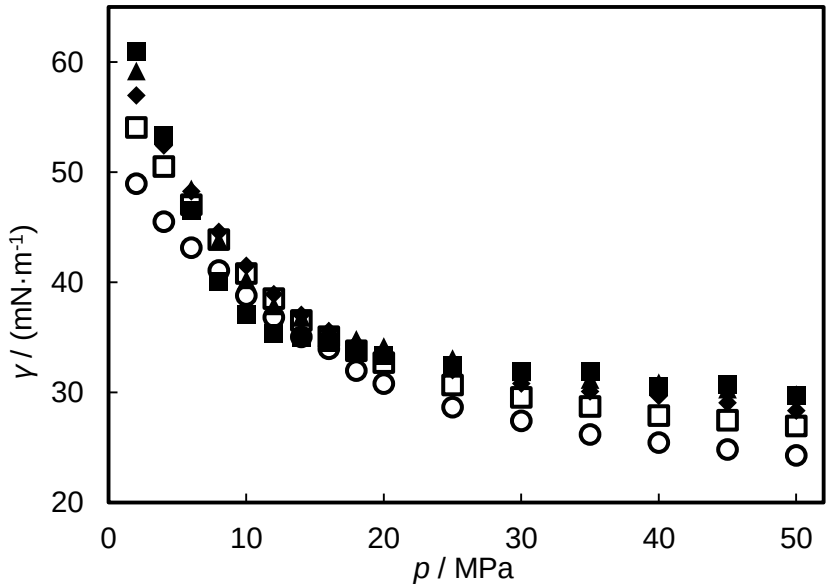

Figure 27. Interfacial tension as a function of pressure at different isotherms
(CO_2 + H_2O + NaCl + KCl) system, m = 1.98 mol·kg^{-1}, symbols: ■, T = 323.15 K; ▲, T = 343.15 K; □, T = 393.15 K; O, T = 423.15 K; ◆, T = 373.15 K

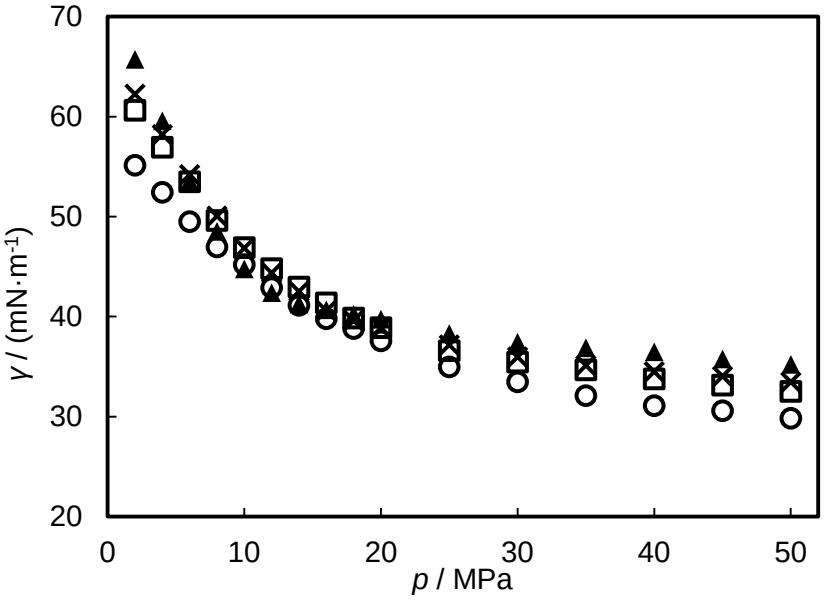

Figure 28. Interfacial tension as a function of pressure on different isotherms
CO_2 and $CaCl_2$(aq) at m = 2.5 mol·kg^{-1}, symbols: ▲, T = 343.15 K; ×, T = 373.15 K; □, T = 393.15 K; ○, T = 423.15 K

3.6.3 CO_2 and brine IFT dependence on temperature

Figure 29 and Figure 30 shows the IFTs plotted along isobars as a function of temperature and it can be seen that the trends, while smooth, are more complicated. This has also been noted in the literature [96, 99, 104, 165].

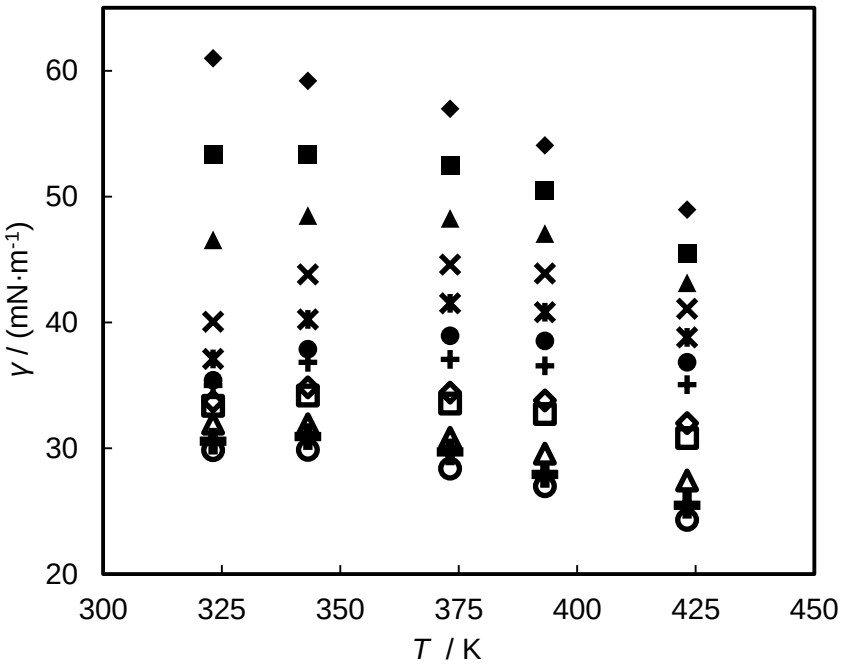

Figure 29. Interfacial tension as a function of temperature at different pressures
(CO_2 + H_2O + NaCl + KCl) system, m = 1.98 mol·kg^{-1}, symbols: ◆, p = 2 MPa; ■, p = 4 MPa; ▲, p = 6 MPa; ×, p = 8 MPa; ✱, p = 10 MPa; ●, p = 12 MPa; ┼, p = 14 MPa; ◇, p = 18 MPa; □, p = 20 MPa; △, p = 30 MPa; ✚, p = 40 MPa; ○, p = 50 MPa

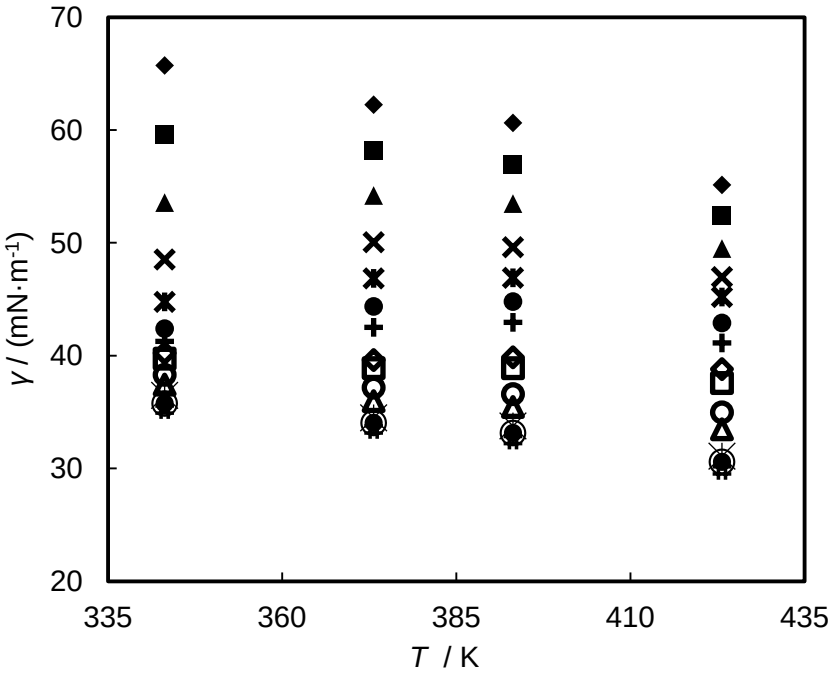

Figure 30. Interfacial tension as a function of temperature at different pressures
CO_2 and $CaCl_2$(aq) at m = 2.5 mol·kg^{-1}, Symbols: ◆, p = 2 MPa; ■, p = 4 MPa; ▲, p = 6 MPa; ×, p = 8 MPa; ✱, p = 10 MPa; ●, p = 12 MPa; +, p = 14 MPa; ◇, p = 18 MPa; □, p = 20 MPa; △, p = 30 MPa; ○, p = 50 MPa

Expressions for the derivatives γ with respect to temperature and pressure may be obtained from the Gibbs-Duhem equation applied to the surface phase and to the two bulk phases. Since, in the present case, these derivatives are only weakly dependent upon the salt molality, it is sufficient to consider the binary (H_2O + CO_2) system. It is shown in the appendix that, for a system containing two components of low mutual solubility, $-(\partial\gamma/\partial T)p$ is proportional to the excess molar entropy of the surface phase, while $(\partial\gamma/\partial p)T$ is proportional to the excess molar volume of the surface phase. Thus the present results give an indication of the sign of these excess properties of the surface phase. See the deduction in of it Appendix B.

3.6.4 CO_2 and brine IFT dependence on the salinity of brines

The effect of salinity (both ion type and concentration) on water surface tension under ambient conditions is documented in the literature [108, 109]. The present results indicate that the interfacial tension increases with salinity and always exceeds that of salt-free water at the same pressure and temperature. Indeed, our results clearly show that at every temperature and pressure investigate, γ increases *linearly* with the salt concentration. This behaviour is exemplified by the results at T = (343.15 and 373.15) K shown in Figure 31 and Figure 32 respectively. Data for zero molality of salt from [97] are also plotted in these figures and fall precisely in line with the linear trends exhibited by our data for finite molality.

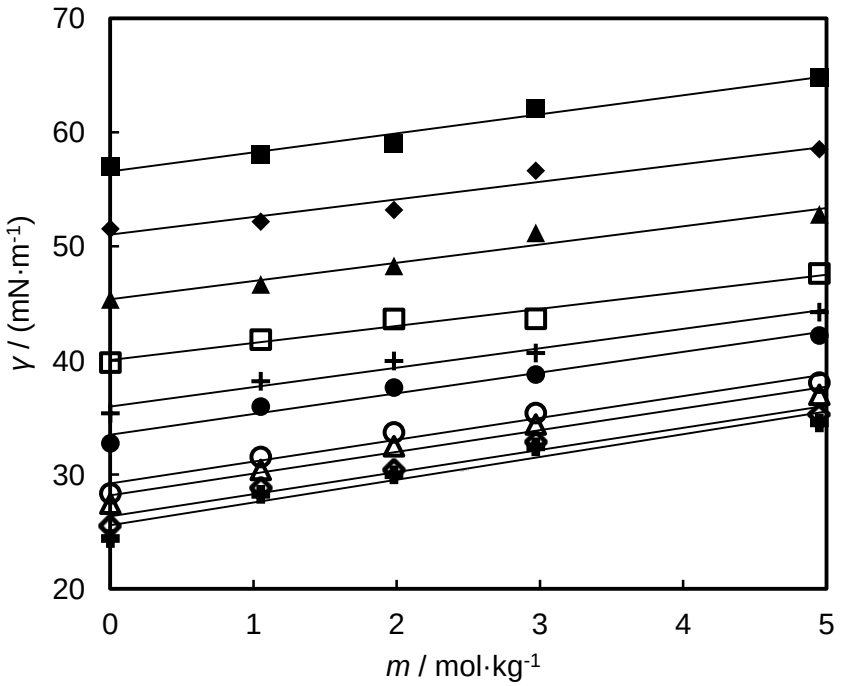

Figure 31. Interfacial tension as a function of salinity (CO_2 + H_2O + NaCl + KCl) system, , at T = 343.15 K, symbols: ■, p = 2 MPa; ◆, p = 4 MPa; ▲, p = 6 MPa; □, p = 8 MPa; ┼, p = 10 MPa; ●, p = 12 MPa; ○, p = 20 MPa; △, p = 25 MPa; ◇, p = 35 MPa; ✚, p = 40 MPa. Solid lines are linear fits to the data.

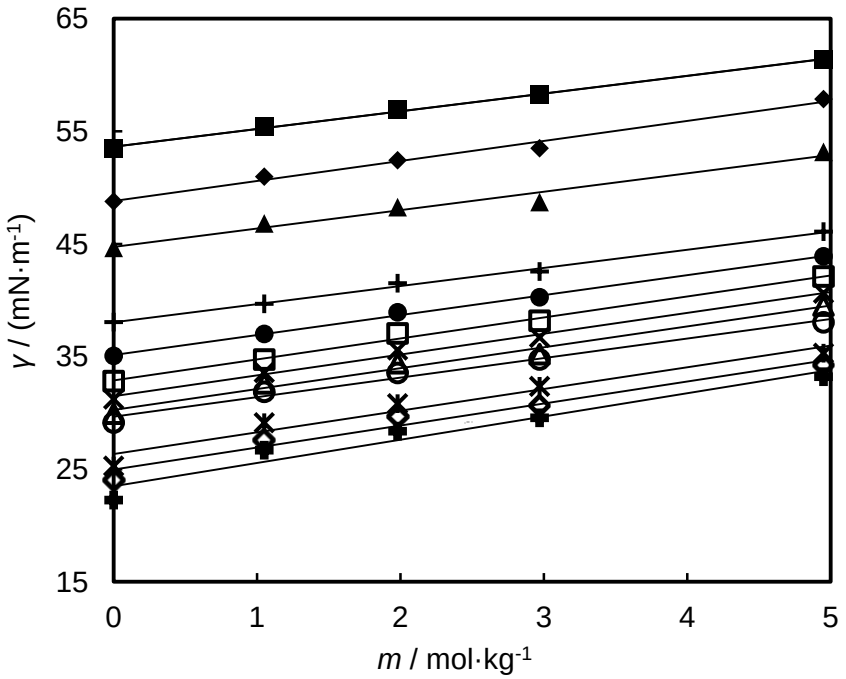

Figure 32. Interfacial tension as a function of salinity (CO_2 + H_2O + NaCl + KCl) system, , at T = 373.15 K, symbols: ■, p = 2 MPa; ◆, p = 4 MPa; ▲, p = 6 MPa; ┼, p = 10 MPa; ●, p = 12 MPa; □, p = 14 MPa; ×, p = 16 MPa; △, p = 18 MPa; ○, p = 20 MPa; ∗, p = 30 MPa; ◇, p = 40 MPa; ✚, p = 50 MPa. Solid lines are a linear fits to the data.

However, again at constant temperature and pressure, different salts can exhibit the same or different effects on the IFT. For example, $CaCl_2$, $MgCl_2$ and Na_2SO_4 all behave essentially the same but have a larger effect than brines containing NaCl and KCl. Figure 33 compares the results for $CaCl_2$(aq) at m = 2.5 mol·kg^{-1} with (0.864 NaCl + 0.136 KCl)(aq) at m = 5.0 mol·kg^{-1} as a function of time after creation of the drop at T = 423.15 K and p = 2 MPa. It is observed that the IFT of CO_2 against both brines are essentially identical at γ = (54.2 ± 0.2) mN·m^{-1}. The present results also show that $MgCl_2$(aq) and $CaCl_2$(aq) behave almost identically at the same temperature, pressure and molality.

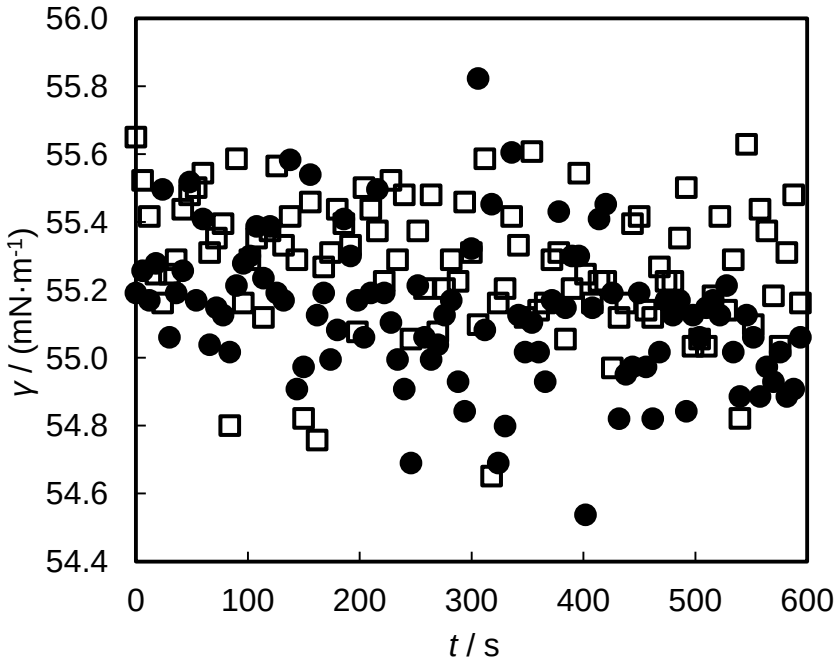

Figure 33. Interfacial tension as a function of time
T = 423.15 K and p = 2 MPa: ●, CO_2 + $CaCl_2$(aq) at m = 2.5 mol·kg^{-1}; □, CO_2 + (0.864 NaCl + 0.136 KCl)(aq) at m = 4.95 mol·kg^{-1}

Figure 34 compares the IFT data for CO_2 with $CaCl_2$(aq) and $MgCl_2$(aq), both at m = 2.5 mol·kg^{-1}, and (0.864 NaCl + 0.136 KCl)(aq) at m = 5 mol·kg^{-1}, as functions of pressure along isotherms at T = (343, 373 and 423) K. The results for each brine system appear to be the same to within the experimental uncertainty.

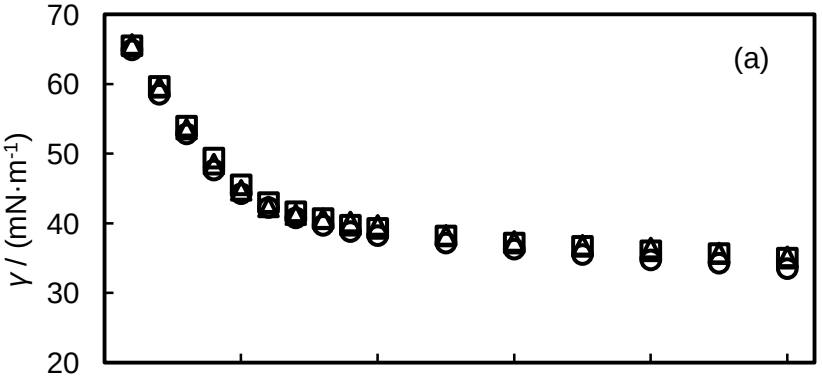

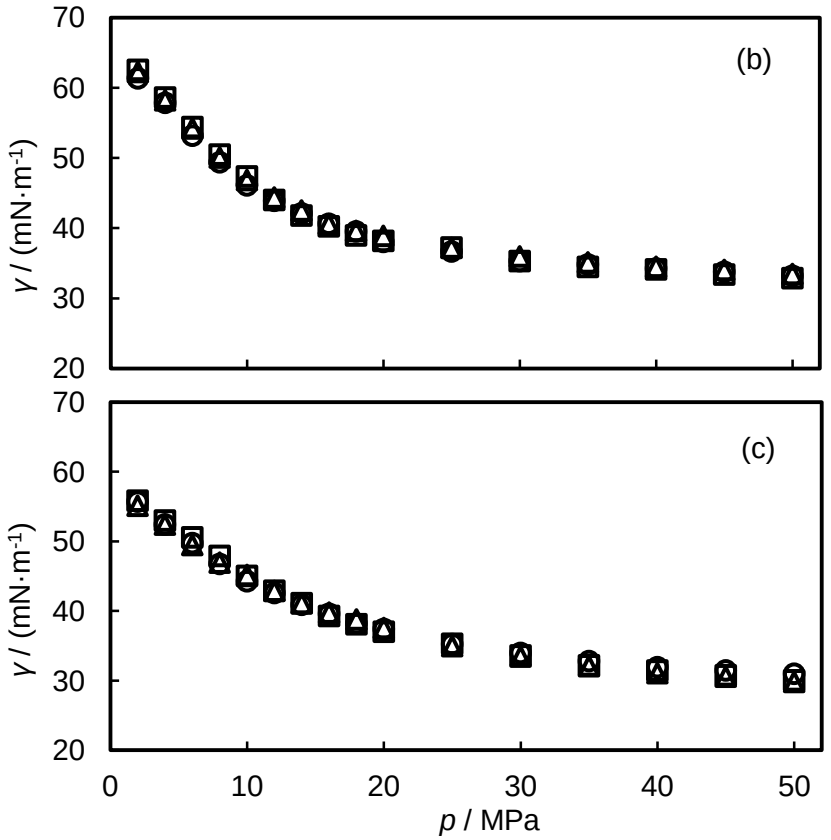

Figure 34. Interfacial tension between CO_2 and three different brines as a function of pressure on different isotherms
(a), T = 343.15 K: (b), T = 373.15 K; (c), T = 423.15 K. △, $CaCl_2$(aq) at m = 2.5 mol·kg^{-1}; O, (0.864 NaCl + 0.136 KCl)(aq) at m = 4.95 mol·kg^{-1}; □, $MgCl_2$(aq) at m = 2.5 mol·kg^{-1}

In view of the behaviour observed experimentally, we propose that the IFT between CO_2 and brines containing the chlorides or sulphates of Na, K, Mg and Ca may be represented as a linear function of the positive-charge molality, m^+, which may be defined for a mixed brine by

$$m^+ = \sum_{i=1}^{n} z_i m_i \,. \tag{3.19}$$

Here, m_i is the molality and z_i is the charge number of the ith cation, and n is the number of cationic species present in the brine. Thus, for a single

salt $M_{\nu}^{z+}X_{(z/y)\nu}^{y-}$, m^+ is the product of the stochiometric number ʋ and the charge number z of the cation M. On grounds of electrical neutrality, the negative-charge molality is identical. Figure 35 illustrates the proposed relation. Here we plot as a function of m^+ at T = 373.15 K and various pressures the IFT of pure water (from Georgiadis [97]), $CaCl_2$(aq) and (0.864 NaCl + 0.136 KCl)(aq) (reported previously [166]). A good linear correlation is observed at every pressure. The results for both $MgCl_2$(aq) and Na_2SO_4(aq) also obey the same relation.

At a molecular level, the explanation for the observed behaviour may be that the ions, being excluded from the CO_2-rich phase, have a negative affinity for the interface and are restricted to the bulk of the aqueous phase. The resulting gradient in ionic strength near the interface leads to an enhanced attraction of the water molecules towards the bulk of the aqueous phase, thereby increasing the work required to expand the interfacial area and amplifying γ. This effect is expected to increase with both ion concentration and ion charge. The special ion effect on surface tension has been studied for brine systems under ambient condition by several authors [108, 109, 167-170].

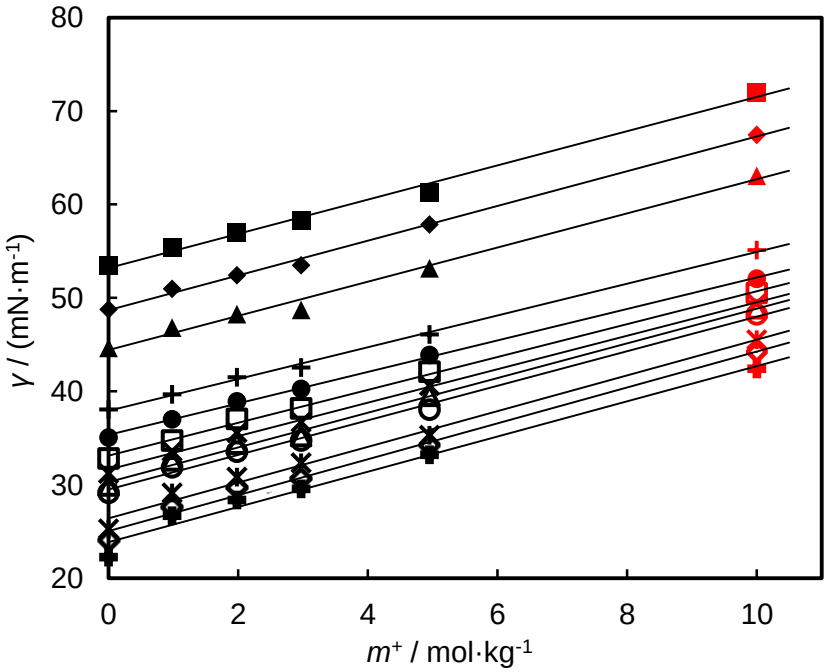

Figure 35. Interfacial tension of (CO_2 + brine) as a function of the positive charge molality
at T = 373.15 K: ■, p = 2 MPa; ◆, p = 4 MPa; ▲, p = 6 MPa; +, p = 10 MPa; ●, p = 12 MPa; □, p = 14 MPa; ×, p = 16 MPa; △, p = 18 MPa; ○, p = 20 MPa; ∗, p = 30 MPa; ◇, p = 40 MPa; ✚, p = 50 MPa. Black symbols refer to (0.864 NaCl + 0.136 KCl)(aq) and red symbols refer to $CaCl_2$(aq)

But the above conclusion is only applicable to strong electrolyte. Our measurement on $NaHCO_3$ solution and brine was found to behave differently from the above mentioned brines. Here we compared (CO_2 + $NaHCO_3$)(aq) at m = 0.98 mol·kg^{-1} with (CO_2+NaCl+KCl)(aq) at m = 1.98 mol·kg^{-1} at different isotherms (343 K, 373 K, 393 K and 423 K). The pressure dependence plots are shown in Figure 36. Form this figure it can be seen that at 343 K, the two systems have different interfacial tensions, however this difference disappeared as the temperature increases. The explanation of this behaviour may be that the concentration of Na^+ remained constant with changing temperature, while the concentration of gaseous CO_2 decreases with increasing temperature,

which shifts the equilibrium of the bicarbonate system. The bicarbonate system has the following equilibrium relationship: $HCO_3^- = CO_3^{2-} + H^+$

and,

$$CO_2 + H_2O = HCO_3^- + H^+$$

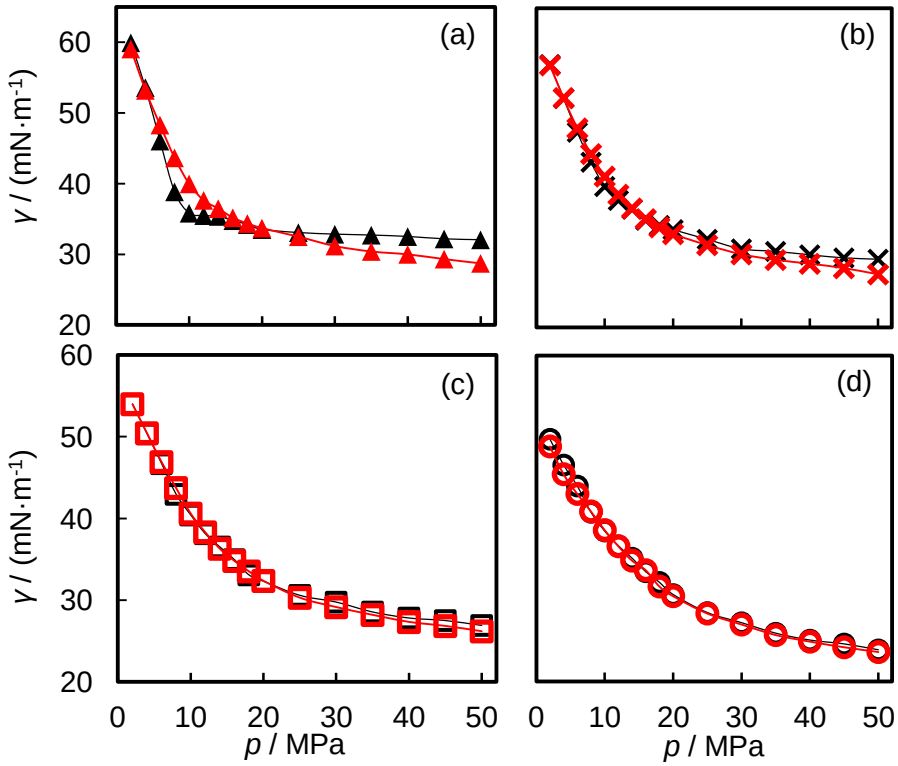

Figure 36. Interfacial tensions as a function of pressure at different isotherms
(a), T = 343.15 K; (b), T = 373.15 K; (c), T = 393.15 K; (d), T = 423.15 K. Black symbols: (CO_2 + $NaHCO_3$)(aq) m = 0.98 mol·kg^{-1}; red symbols: (CO_2+NaCl+KCl)(aq) m = 1.98 mol·kg^{-1}

Therefore, when the concentration of dissolved gaseous CO_2 decrease the amount of dissociated carbonate species decreases (i.e. increasing the pH) which could explain the observed behaviour. However, due to the fact that bicarbonate has relative low solubility in water, the behaviour of bicarbonate ion in complex brine does not dominate the behaviour of brine.

3.7 Empirical model of CO_2 and brine IFT

In this chapter, two different empirical models for predicting the interfacial tensions between brine and CO_2 are provided.

The first model is an empirical fitting of the experimental data base on the linear dependence of IFT on the positive charge concentration. With this model, the IFT can be calculated directly by given brine salinity, temperature , $T > T_c(CO_2)$, and pressure.

The second model is based on both the linear relationship between IFT and positive charge concentration and the relation between salt free IFTs and the solubility of CO_2 in water. With this model, IFT of brine and CO_2 could be calculated by give temperature, pressure, brine salinity, and the CO_2 solubility in water under the same conditions.

3.7.1 Empirical model 1

For practical purposes, it is useful to have an empirical equation to describe the variation of γ with temperature, pressure and salinity. From the discussion in last section, it is clear that for the same type of ions, the present results can be correlated as a linear function of molality as follows:

$$\gamma/\left(\mathrm{mN}\cdot\mathrm{m}^{-1}\right)=A\left[m/\left(\mathrm{mol}\cdot\mathrm{kg}^{-1}\right)\right]+B \tag{3.20}$$

For different type of ions but strong electrolyte, the same function as above is applicable, with the same parameters, but generalizes it by replacing total salt molality m by the positive-charge molality m^+. The correlation is therefore written

$$\gamma/(\mathrm{mN}\cdot\mathrm{m}^{-1})=A[m^{+}/(\mathrm{mol}\cdot\mathrm{kg}^{-1})]+B \tag{3.21}$$

Here A and B are functions of temperature and pressure, the latter representing γ/(mol·kg^{-1}) for the (CO_2 + H_2O) system. Considering all of

the data at $T \geq 323.15$ K, the following expressions, containing in total 12 parameters, were obtained

$$A = a_0 + a_1\left(p/\mathrm{MPa}\right) + a_2\left(T/\mathrm{K}\right) \tag{3.22}$$

and B, representing γ/(mN·m^{-1}) for the (CO_2 + H_2O) system, is given by

$$\begin{aligned} B = {} & [b_{00} + b_{01}(T/\mathrm{K}) + b_{02}(T/\mathrm{K})^2] + \\ & [b_{10} + b_{11}(T/\mathrm{K})](p/\mathrm{MPa})^{-1} + \\ & [b_{20} + b_{21}(T/\mathrm{K})](p/\mathrm{MPa})^{-2} + \\ & [b_{30} + b_{31}(T/\mathrm{K})](p/\mathrm{MPa})^{-3} \end{aligned} \tag{3.23}$$

The parameters appearing in Eq. (3.22) and (3.23) are given in Table 4, and the ranges of validity for the correlation are $323.15 \leq T/\mathrm{K} \leq 448.15$ and $p \leq 50$ MPa.

Eq. (3.21) was used, to predict the IFT of the brines investigated in this work and the relative deviations are shown in figure 37, 38 and Figure 39. The average absolute relative deviation for the entire data set is 2% with the majority of the data predicted within ± 3%. Thus we deduce that Eq. (3.21) may be useful in predicting the IFT of other (CO_2 + brine) systems at positive-charge molalities up to about 10 mol·kg^{-1}, subject to the restrictions on temperature and pressure noted above.

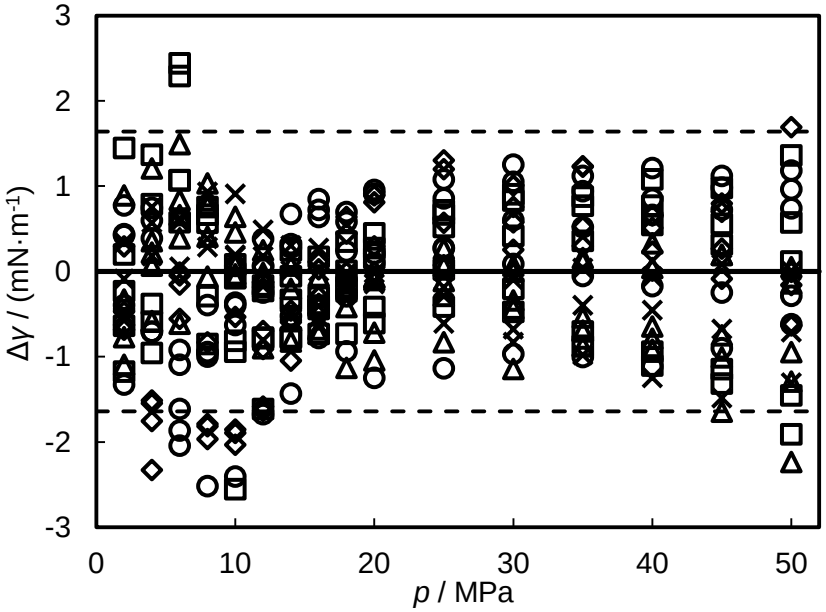

Figure 37. Deviation of the interfacial tensions from the fitting Eq (3.21) (CO_2 + H_2O + NaCl + KCl) system, symbols: ◇, T = 323.15 K; □, T = 343.15 K; △, T = 373.15 K; ×, T = 393.15 K; ○, T = 423.15 K

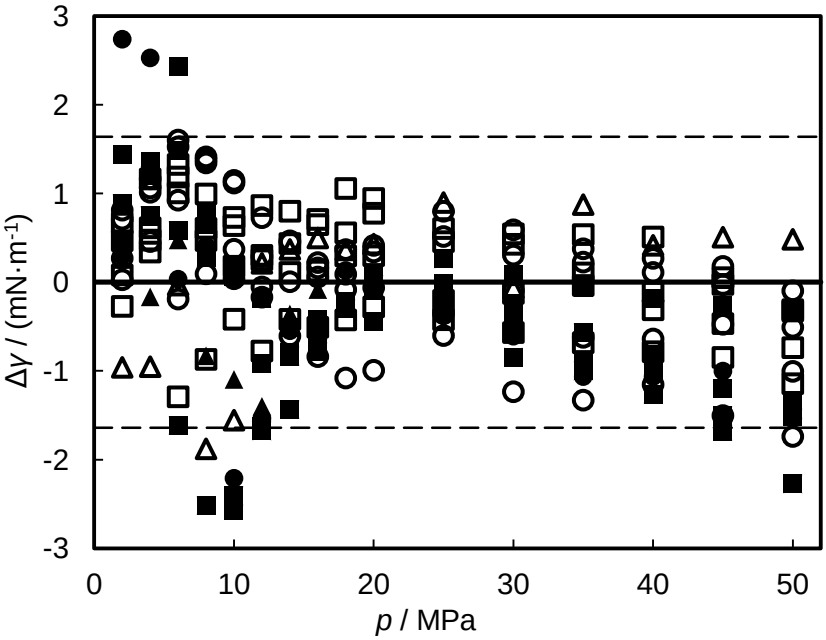

Figure 38. Deviations of the interfacial tension from the predictions of Eq (3.21)
different (CO_2 + brine) systems, symbols: ○, $CaCl_2$(aq) and $MgCl_2$(aq) at m^+ = 5.0 mol·kg^{-1}; ●, $CaCl_2$(aq) and $MgCl_2$(aq) at m^+ = 10.0 mol·kg^{-1}; △,

Na_2SO_4(aq) at m^+ = 0.98 mol • kg^{-1}; ▲, Na_2SO_4(aq) at m^+ = 1.96 mol • kg^{-1}

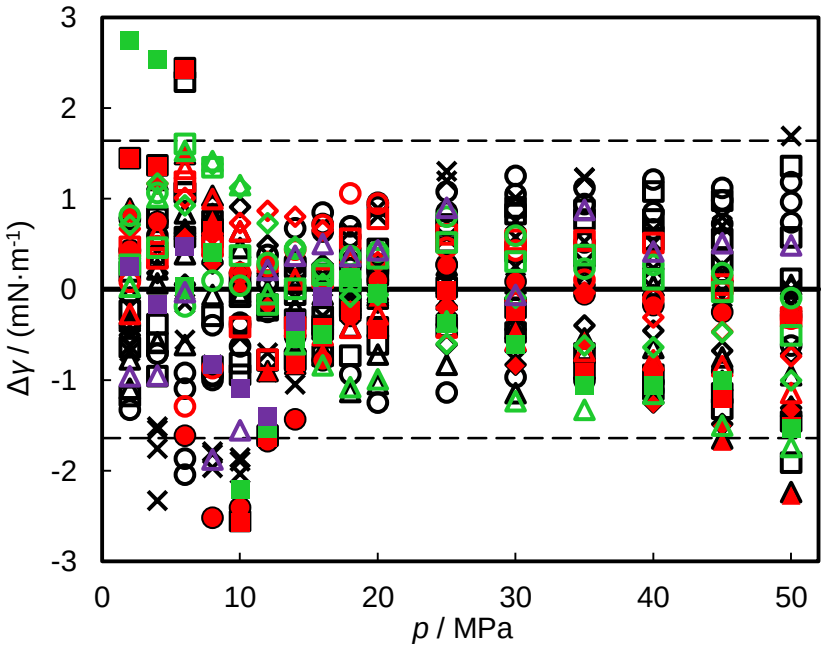

Figure 39. Deviations of the interfacial tension from the predictions of empirical model 1
different (CO_2 + brine) systems, Black symbols, (0.864 NaCl + 0.136 KCl)(aq); Red symbols, $CaCl_2$(aq); Green symbols: $MgCl_2$(aq); Purple symbols, Na_2SO_4(aq)

Table 4. Parameters in Eq. (3.22) and (3.23) for the correlation of the interfacial tension.

a_0	4.51010×10^{-01}
a_1	6.2018×10^{-03}
a_2	3.3654×10^{-03}
b_{00}	$-4.1203\times10^{+01}$
b_{01}	4.3549×10^{-01}
b_{02}	-7.2502×10^{-04}
b_{10}	$-5.3890\times10^{+02}$
b_{11}	$2.0305\times10^{+00}$
b_{20}	$3.8312\times10^{+03}$
b_{21}	$-1.1694\times10^{+01}$
b_{30}	$-5.1659\times10^{+03}$
b_{31}	$1.5073\times10^{+01}$

3.7.2 Empirical model 2

The basic structure of empirical model 2 is the same as model 1, which can be written as,

$$\gamma/\left(\mathrm{mN}\cdot\mathrm{m}^{-1}\right)=A\left[m/\left(\mathrm{mol}\cdot\mathrm{kg}^{-1}\right)\right]+B \tag{3.24}$$

For different type of strong electrolytes, the total salt molality m could be replaced by the positive-charge molality m^+,

$$\gamma/(\mathrm{mN}\cdot\mathrm{m}^{-1})=A[m^+/(\mathrm{mol}\cdot\mathrm{kg}^{-1})]+B \tag{3.25}$$

Here A is functions of temperature and pressure,

$$A=a_0+a_1\left(p/\mathrm{MPa}\right)+a_2\left(T/\mathrm{K}\right)+a_3\left(p/\mathrm{MPa}\right)^{-0.5} \tag{3.26}$$

And B represents γ/(mol·kg^{-1}) for the (CO_2 + H_2O) system. From empirical model 1, the interfacial tensions of water and CO_2 were calculated and compared with literature data, as shown in Figure 40.

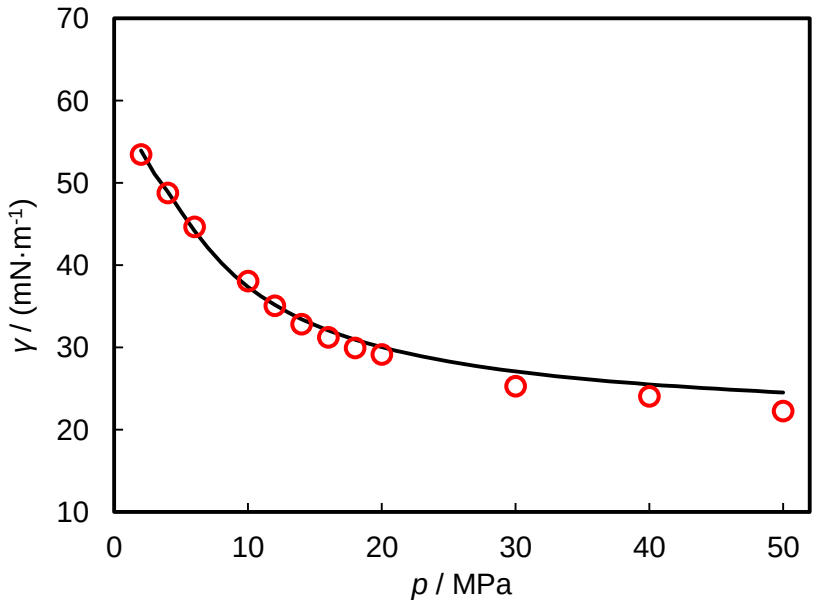

Figure 40. Calculated interfacial tension of water and CO_2 at T = 373 K Solid line, empirical equation; ○, reference data [64]

In theory, this interfacial tension is depending only on the temperature and pressure in saturated systems. Considering that the surface tension of water is only depending on pressure, we explored the relationship between CO_2 solubility in water and the IFT of water and CO_2. Table 5 is the list of the difference between pure water surface tension and the interfacial tension between water and CO_2, $\Delta\gamma$, deduced from empirical model 1.

Table 5. Surface tension of water and its difference with the interfacial tension of CO_2 and water

Water surface tension						
T / K	298.15	323.15	343.15	373.15	393.15	423.15
γ_w mN·m^{-1}	72.0	67.9	64.5	58.9	55.0	48.7
The difference of water surface tension and the interfacial tension of water and CO_2. $\Delta\gamma = (\gamma_w - \gamma_{wc})$ / (mN·m^{-1})						
T / K \ p / MPa	298.15	323.15	343.15	373.15	393.15	423.15
2	51.7	58.0	56.1	53.0	50.8	45.0
4	40.0	50.5	50.2	48.4	47.3	41.9
6	29.1	43.6	45.3	44.3	43.9	39.7
8	25.2	37.6	39.7	40.2	40.8	38.0
10	23.9	35.0	37.1	37.2	37.8	35.8
12	23.4	33.0	34.5	35.5	35.4	33.5
14	22.6	32.1	33.2	33.4	33.5	31.5
16	21.8	31.6	32.0	32.0	31.9	29.9
18	21.4	31.1	31.1	30.7	30.2	28.0
20	21.1	30.8	30.7	29.8	29.0	26.6
25	20.5	30.1	29.7	28.6	26.6	24.4
30	18.8	28.9	28.8	26.9	25.7	23.0
35	17.1	28.8	28.3	26.4	24.9	21.7
40	14.6	27.4	27.8	25.6	24.1	20.8
45	13.9	27.5	27.2	25.3	23.6	20.2
50	13.0	27.8	26.9	24.8	22.8	19.7

Even though no universal curve was found, it was found that these differences are correlated with the solubilities [171] of CO_2 in water under the same temperature and pressure conditions, as shown in Figure 41. Surprisingly, at each isotherm these differences are linearly depending on the solubility of CO_2 in water.

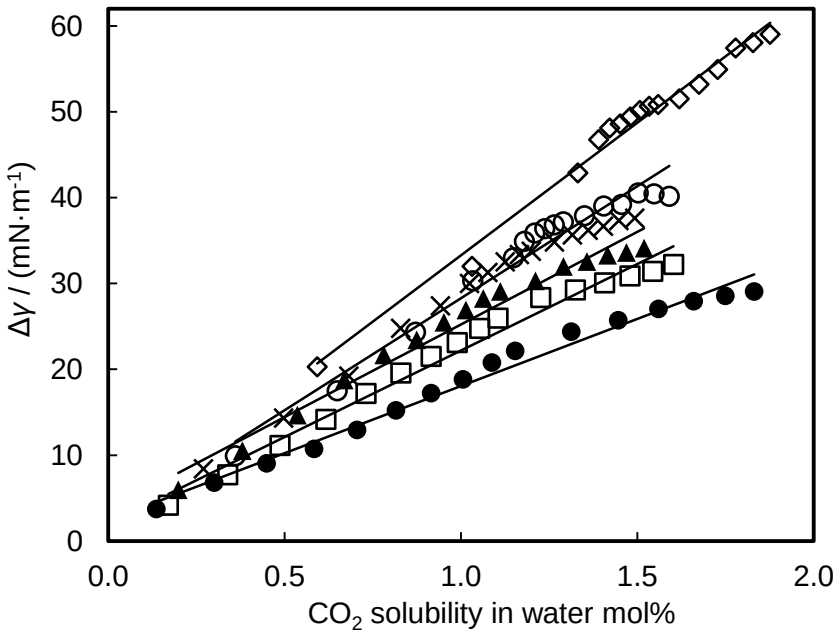

Figure 41. The difference of water surface tension and the interfacial tension between water and CO_2 dependence on CO_2 solubility in water symbols: ◇, T = 298.15 K; O, T = 323.15 K; ×, T = 343.15 K; ▲, T = 373.15 K; □, T = 393.15 K; ●, T = 423.15 K

It was also noticed that the slope of each linear line decreases with increasing temperature. We describe this relationship as below,

$$B = \gamma_{\text{water}} - Cx_{\text{CO}_2} \tag{3.27}$$

Here γ_{water} is the surface tension of water under the same temperature, and x_{CO2} is the solubility of CO_2 in water under the same temperature and pressure, while C is the slope of $\Delta\gamma$ in relation with x_{CO2} respectively. Further on, C can be written as a function of temperature,

$$C = d\left(T/\text{K}\right) + e \tag{3.28}$$

The correlation between C and temperature is shown in Figure 42, d and e are the slope and intercept of C relative with temperature respectively.

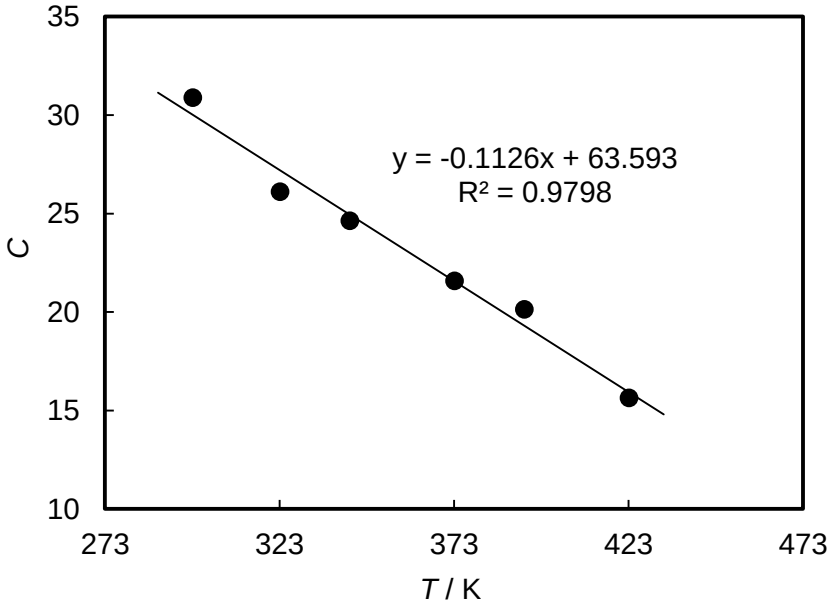

Figure 42. Correlation of *C* and temperature

Considering all of the data at 293.15 K ≤ *T* ≤ 423.15 K, the following expressions, containing in total 7 parameters, appearing in Eq (3.26), (3.27) and (3.28) are given in Table 6 and deviations of the experimental data are shown in Figure 43. The average of the absolute deviation for the experimental data is 1.1 $mN \cdot m^{-1}$ with the vast majority of the data fitted to within 3.49 $mN \cdot m^{-1}$. Nevertheless, a few points exhibit larger, mostly positive, deviations that could not be reduced without adding many additional parameters.

Table 6. Parameters in Eq (3.26). (3.27) and (3.28) for the correlation of the interfacial tension.

parameter	value
a_0	-1.3862E+00
a_1	2.3985E-02
a_2	4.2427E-03
a_3	2.2588E+00
d	-1.1264E-01
e	6.3593E+01

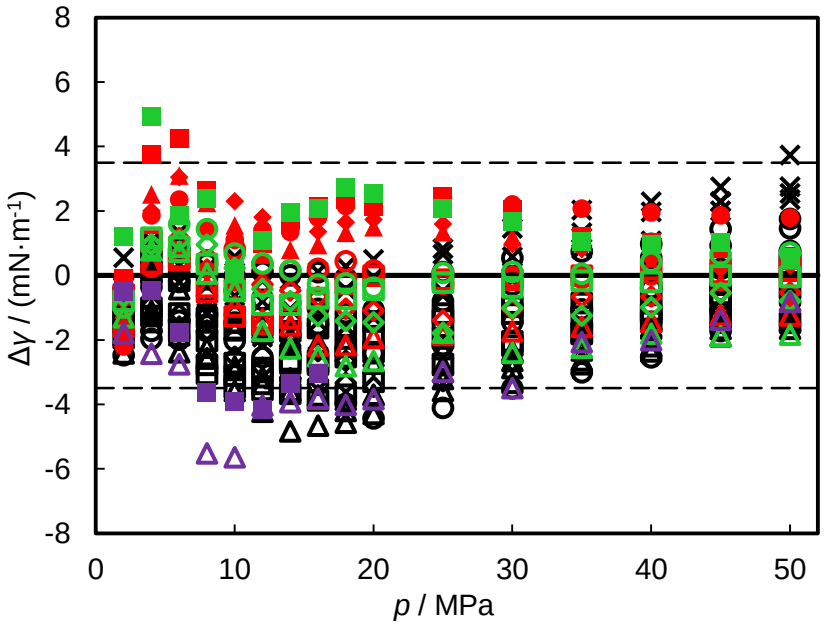

Figure 43. Deviations of the interfacial tension from predictions of empirical model 2
black symbols, (0.864 NaCl + 0.136 KCl)(aq); red symbols, $CaCl_2$(aq);
Green symbols: $MgCl_2$(aq); Purple symbols, Na_2SO_4(aq)

Finally, the interfacial tensions of two synthetic Qatari brine samples, detailed in Appendix E, and CO_2 were measured at 343 K and 393 K. These IFT experimental data were compared with the calculated IFT from empirical model 1 with the same temperature, pressure and positive charge concentration. Figure 44, the comparison of calculated IFTs and experimental IFTs indicated a good prediction of empirical model 1 on complex brines.

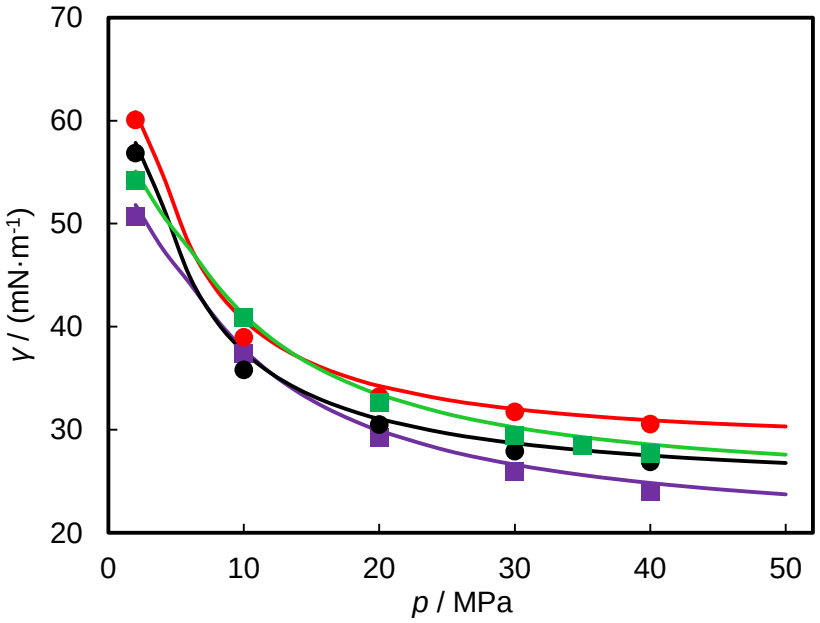

Figure 44. Interfacial tension of Qatari brine (solid line: Empirical model 1, solid symbols: experimental data): Black: low salinity brine at T = 343 K; Purple, low salinity Qatari brine at T = 393 K; Re, high salinity brine at T = 343 K; Green, high salinity brine at T = 393 K

Chapter 4. Molecular dynamics simulation of interfacial tension

Molecular Dynamics simulations were performed to study the interfacial tension between CO_2 and brine for a range of temperatures between 303 K and 393 K and pressures from 2MPa to 50 MPa. The ions involved in this study were Na^+, Ca^{2+} and Cl^-. The results indicate that the interfacial tension decreases with increasing pressure under any temperature condition, but increases linearly with the molality of the salt solution. The density profiles calculated from the MD simulation also indicate a positive excess of CO_2 and a negative excess of ions at the interface. The charge of the ions was found to have a larger influence than their size on the interfacial tension, a result that is consistent with experimental findings.

4.1 Interfacial tension simulation by molecular dynamics

The study of interfacial properties between carbon dioxide and the fluids and minerals present in oil reservoirs and deep saline aquifers is fundamental to a scientific understanding of geological carbon storage. The technologies and practices that have been developed for CO_2-EOR have to some extent applicability in carbon storage processes.

In chapter 3 we explored the IFT of CO_2 and water/brines as a function of temperature and pressure over a wide range of brine salinity [172, 173], and it was found that interfacial tension increases linearly with molality. Further, at constant temperature and pressure, the interfacial tension is the same function of the positive charge molality for all investigated salts, i.e. mixtures of NaCl and KCl, $CaCl_2$, $MgCl_2$ and Na_2SO_4. In this chapter we use MD simulations mainly to validate this dependence on positive charge molality, i.e. ions would be concentrated in the bulk but not in the interface, otherwise different molecular weights should make a difference

on IFT. We used MD simulations to obtain deeper insight into the reasons for different dependence of interfacial tension on temperature, pressure and the salinity of brines.

Molecular Dynamics simulations of pure water and CO_2 system have been carried out by various authors [63, 150, 174-177]. The surface tension of water has been investigated by Chen *et al*. [178] with different water models. The interfacial tension of pure water and CO_2 system was studied by Nielsen *et al*.[179]. However to date it appears that no MD studies have been performed on the brine (water and salt) and CO_2 system under reservoir conditions.

4.2 Models for intermolecular potentials

4.2.1 Force field selection

Two typical water models, SPC/E [180] and TIP4P[181] were investigated together with the EPM2 model for CO_2 [150, 176, 182-184]. The SPC/E force field was chosen because of its ability to reproduce water self-diffusion, dissolved CO_2 solvent structure [175], orthobaric density [149], static dielectric constant [185], and *pVT* properties up to high pressures [186], and because it provides one of the best predictions of the vapor–liquid IFT of water [178, 187]. Despite some early, now controversial, results indicating that the SPC/E model accurately reproduces the water vapor-liquid IFT [149], most simulations of water vapor-liquid IFT using the SPC/E force field underestimate the vapor-liquid by up to 10 $mN \cdot m^{-1}$ [178, 187]. Indeed, most commonly used fixed-charge water models significantly underestimate the surface tension of liquid water. The TIP4P water model has been shown to provide a better estimate of water vapour-liquid IFT [187], so this water model was also selected for comparison. The EPM2 model for carbon dioxide was chosen because of its good prediction of the vapor-liquid coexistence curve [183]. The EPM2 CO_2 molecules were treated in the simulation by

adding two dummy sites to the molecules carrying the total mass of the molecule [183], while the carbon and oxygen atoms have zero mass but carry the 6-12 Lennard-Jones parameters and atoms charges. The 6-12 Lennard-Jones parameters of the ions explored in this study are obtained from the OPLS-AA all-atom force field [188]. These parameters together with EPM2 CO_2 used in this study are summarized in Table 7.

Table 7. Lennard-Jones parameters of atoms

atoms	σ (nm)	ε (kJ·mol^{-1})	charge (e)	mass (g·mol^{-1})
Ions				
Na^+	0.333045	0.011598	1.000	22.98977
Ca^{2+}	0.241203	1.88136	2.000	40.08000
Cl^-	0.441724	0.492833	-1.000	35.45300
EPM2 CO_2				
D1	0	0	0	22.00475
D2	0	0	0	22.00475
C	0.2757	0.23379	0.6512	0
O	0.3033	0.66912	-0.3256	0

4.2.3 Interfacial tension

During the NVT simulation, the interfacial tension was determined by the principal components of the MD simulation cell stress tensor, as detailed in Harries *et al*. [147], Matsumoto *et al*. [189] and Kuznetsova *et al*. [150]:

$$\gamma = \frac{1}{2} L_Z \left[P_{zz} - \frac{1}{2}\left(P_{xx} + P_{yy}\right) \right] \tag{4.1}$$

where L_z (nm) is the box length in the Z direction and $P_{\alpha\alpha}$ is the αα component of the pressure tensor. A sketch of simulation was shown in Figure 45, where z direction is normal to the two brine and CO_2 interfaces.

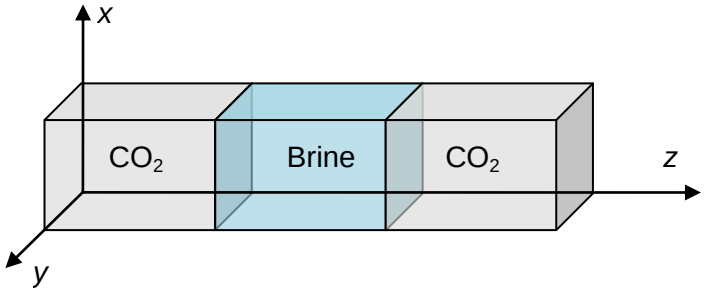

Figure 45. Sketch of simulation domain configuration

4.2.2 Simulation methods

This study was performed with the GROMACS 4.4.5 MD simulation code [114] using periodically boundary conditions. For the NaCl(aq) and CO_2 system, two different brine salinities were studied, which are 1.73 $mol \cdot kg^{-1}$ and 3.46 $mol \cdot kg^{-1}$. For the $CaCl_2$(aq) and CO_2 system, we have the same amount of water, CO_2 and Cl^- molecules as in the NaCl(aq) and CO_2 systems.

Before carrying out the systematic study with a large range of temperature and pressure variation, the system size was optimized by comparing simulation results containing different numbers of water molecules under certain temperature and pressure conditions, while the number of CO_2 molecules is always adjusted according with the pressures. We found that the systems containing 1024 and 4096 water molecular gave similar results, while a smaller system containing 512 water molecules yields different simulation results due to the small amount of water molecular in the system. In Figure 46, we present the interfacial tension of water and CO_2 as a function of pressure. The simulation was initialized by placing all the particles in a control box for NPT simulation. After reaching a dynamic equilibrium, the dimensions of the box were fixed and a further 10 ns NVT simulation was performed, from which the final results were obtained.

During the simulation, the Nose-Hoover extended ensemble was used for temperature coupling. The Parrinello-Rahman method was used for pressure coupling in the NPT simulation [114]. In this scheme the simulation box vectors are subject to an equation of motion and no instantaneous scaling takes place. The pressure coupling is governed by the time constant t_p [ps], associated with the period of pressure fluctuations at equilibrium. An anisotropic pressure coupling type was used and only the z dimension oscillated in the simulation. To avoid large oscillations which may occur especially at a pressure near to the critical pressure of CO_2, the initial volume of the box was very carefully set with reference fluid densities [190]. Meanwhile, a total compressibility of the system was given by interpolating the compressibility of each phase from reference[190].

For both NPT and NVT simulations, the long-range Coulomb intermolecular forces are treated using the particle-mesh Ewald (PME) technique.

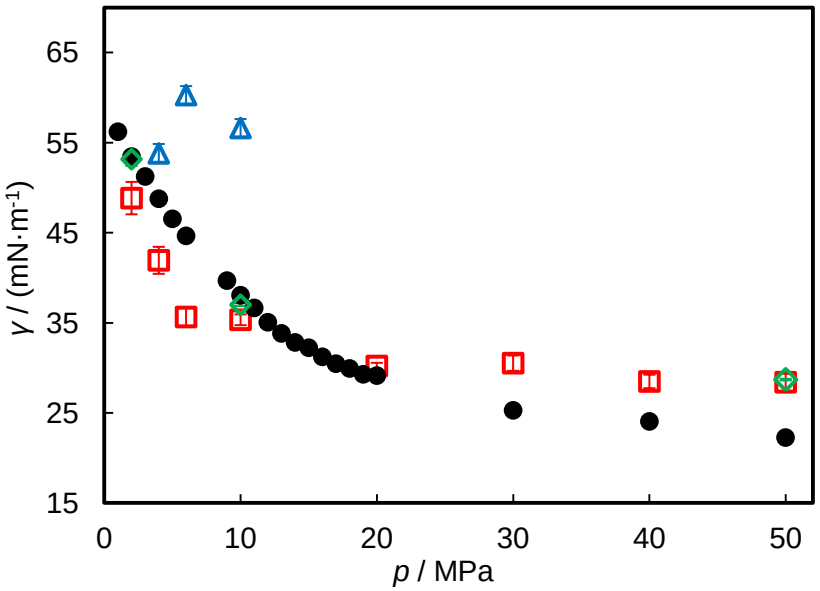

Figure 46. Pressure dependence of interfacial tension of SPC/E-EPM2 system with different particle numbers

T = 373 K. Symbols (number of water molecules/number of CO_2 molecules): △, 512/256; □, 1024/512; ◇,4096/2048; ●, reference [97]

4.2 Results and discussion

In the following sections, we will present our results on density profile and surface excess, pressure and temperature dependence, brine salinity dependence and solubility.

4.2.1 Density profile and surface excess

In Figure 47, we present a snapshot of the simulation domain of the brine and CO_2 system at 373 K and 2 MPa. 128 Ca^{2+}, 256 Cl^-, 4096 SPC/E water and 512 EPM2 CO_2 molecules are within the control box. The system has dimensions of 5×5×51.73 nm in *x, y* and *z* directions respectively. The condensed phase in the centre is brine and the less dense phase is CO_2 rich gas.

A detailed density profile of the interface is calculated from the GROMACS simulations, as shown in Figure 48. This density profile yields a 2 nm interface. A positive excess of CO_2 can be observed together with a negative excess of ions. Similar phenomena were found for NaCl(aq) and CO_2 systems at different temperatures and pressures.

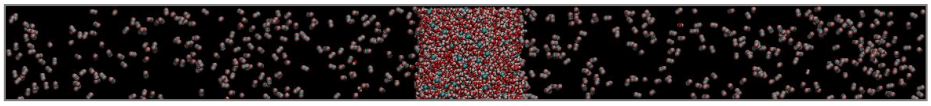

Figure 47. Snapshot of the simulation domain of a brine-CO_2 system equilibrated at m = 3.46 mol·kg^{-1}; T = 373 K, p = 2 MPa. Particle numbers: Ca^{2+}: 128; Cl^-: 256; Water SPC/E: 4096; CO2 EPM2: 512

The excess of CO_2 on the interface is explained by the regular orientation of water molecules on the interface, and the attraction between these regular water molecular array on the surface attract CO_2 molecules with stronger average force than the bulk phase.

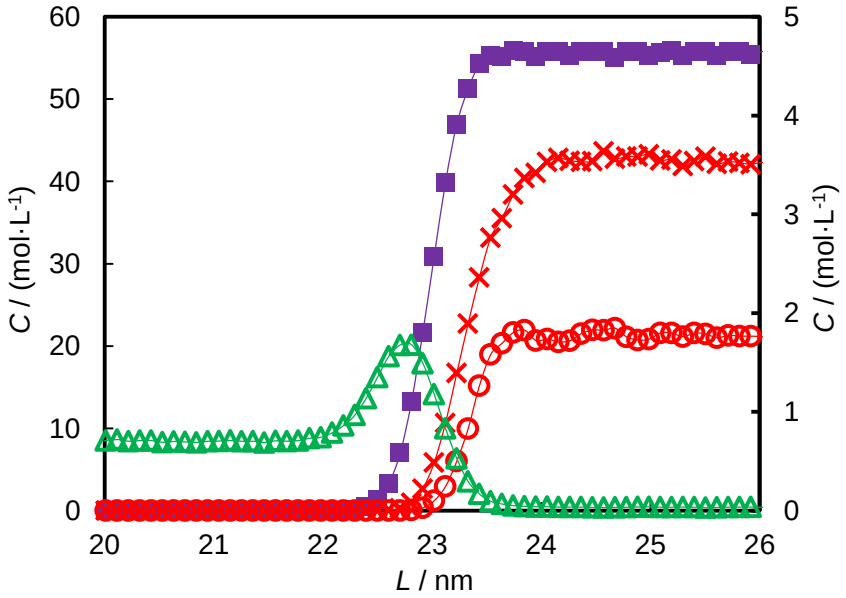

Figure 48. Density profile of brine-CO_2 interface simulation equilibrated at T = 373 K, p = 2 MPa. The molar concentration of water is scaled at the left, and ions and CO_2 are scaled at the right. Particle numbers: Ca^{2+}: 128; Cl^-: 256; Water SPC/E: 4096; CO_2 EPM2: 512. Symbols: ■, water; ×, Cl^-; ○, Ca^{2+}; △, CO_2

The total number of moles of water, CO_2 and ions remain constant in the bulk phases but vary at the surface as shown in Figure 48. The surface excess represents the difference between the total number of moles of the i^{th} component in the system and in a particular phase, CO_2 or brine, and is represented by:

$$\Gamma_i = \frac{n_i^{total} - n_i^{CO_2} - n_i^{brine}}{A} \tag{4.2}$$

where Γ_i is the surface excess of the i^{th} component, n is the number of moles, CO_2 and brine are the phases, and A is the area of the dividing surface. Γ represents the excess of solute per unit area of the surface over the bulk concentration extrapolated to the interface, calculated directly from the density profile. From the density profiles in Figure 48, we observe that Γ_{CO2} is a positive term which has a value of 8.47×10^{-7} mol·m^{-2} but Γ_{ion} is a negative term which is around -5.92×10^{-7} mol·m^{-2}.

4.2.2 Pressure and temperature dependence

We observe that both water models, TIP4P and SPC/E, qualitatively predict the interfacial tension values found experimentally and reported in this work, as shown in Figure 49 Figure 50, and Figure 51. The interfacial tension decreases with increasing pressure when the temperature and brine salinity are constant. However, comparing Figure 49 with Figure 50, using the same number of molecules and the same simulation control parameters, it can be seen that the SPC/E water model gives results that agree better with experiment. Meanwhile the uncertainty from SPC/E model is comparability small than TIP4P water model.

Our previously published experimental results of IFT at high pressures demonstrated that NaCl and $CaCl_2$ brine solutions with the same positive charge concentration gives similar interfacial tension results at different pressures at T = 373 K. The same behaviour was observed at other temperatures as well [172, 173]. Figure 50 shows that the MD simulation results for the interfacial tension of brine and CO_2 is consistent with this dependence on positive charge concentration.

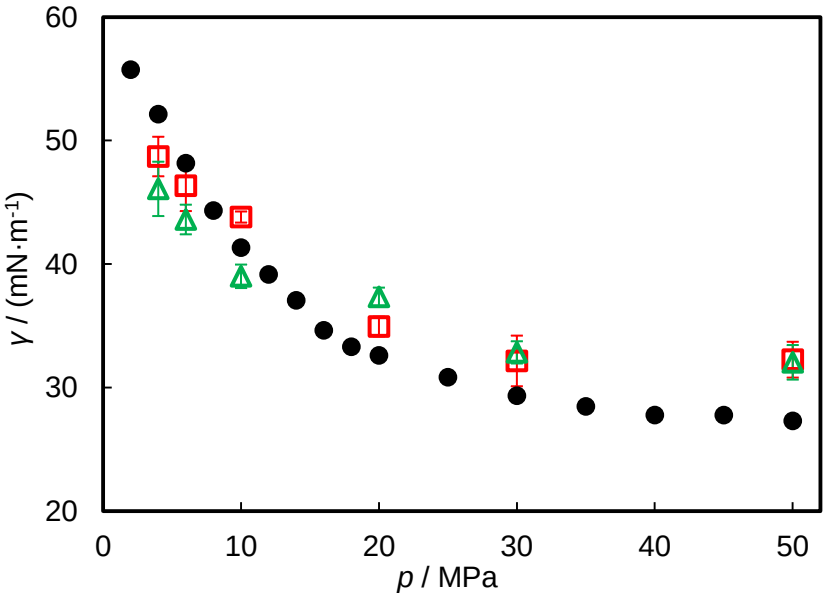

Figure 49. Pressure dependence of interfacial tension of brine and CO_2 system
T = 373 K. Particle numbers: Na^+:16; Ca^{2+}: 8; Cl^-:16; Water SPC/E: 1024; CO_2 EPM2: 512. Symbols: △, MD of NaCl(aq) and CO_2; □, MD of $CaCl_2$(aq) and CO_2; ●, reference [172]

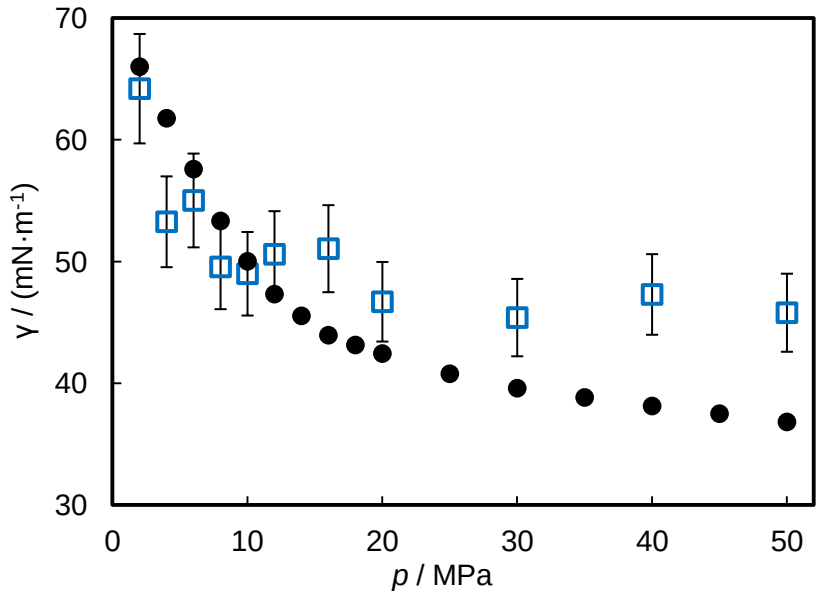

Figure 50. Pressure dependence of interfacial tension between NaCl(aq) and CO_2
T = 373 K. Particle numbers: Na^+:128; Cl^-:128; Water TIP4P: 1024; CO_2 EPM2: 512. Symbols: □, MD of NaCl(aq) and CO_2; ●, reference [172]

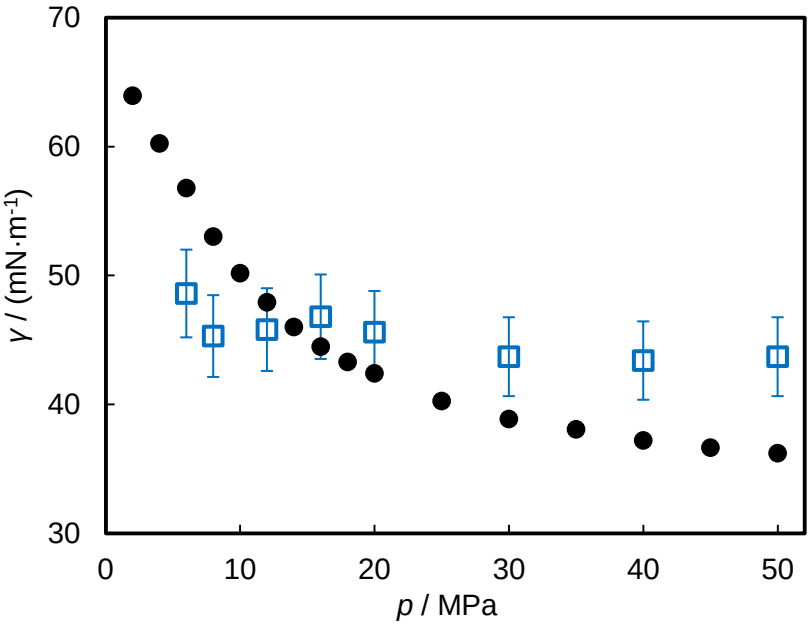

Figure 51. Pressure dependence of interfacial tension between NaCl(aq) and CO_2
T = 393 K. Particle numbers: Na^+:128; Cl^-:128; Water TIP4P: 1024; CO_2 EPM2: 512. Symbols: □, MD of NaCl(aq) and CO_2; ●, reference [172]

4.2.3 Brine salinity dependence

Figure 52 and Figure 53 show the interfacial tension dependence on brine salinity at 373 K and two different pressures respectively. First, we observe that, for the TIP4P water model, the interfacial tensions of brine and CO_2 increase linearly with increasing salt concentration. Second, for different types of ions, the interfacial tension is found to increase linearly with positive charge concentration, regardless of the type of ions.

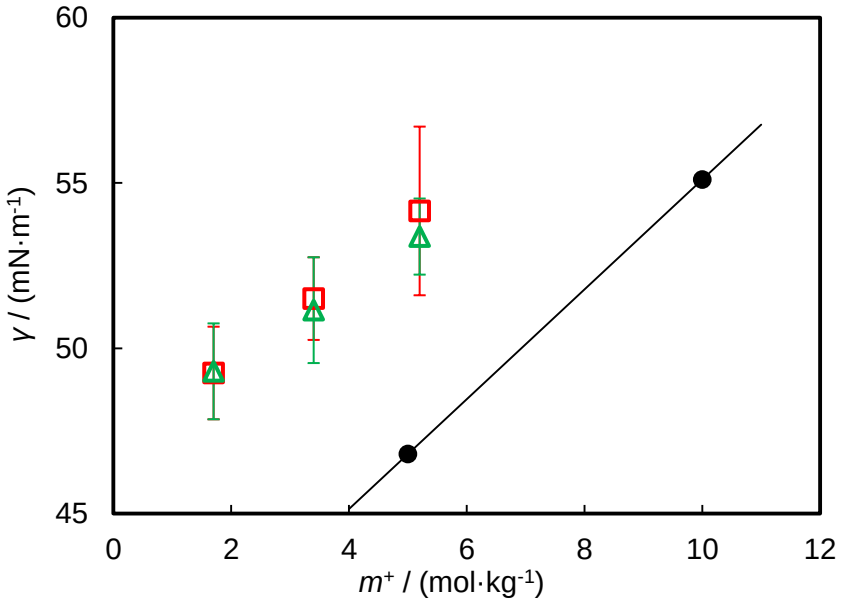

Figure 52. Interfacial tension dependence on brine salinity
T = 373 K, p = 10 MPa. Particle numbers: Water TIP4P: 1024; CO_2 EPM2: 512. Symbols: △, MD of NaCl(aq) and CO_2; □, MD of $CaCl_2$(aq) and CO_2; ●, reference [172, 173]

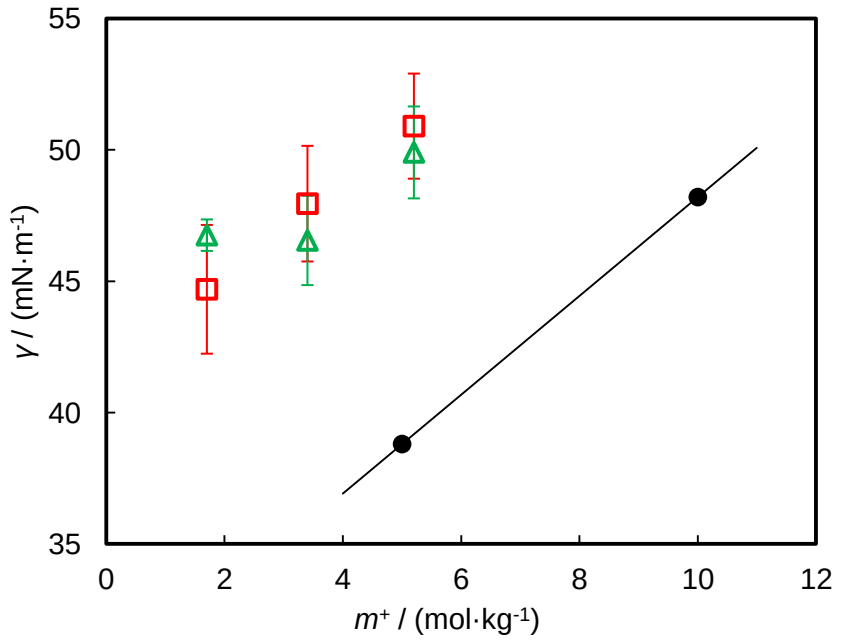

Figure 53. Interfacial tension dependence on brine salinity
T = 373 K, p = 20 MPa. Particle numbers: Water TIP4P: 1024; CO_2 EPM2: 512. Symbols: △, MD of NaCl(aq) and CO_2; □, MD of $CaCl_2$(aq) and CO_2; ●, reference [173]

From the Gibbs adsorption isotherm for multicomponent systems, the concentration of ions, CO_2 and water within the interface are related to the interfacial tension. The Gibbs adsorption equation in terms of surface excess can be written as

$$-d\gamma = \Gamma_{\text{water}} d\mu_{\text{water}} + \Gamma_{CO_2} d\mu_{CO_2} + \Gamma_{\text{ion}} d\mu_{\text{ion}} \tag{4.3}$$

where γ is the interfacial tension, Γ is the interfacial excess and μ is the chemical potential.

This equation indicates that when the surface excess of a component is positive, increasing the chemical potential of that component reduces the interfacial tension; when the surface excess of a component is negative, increasing the chemical potential of that component increases the interfacial tension. In the system of CO_2 and brine, an arbitrary reference plain where has $\Gamma^0_{\text{water}} = 0$ can be found with in the interface zone. Thus the term $\Gamma_{\text{water}}\, d\mu_{\text{water}} = 0$, and Eq. (4.3) can be written as

$$-d\gamma = \Gamma^0{}_{CO_2} d\mu_{CO_2} + \Gamma^0{}_{\text{ion}} d\mu_{\text{ion}} \tag{4.4}$$

As discussed earlier, the MD simulation shows that $\Gamma^0_{CO2} > 0$, and $\Gamma^0_{\text{ion}} < 0$. In a process of increasing the concentration of salt in brine, while maintaining the temperature and pressure, the chemical potential of the ions increases, and hence the term $\Gamma^0_{\text{ion}}\, d\mu_{\text{ion}} < 0$. However the solubility of CO_2 decreases as a salting out effect occurred, also resulting in a contribution $\Gamma^0_{CO2}\, d\mu_{CO2} < 0$. From Eq. (4.4), it can be concluded that the interfacial tension of the brine and CO_2 system increases with increasing salt concentration.

4.2.4 Solubility

Molecular dynamics simulations also predict the solubility of CO_2 in brine and the mole fraction of water vapour in CO_2. The solubility of CO_2 in brine free of salt at 373 K and 2 MPa from our MD simulation is 0.0018 ±

0.0005, in good agreement with the reference value of 0.0021 from Duan's model [191]. The mole fraction of water vapour under the same condition from our MD simulation is 0.008 ±0.001, while the reference value from SAFT calculations is 0.06±0.005 [171] . See Figure 54 and Figure 55.

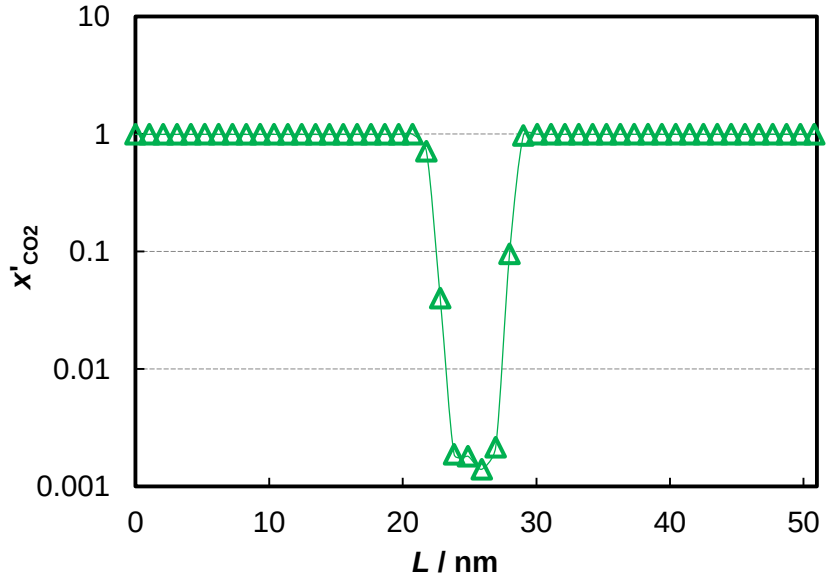

Figure 54. Solubility of CO_2 in brine free of salt expressed as mole fraction x' of CO_2 in salt-free water
NaCl(aq) and CO_2 system at T = 373 K, p = 2 MPa. Particle numbers: Ca^{2+}: 128; Cl^-: 256; Water SPC/E: 4096; CO_2 EPM2: 512

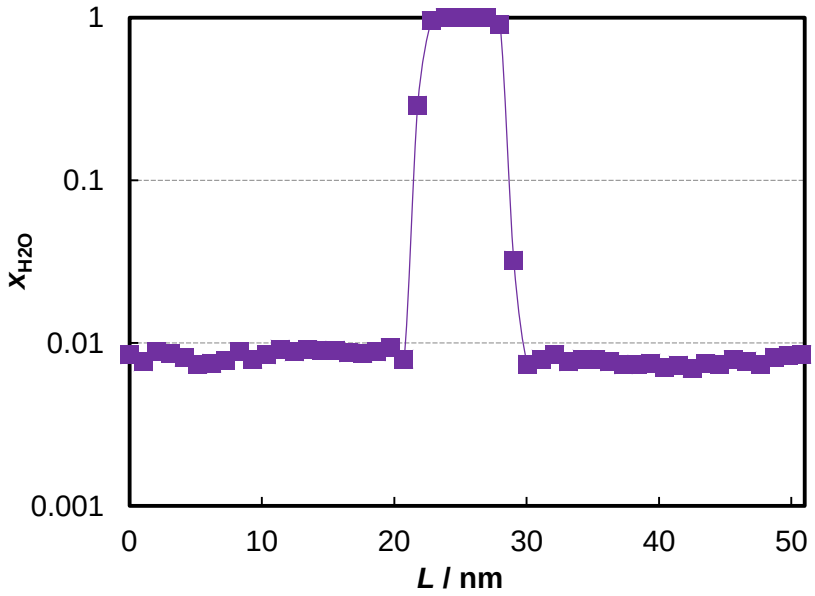

Figure 55. Solubility of water in CO_2 expressed as molar fraction of water in the CO_2 rich phase
NaCl(aq) and CO_2 system at T = 373 K, p = 2 MPa. Particle numbers: Ca^{2+}: 128; Cl^-: 256; Water SPC/E: 4096; CO_2 EPM2: 512

Chapter 5. Experimental comparison between contact angle and wettability index on reservoir fluids and rocks

In this chapter, the investigation on salinity effect on wettability in a ternary system with carbonate rock in contact with brine and crude oil is discussed. Brines of NaCl(aq) and Na_2SO_4(aq) with molality from (0.05 to 4.40) mol·kg^{-1} were studied with five different crude oils. The wettability was examined by both the NMR technique and the traditional USBM wettability index test on outcrop porous carbonate. The results from these two approaches were compared with direct contact angle measurement on an ideal mineral surface. The measurements for the comparison were made at 323.15 K and ambient pressure. The results indicated that reducing the salinity always drives carbonate minerals in the water wetting direction. This effect was found stronger for divalent ions (Na_2SO_4) than monovalent ions (NaCl) when both have identical ionic strength. Together with the interfacial tensions of brines and crude oils measured in this research, it could be further concluded that for the same type of salt, high concentration brines always have lower adhesion tension, which is independent of the types of crude oil. The relationship built between contact angle and NMR or Amott wettability index provides an effective tool on wettablity identification of reservoir rocks. Two crude oil samples and NaCl(aq) with molarility of 0.07 mol·kg^{-1} were studied under reservoir conditions. It was found that ambient condition contact angles are different from those measured under reservoir conditions. Temperature was found to have a larger influence than pressure. The contact angle measurement with the presence of CO_2 indicated that CO_2 has a large influence on the wetting condition in a system. The systems studied in this work are listed below in Table 8.

Table 8. System of calcite, crude oil, and brine studied in this work

<table>
<tr><th colspan="3">System</th><th rowspan="2">T
K</th><th rowspan="2">P
MPa</th><th rowspan="2">CA
(A.R)</th><th rowspan="2">IFT</th><th rowspan="2">USBM</th><th rowspan="2">NMR</th></tr>
<tr><th>Mineral</th><th>Brine, CO_2</th><th>Crude</th></tr>
<tr><td rowspan="6">Fresh Calcite</td><td>4.39 mol·kg^{-1} NaCl
0.07 mol·kg^{-1} NaCl</td><td rowspan="2">Crude sample 1
Crude sample 2
Crude sample 3
Crude sample 4
Crude sample 5
Decane</td><td rowspan="2">323</td><td rowspan="2">0.1</td><td rowspan="2">√(A.R)</td><td rowspan="2">√</td><td>√</td><td>√</td></tr>
<tr><td>1.66 mol·kg^{-1} Na_2SO_4
0.05 mol·kg^{-1} Na_2SO_4</td><td colspan="2"></td></tr>
<tr><td>0.07 mol·kg^{-1} NaCl</td><td>Crude sample 1</td><td rowspan="4">323
to
473</td><td rowspan="4">10
to
40</td><td rowspan="4">√</td><td rowspan="4"></td><td colspan="2" rowspan="4"></td></tr>
<tr><td>CO_2</td><td>Crude sample 2</td></tr>
<tr><td rowspan="3">0.07 mol·kg^{-1} NaCl
+
CO_2</td><td>Crude sample 1</td></tr>
<tr><td rowspan="2">Crude sample 3</td></tr>
<tr><td>Brine Aged</td></tr>
<tr><td>Oil aged</td></tr>
</table>

√: study has been carried out.

5.1 Materials

Pure deionised and degassed water (electrical resistivity > 18 MΩ·cm) was used. Sodium chloride and sodium sulphate were purchased from Sigma-Aldrich, with mass fraction purities of ≥ 0.99. Solutions were prepared gravimetrically with the relative uncertainties in mass being below 0.01 %. Thus the relative uncertainty of molality was most probably limited only by the purity of the salts and was taken to be approximately 0.5 %. The solutes were fully dissolved in the water, and then centrifuged prior to use.

The carbonate rocks are samples from outcrop Estialliades limestone, after CT scanning, porously homogeneous samples were selected for the experiment. The average pore size was around 100 μm in diameter. Single crystal calcite sample, Iceland spar, for contact angle experiment was purchase from commercial suppliers. The measuring surface was cleaved from big crystal blocks (around 4 cm on each dimension, to 4 cm in length, 2 cm in width and 5 mm in thickness), and selected under magnifying glass. Photos of these samples are shown in Figure 56.

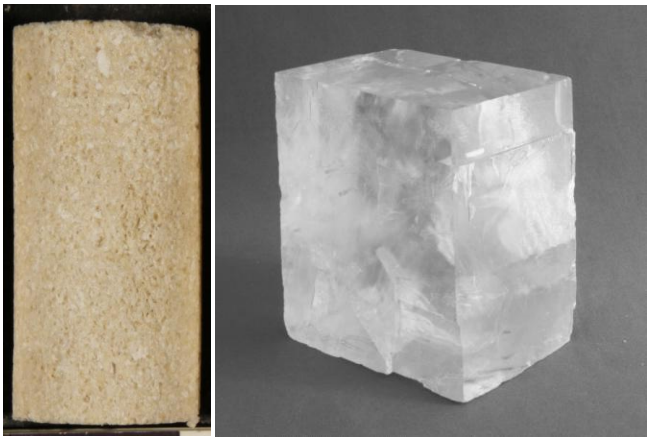

(a) (b)

Figure 56. Rock sample for wettability index measurement and contact angle measurement
(a), Estialliades limestone; (b), Iceland spar

Decane and five crude oils are use in this study. The properties of these crude oil samples are shown in Table 9.

Table 9. Properties of crude oil samples

Crude	ρ ($kg \cdot m^{-3}$)	μ (mPa·s)	SARA analysis			
			S	A	NSO	A
Sample 1	0.8779	24.81	34.77	48.87	12.45	3.90
Sample 2	0.8776	6.55	46.48	35.33	17.43	0.76
Sample 3	0.8628	9.34	31.57	50.69	14.29	3.46
Sample 4	0.8313	4.64	52.08	39.06	7.96	0.91
Sample 5	0.8112	2.34				0.15

5.2 Experimental setup

5.2.1 Experimental setup for contact angle and IFT measurement on crude oil, brine and calcite systems

Ambient pressure contact angle and IFT measurement was done on a tension meter (model DSA100S, KRÜSS GmbH), see Figure 57. This DSA100S is custom-made for contact angles, interfacial tension and surface free energies on different fluid and solids with good accuracy [192]. The experiment which operated at $T = 323$ K in this research is maintained a thermostatable environmental chamber and a heating looping surrounding the injection capillary. More detail technical information of this device is attached in Appendix H.

Figure 57. Instrument for interfacial tension and contact angle measurement [192]

The High Pressure View Chamber (HP3220LLH) is designed to operate in combination with above DSA100 system to measure surface tension (pendant drop and rising bubble) and contact angles in the parameter range from vacuum to 50 MPa and 453 K), see Figure 58. The major parts of this device are two manual high pressure screw-piston pumps and one high pressure view cell. Which are mainly the same as another apparatus introduced in section 3.2, as shown in Figure 59. More detail technical information of this device is attached in Appendix I.

Figure 58. Instrument for HPHT interfacial tension and contact angle measurement [192]

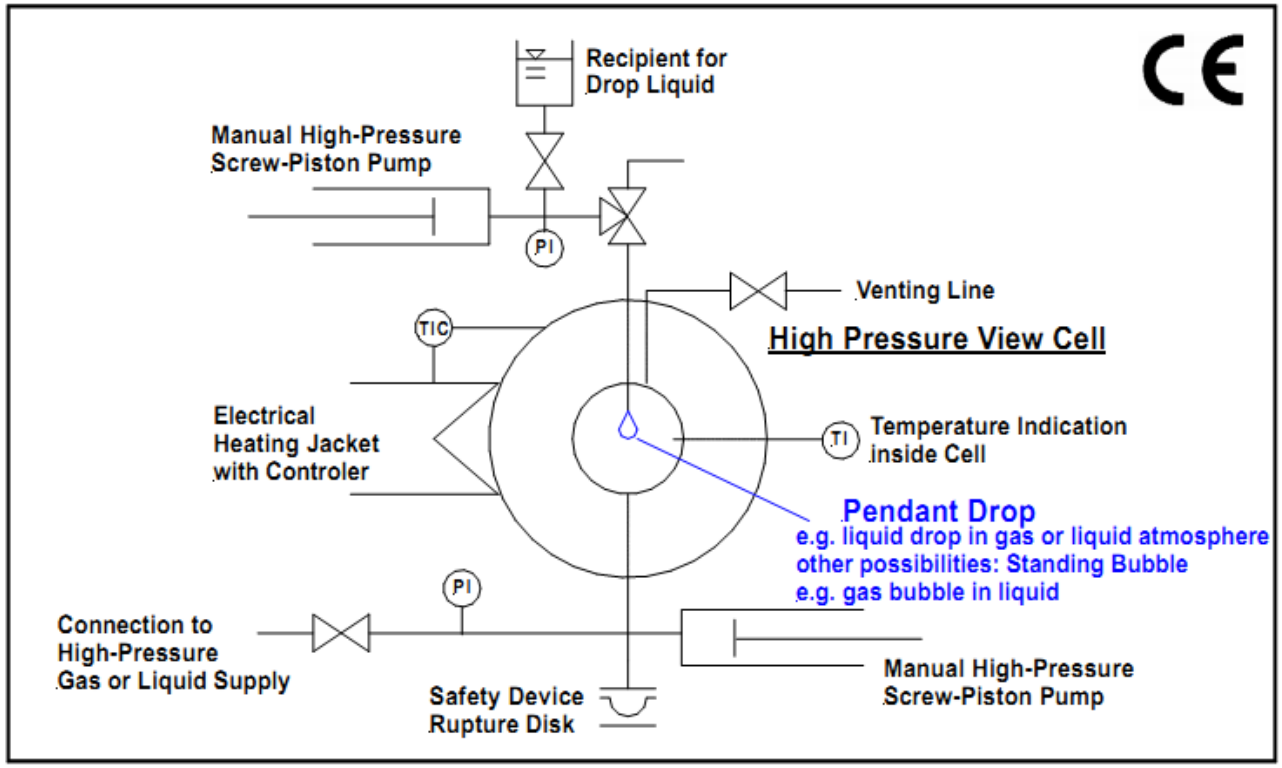

Figure 59. Schematic diagram of the apparatus [192]

5.2.2 Wettability index equipment

The equipment involved in USBM wettability index measurement is temperature controllable oven, glasses saturation jars and capillary pressure ultra rock centrifuge.

The equipment for NMR wettability index measurement is the same as the one described in Looyestijn's paper [142]. This device is capable of measuring wettability up to 323 K at ambient pressure.

5.3 Experimental procedure

5.3.1 Experimental procedure for contact angle and IFT measurement

Before the experiment, crude oil samples, brines and calcite are preheated in the oven at 323 K. In order to take the measurement at 323 K, the temperatures of both the bulk phase liquid and the injected fluid need to be maintained at 323 K. A chiller bath and heater circulator was used to pump working fluid to the heating jacket surrounding the syringe and the thermo chamber. The temperature of the working fluid was adjusted until the temperature in the thermo chamber and syringe stabilized at 323 K.

In IFT experiment, due to the fact that crude oils are less dense than brine, a bottom to top crude oil pendant drop was created during the measurement, as shown in Figure 60. For every system at least 5 droplets were measured, and for each drop a 10 minutes, which start immediately after creating them, dynamic interfacial tension was recorded.

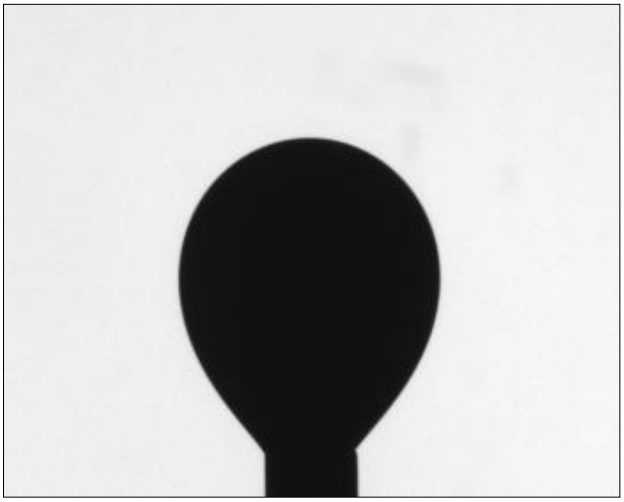

Figure 60. Crude oil sample 2 droplet in NaCl solution m = 0.07 mol·kg^{-1}, at T = 323 K, ambient pressure

The contact angle measurement was performed in a small cubic quartz container, with two pieces of calcite supporting another calcite sample. Brine was injected in to the container first and crude oil droplet is created on the underneath surface of the mineral sample by a stainless needle, as shown in Figure 61. By convention, the contact angle is measured in the water phase.

Advancing and receding contact angle was measured with 15 degrees tilting of the baseline surface of calcite.

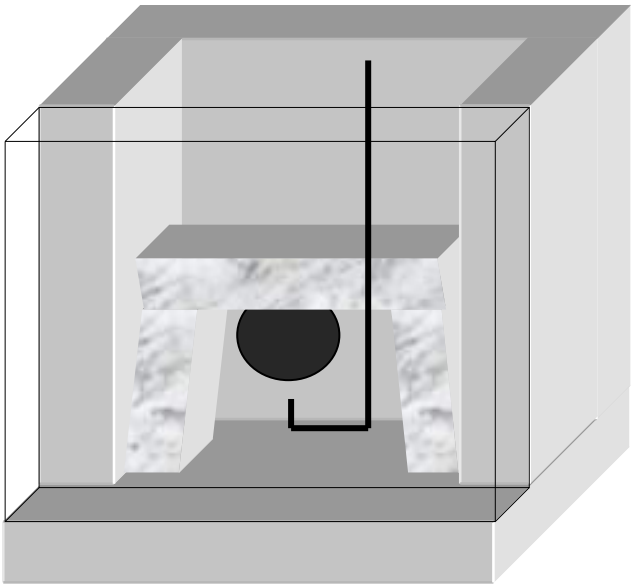

Figure 61. Schematic representation of crude oil sessile drop in touch with solid surface in brine bulk phase

5.3.2 Wettability index measurements procedure

USBM wettability index measurement in this study followed the industry standard of USBM WI procedure [141]. All the processes were performed at 323 K.

The procedure of NMR wettability index determination is the same as Looyestijn *et al*. has described in their paper [142].

5.4 Results and discussion

Brines of NaCl(aq) and Na_2SO_4(aq) with molality from (0.05 to 4.40) $mol \cdot kg^{-1}$ was studied with five different crude oils. The wettability was examined by nuclear magnetic renascence (NMR) technique, traditional USBM wettability index test on outcrop porous carbonate. The results from these two approaches were compared with direct contact angle measurement on ideal mineral surface. All the measurements were made at 323.15 K and ambient pressure. The results indicated that reducing

the salinity always drives carbonate mineral to water wetting direction. This effect was found stronger with divalent ions (Na_2SO_4), than with monovalent ions (NaCl) when both has identical ionic strength. Together with the interfacial tensions of brines and crude oils measured in this research, it could be further concluded that for the same type of salt, high concentration brine always have lower adhesion tension, independent from the type of crude oils. Finally, the relationship built between contact angle and NMR or Amott wettability index provides an effective tool on wettablity identification of reservoir rocks. Long term contact angle were measured on one crude oil and brine sample. HTHP contact angle was studied by 0.07 mol·kg^{-1} NaCl solution and two crude oil samples on calcite. The effects of CO_2 on wettabilty were investigated with CO_2 saturated 0.07 mol·kg^{-1} NaCl solution and crude oil sample 1 and 3. The study on CO_2, crude oil and calcite system found that crude oil was dissolved by CO_2 thus couldn't identify the wettability.

5.4.1 Contact angle dependence on time

Long term contact angle measurement was done with crude oil sample 2 and 0.07 mol·kg^{-1} NaCl(aq) for 100 hours. See as Figure 62. Contact angel decreases rapidly in the first 10 minutes, an initially water wetting behaviour changed to oil wetting behaviour. But after 30 minutes, the contact angle remained almost constant, see Figure 63.

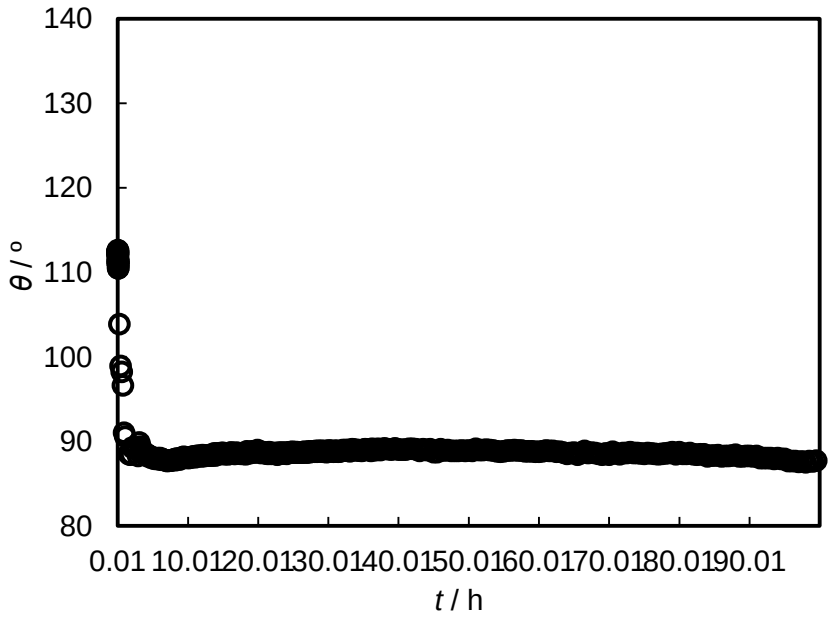

Figure 62. Long term contact angle measurement crude oil sample 2 and 0.07 mol·kg^{-1} NaCl(aq)

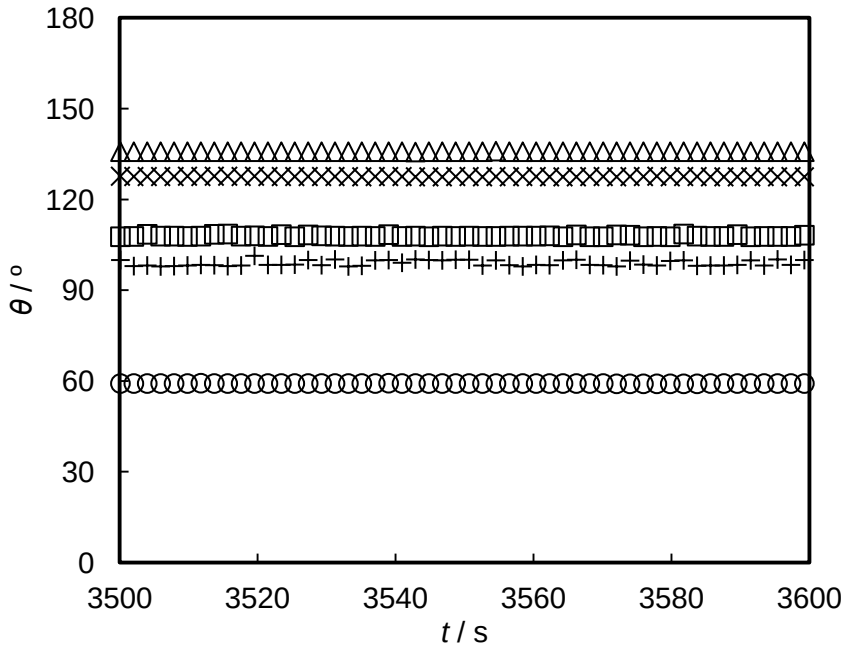

Figure 63. Contact angle dependence on time 4.39 mol·kg^{-1} NaCl(aq) at ambient pressure and T = 323 K: O, crude oil sample 1; +,crude oil sample 2; △, crude oil sample 3; □, crude oil sample 4; ×, crude oil sample 5

5.4.2 Contact angle dependence on the salinity of brine and the properties of crude oil

Different effect factors on the wettability was investigated by Gomari and Hamouda (2006) [193] on Calcite (Island-spar) from India. However they claimed that the presence of SO_4^{2-} increases the water-wetness of calcite, which is different from our experiment observation. The presence of Mg^{2+} and SO_4^{2-} ions is shown to increase the water-wetness of the calcite. Both ions reduce the contact angle. Higher reduction is obtained in presence of SO_4^{2-} compared to Mg^{2+}. An experimental study on a chalk surface, reported in a paper by Zhang *et al*. (2007) [194], which investigated three type of ions, Ca^{2+}, Mg^{2+} and SO_4^{2-} and the chalk surface concluded that to improve water wetness, SO_4^{2-} must act together with either Ca^{2+} or Mg^{2+}. The field experience on chalk reservoir, reported by Austad *et al*. (2008) [195] confirmed that the seawater improves the water wetness of chalk, which increases the oil recovery by spontaneous imbibition and viscous displacement. Just on the opposite, another research done by Chukwudeme and Hamouda (2009) [196] on chalk found that the presence of SO_4^{2-} in distilled water is shown to be more effective than that for distilled water in imbibition experiments at temperatures up to 323 K, but a large reduction in the potential oil recovery is observed when distilled water contains Mg^{2+} is used as an imbibing fluid for cores treated with asphaltene.

Our ambient condition contact angle results indicate a highly wettability dependence on both crude oil and brine types. However, for every crude oil, more concentrated brines, both NaCl(aq) and Na_2SO_4(aq) show stronger oil wetting behaviour. See Table 10.

Table 10. Contact angle dependence on the salinity of brine and the type of crude oil

Brine		Crude oil				
Ions	*m*/(mol·kg^{-1})	Sample 1	Sample 4	Sample 5	Sample 3	Sample 2
NaCl	0.07	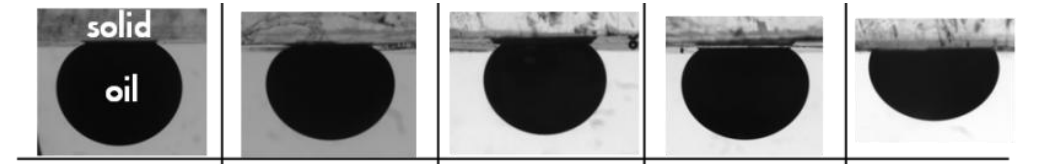				
	4.39	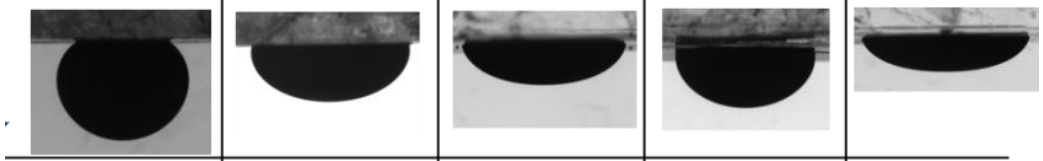				
Na_2SO_4	0.05	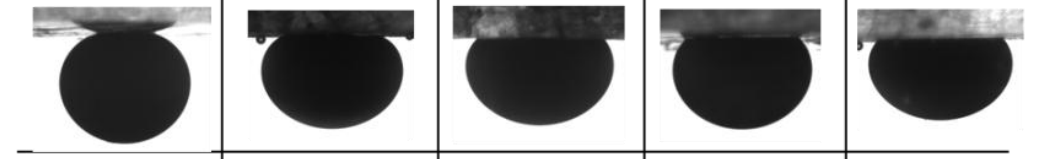				
	1.66	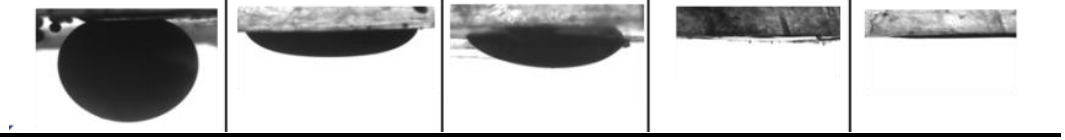				

Obviously, the salinity effect from Na_2SO_4 is stronger than NaCl for every crude oil sample.

The dependence of contact angle on crude oil is more complicated due to the fact that crude oil contains thousands of components. Nevertheless, the viscosity of crude oil plays an important role. From Figure 64 it can be seen that salinity has less effect when the viscosity of crude oil increases. Generally, for high salinity crude oils samples, $90°{\sim}\theta_{HS} < \theta_{LS}$; for low salinity crude oil samples, $\theta_{HS} < 90° < \theta_{LS}$.

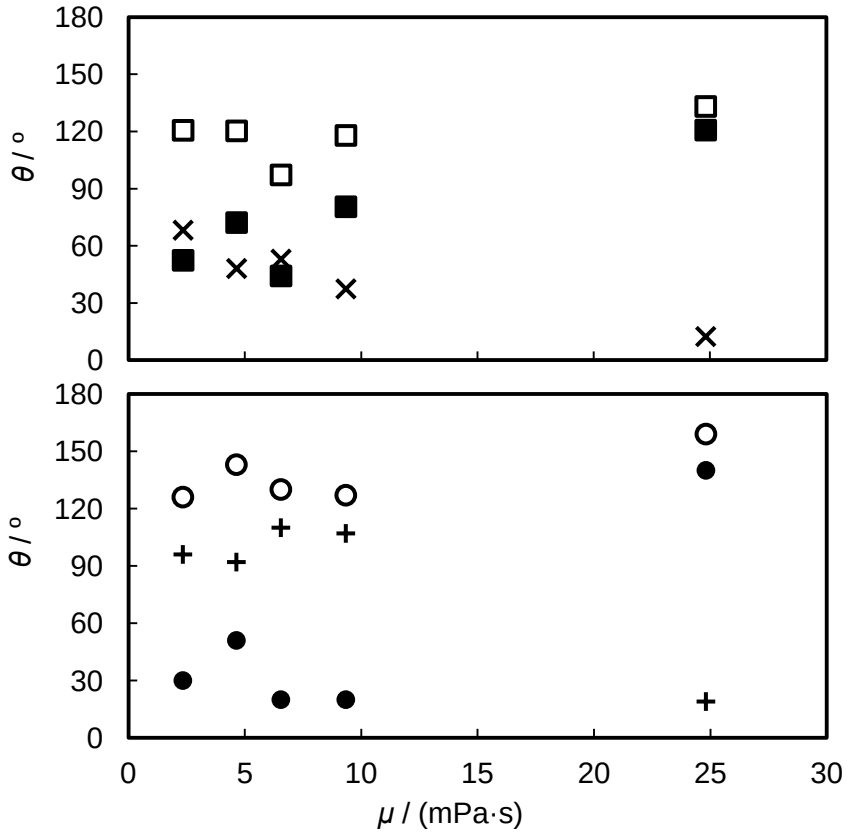

Figure 64. Contact angel dependence on crude oil viscosity
symbols: □, 0.07 mol·kg^{-1} NaCl solution; ■, 4.39 mol·kg^{-1} NaCl solution; ○, 0.55 mol·kg^{-1} Na_2SO_4 solution; ●, 1.66 mol·kg^{-1} Na_2SO_4 solution; ×, difference of two NaCl solution ; +, difference of two Na_2SO_4 solution

All the advancing and receding contact angles have around 5 to 15 degree difference from each other and they don't indicate essentially different wetting behaviour. See Figure 65 and Table 11.

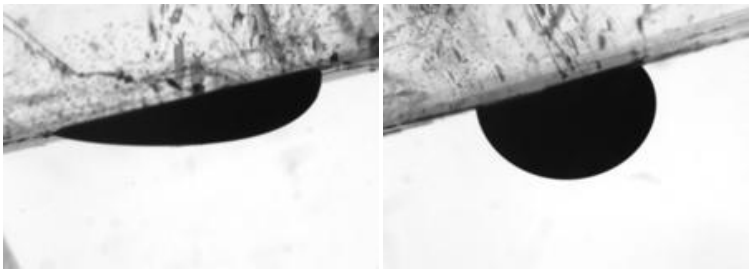

(a) (b)

Figure 65. Advancing and receding contact angle brine, crude oil sample 2 and calcite system at ambient pressure, T = 323 K: (a), 4.39 mol·kg^{-1} NaCl(aq); (b), 0.07 mol·kg^{-1} NaCl(aq)

Table 11. Contact angle θ for Crude oil and brine at 323 K, ambient pressure

Brine		Crude oil	θ / °	Advancing θ / °	Receding θ / °
Ions	m mol·kg^{-1}				
NaCl	4.39	Sample 1	59	58	60
		Sample 2	136	94	158
		Sample 3	100	81	109
		Sample 4	108	69	118
		Sample 5	128	100	134
	0.07	Sample 1	47	34	42
		Sample 2	83	64	88
		Sample 3	62	55	68
		Sample 4	60	57	66
		Sample 5	59	59	62
Na_2SO_4	1.66	Sample 1	40	39	41
		Sample 2	160	-	-
		Sample 3	160	-	-
		Sample 4	129	-	-
		Sample 5	150	-	-
	0.05	Sample 1	21	-	-
		Sample 2	50	49	83
		Sample 3	53	52	68
		Sample 4	37	-	-
		Sample 5	54	50	67

5.4.3 Contact angle dependence on temperature and pressure

Contact angle measurement of brine, crude oil and calcite system at reservoir conditions are different from the measurement at ambient conditions. Figure 66 indicates this large difference.

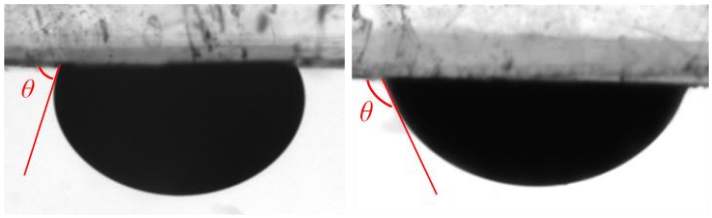

(a) (b)

Figure 66. Contact angle of crude oil sample 3 in contact with calcite 0.07 mol·kg^{-1} NaCl(aq). (a) T = 323 K, ambient pressure; (b), T = 423 K, p = 30 MPa

Contact angle of 0.07 mol·kg^{-1} NaCl(aq), crude oil sample 3 and Calcite are measured from 323 K to 473 K with pressures up to 40 MPa, these data are listed in Table 12. Figure 67 indicated that the contact angle under ambient conditions is different from reservoir conditions. When pressure was kept constant, contact angle increases with increasing temperature. However, at higher temperature conditions, contact angle doesn't have obvious change with changing pressures. At the lowest temperature in this experiment, which is 323 K, it can be seen that the contact angle increased readily with increasing pressure, but no obvious change was found when the temperature is greater than 373 K. It should be noticed that the uncertainties of the state points at ambient pressure has lower uncertainties, such even take the uncertainties into account, the trends in figure 67 shouldn't be dramatically changed.

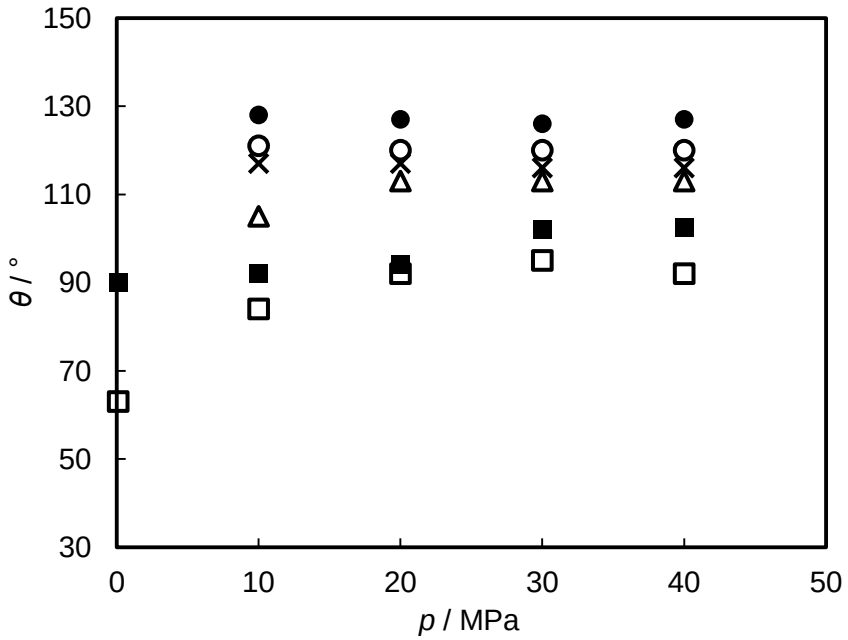

Figure 67. Contact angle dependence on temperature and pressure crude oil sample 3, 0.07 mol·kg-1 NaCl solution and calcite system. Symbols: □, T = 323 K; ■, T = 343 K; △, T = 373 K; ×, T = 393 K; ○, T = 423 K; ●, T = 473 K

Table 12. Contact angle under high temperature and high pressure conditions

Contact angle θ / °						
T/K p/MPa	323	343	373	393	423	473
0.1	63	90	-	-	-	-
10	84	92	105	117	121	128
20	92	94	113	117	120	127
30	95	102	113	116	120	126
40	92	103	113	116	120	127

5.4.4 Crude oil and brine IFT dependence on time

To obtain the IFT by the pendant drop method, the difference between the densities of the two fluids needs to be known. In this work, the densities of fluids are measured with an Anton Paar (model 4500) vibrating-tube density meter.

For all types of brine and concentrations, the IFT is observed to decrease continually in the first 200 s after a fresh pendant drop was created, but this trend gradually reached a plateau afterwards.

In Figure 68, a dynamic IFT measurement for the first 10 minutes after injecting fresh crude oil in to bulk brine phase. This behaviour is explained by the initial equilibration between crude oil and brine. This has also been noted in the literature [96, 98, 104, 165].

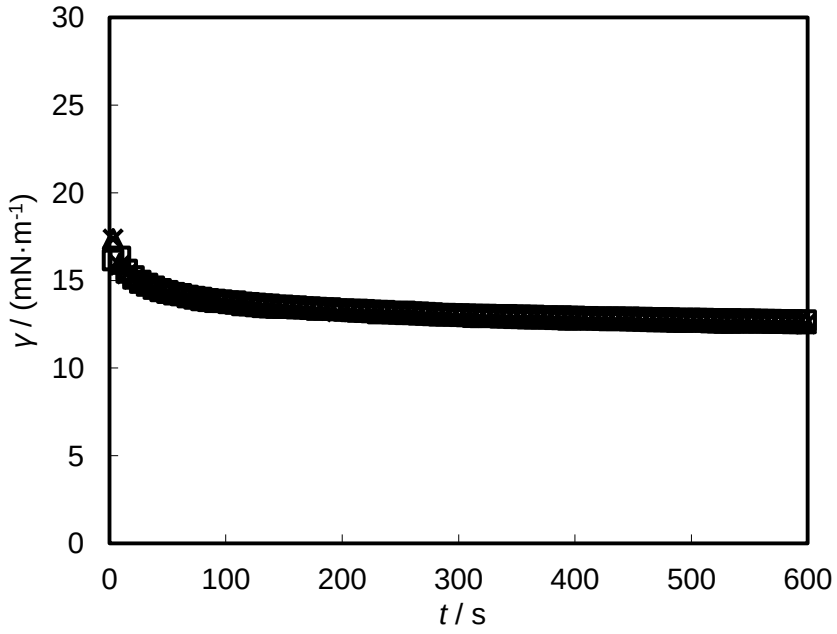

Figure 68. Time dependence interfacial tension of crude oil sample 2 and NaCl solution
m = 0.07 mol·kg^{-1}, at T = 323 K, ambient pressure
symbols: △, drop 1; ×, drop 2; □, drop 3

5.4.5 IFT dependence on the salinity of brine and the properties of crude oil

Form Figure 69 it can be seen that the IFT of NaCl solution doesn't have clear dependence on the salinity of brine. However, for Na_2SO_4, low salinity brine has higher interfacial tension on every crude oil. However

the IFT difference from high and low salinity brine is getting smaller when the viscosity increases. IFT data are listed in

Table 13.

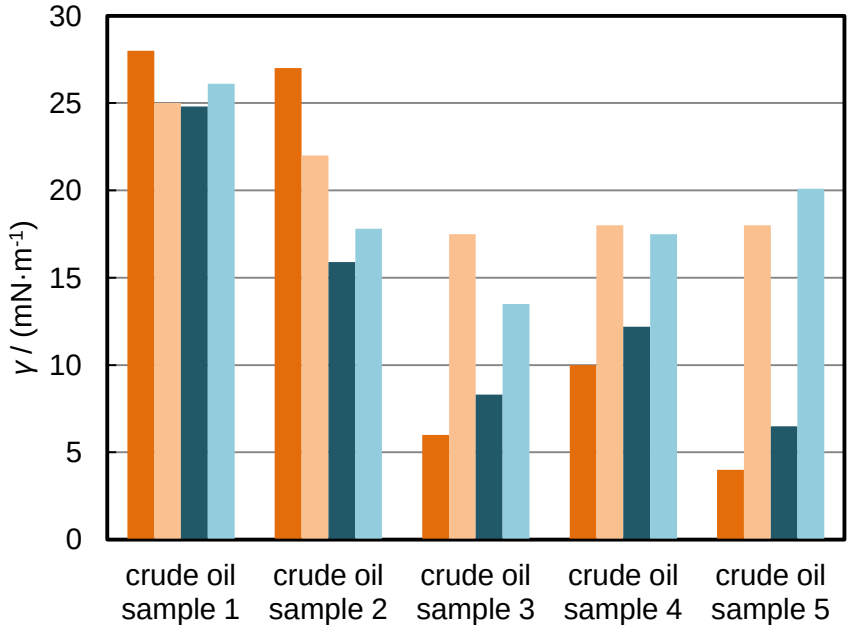

Figure 69. Interfacial tension *γ* for Crude oil and brine at 323 K, ambient pressure
symbols: ■, 4.39 mol·kg^{-1} NaCl solution; ■, 0.07 mol·kg^{-1} NaCl solution; ■, 1.66 mol·kg^{-1} Na_2SO_4 solution; ■, 0.05 mol·kg^{-1} Na_2SO_4 solution

Table 13. Interfacial tension γ for Crude oil and brine at 323 K, ambient pressure

Brine		Crude oil	$\Delta\rho$ kg·m^{-3}	γ mN·m^{-1}
Ions	*m* mol·kg^{-1}			
NaCl	4.39	Sample 1	0.27	28.2
		Sample 2	0.27	6.1
		Sample 3	0.29	27.2
		Sample 4	0.32	10.1
		Sample 5	0.34	4.1
	0.07	Sample 1	0.11	25.2
		Sample 2	0.11	17.5
		Sample 3	0.13	22.3
		Sample 4	0.16	18.1

		Sample 5	0.18	18.2
Na_2SO_4	1.66	Sample 1	0.20	24.8
		Sample 2	0.20	8.3
		Sample 3	0.21	15.9
		Sample 4	0.25	12.2
		Sample 5	0.27	6.5
	0.05	Sample 1	0.11	26.1
		Sample 2	0.11	13.5
		Sample 3	0.13	17.8
		Sample 4	0.16	17.5
		Sample 5	0.18	20.1

5.4.6 The effect of CO_2 in brine, crude oil and calcite system

The presence of CO_2 at reservoir condition changes the wettability of the system compared to the case of no CO_2 presence. Contact angle measurement on brine, crude oil and calcite system at reservoir conditions shows this change, as shown in Figure 70. It indicated that CO_2 in presence of water could effectively change the wettability in carbonate system at reservoir condition.

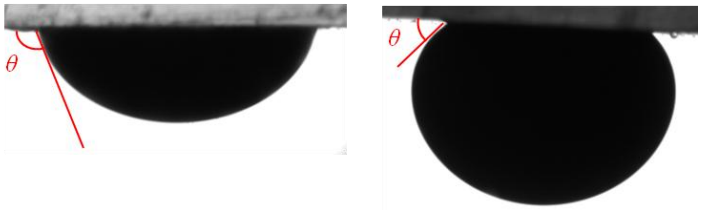

(a) (b)

Figure 70. Contact angle of crude oil sample 4 in contact with calcite T = 373 K, p = 30 MPa, (a), 0.07 mol·kg^{-1} NaCl(aq); (b), CO_2 saturated 0.07 mol·kg^{-1} NaCl(aq)

Examining the surface of calcite samples with scanning electron microscopic method, it was observed the surface layer of the mineral was dissolved in CO_2 saturated brine, while the surface underneath crude oil droplet remains the same as fresh sample, as shown in Figure 71.

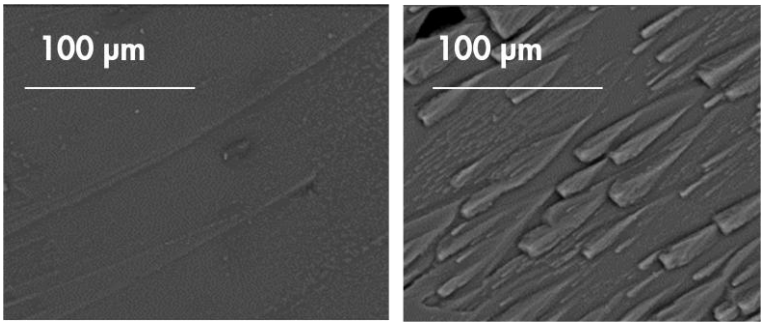

(a) (b)

Figure 71. Scanning electron microscope (SEM) image of calcite surface before experiment (a), and after experiment (b)

5.4.7 Correlation between contact angle and wettability index

Fluid rock static/dynamic interactions strongly depend on wettability and interfacial tension properties, that can vary with reservoir structure, type of fluids, temperature and pressure. The extraction of reservoir fluids injection of fluids (carbon dioxide, water, surfactants, H_2S) and trapping of fluids (Carbon dioxide) depend on wettabilitty. However empirical wettability index, such as Amott, USBM, NMR are difficult to interpret, because they usually include both wettability and pore structure information. They are not suitable for systematic investigation on the influence of wetting behaviour. Understanding the relation between contact angle and wettability index could provide an effective tool on wettablity identification, which will be applied to conventional gas and oil production, EOR, and CCS process.

The wettability indices obtain from NMR experiment are compared with contact angle results in Figure 72. It can be seen that NMR test is not quite sensitive to the porous rock sample, and large error bars were shown in the figure. This is because in theory, wettability index is an empirical fitting of the relaxation time. And the larger the pore size is, the less accurate the prediction is. Nevertheless, it still can be seen that contact angle wettability and NMR WI are correlated with each other.

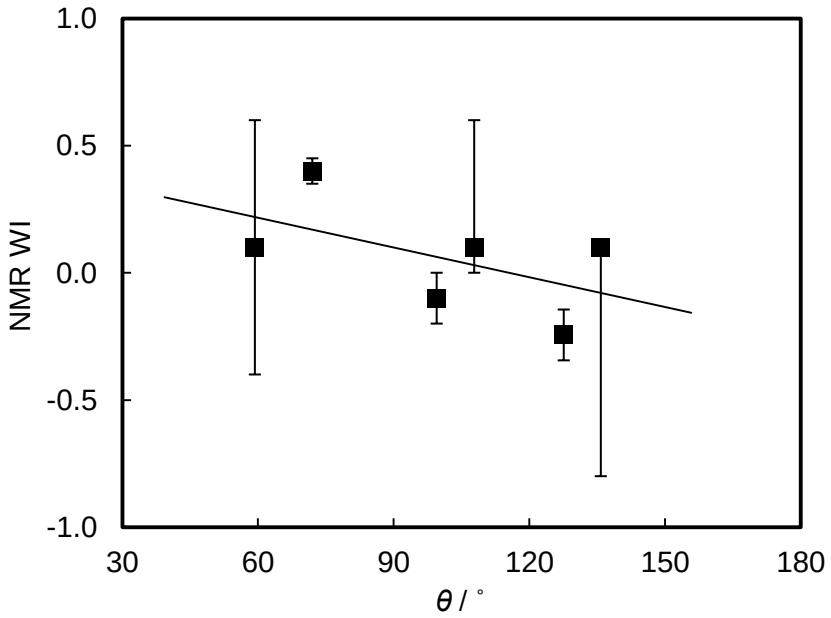

Figure 72. Comparison of NMR wettability index and contact angle
T = 373 K, ambient pressure: ■, high concentration NaCl(aq) at m = 0.07 mol·kg^{-1}

The properties of porous rock samples are listed in Table 14.

The oil production from USBM spontaneous imbibitions is showed in Figure 73. The same as contact angle results, strong dependence on brine salinity can be seen. A further oil production was also achieved from some crude oil by refresh the brine in the middle of this process.

The initial water wettability indexes obtain from Amott calculation are compared with contact angle results in Figure 74. It can be seen that contact angle wettabiliyt and Amott WI are correlated with each other.

Table 14. Rock samples for USBM wettability index measurement

	Porosity		Permeability air	Bulk density	Hg bulk volume	Grain volume	Core length	Core diameter	Vpore	Crude sample	Brine
	Hg ~ CCl3H	Cal. ~ CCl3H									
	%	%	mD	$g \cdot ml^{-1}$	ml	ml	cm	cm	ml		
1	0.27	0.28	177.5	1.97	24.38	17.78	5.07	2.49	6.60	4	HS
2	0.29	0.30	173.6	1.92	23.90	16.97	5.04	2.48	6.93	4	LS
3	0.27	0.28	152.3	1.97	24.41	17.80	5.08	2.50	6.61	2	HS
4	0.28	0.29	160.0	1.95	24.02	17.32	5.07	2.47	6.69	5	HS
5	0.28	0.29	175.0	1.94	23.94	17.22	5.07	2.48	6.72	5	LS
6	0.29	0.31	153.1	1.91	23.71	16.75	5.08	2.47	6.96	6	LS
7	0.28	0.29	152.5	1.95	23.88	17.26	5.07	2.47	6.62	6	HS
8	0.28	0.30	152.5	1.93	23.80	17.03	5.07	2.47	6.77	2	LS
9	0.28	0.29	181.2	1.93	23.85	17.07	5.08	2.46	6.79	3	HS
10	0.29	0.30	163.1	1.93	23.68	16.90	5.08	2.46	6.78	3	LS
11	0.29	0.30	189.6	1.92	23.78	16.88	5.07	2.46	6.90	1	HS
12	0.29	0.30	202.4	1.91	23.82	16.88	5.08	2.46	6.93	1	LS

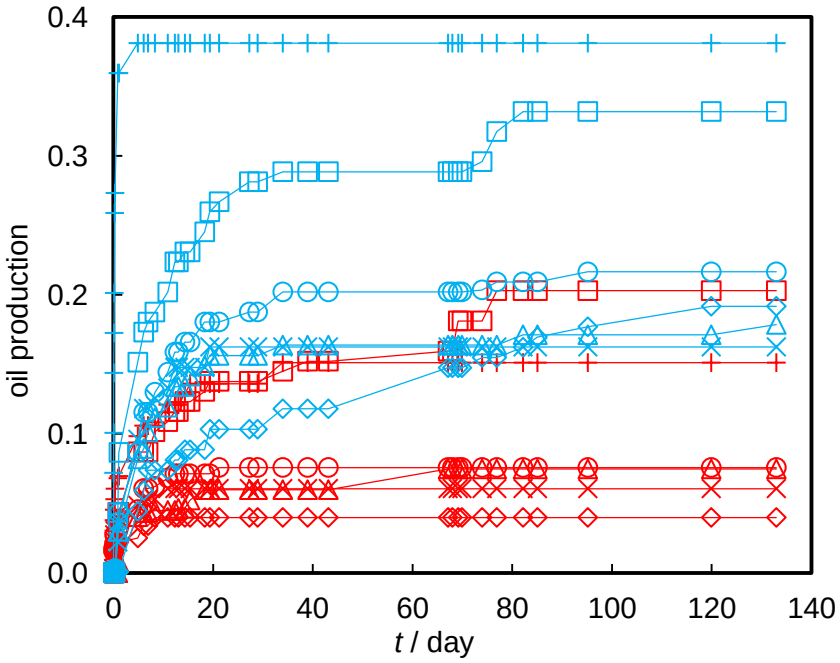

Figure 73. Oil production of 95% water saturated limestone in m = 0.07 mol·kg^{-1} NaCl(aq) at T = 373 K as a function of time.
Blue symbols, low salinity brine system; Red symbols, high salinity brine system. Symbols: □, crude oil sample 1; ×, crude oil sample 2; ◇, crude oil sample 3; O, crude oil sample 4; △, crude oil sample 5

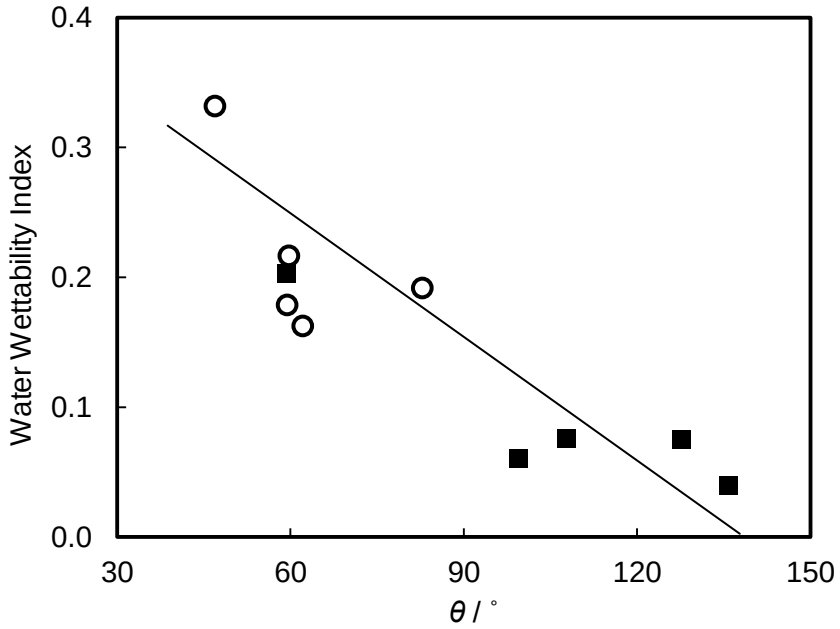

Figure 74. Comparison of Amott wettability index and contact angle T = 373 K, ambient pressure: ■, NaCl(aq) at m = 4.40 mol • kg^{-1}; ○, NaCl (aq) at m = 0.07 mol • kg^{-1}

5.4.8 IFT, contact angle and adhesion tension

Young's equation relates the contact angle to the interfacial tensions. In Figure 75, on the three phase contact line we have,

$$\gamma_{\text{rock\_brine}} - \gamma_{\text{oil\_brine}} \cdot \cos\theta = \gamma_{\text{rock\_oil}} \tag{5.1}$$

In this equation, only $\gamma_{\text{oil_brine}}$is measureable. But the interfacial tension between solid and other fluid can't be measured experimentally. Term $\gamma_{\text{oil\_brine}} \cdot \cos\theta$ is the adhesion tension of brine on calcite in oil. For the same type of oil, $\gamma_{\text{oil_rock}}$always remains the same, however, from the experimental evidence which for any kind of crude oil has been investigated in this study, the adhesion tension, $\gamma_{\text{oil\_brine}} \cdot \cos\theta$, of low salinity brine is always greater than high salinity brine, as shown in Figure 76, Contact angle together with interfacial tension at ambient

condition indicated that the higher the concentration of brine the lower the adhesion tension over different crude oils. More general, from Young-Laplace equation, it can be concluded that the IFT between rock surface and brine increases with increasing brine salinity.

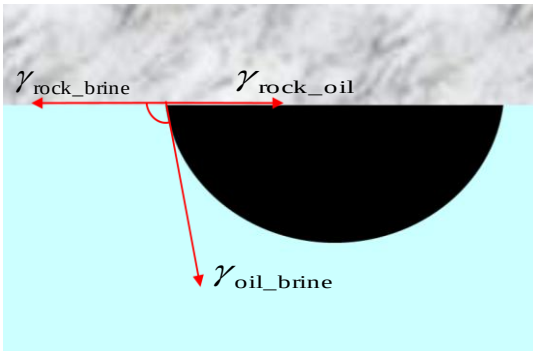

Figure 75. Contact angle for a drop on a horizontal surface

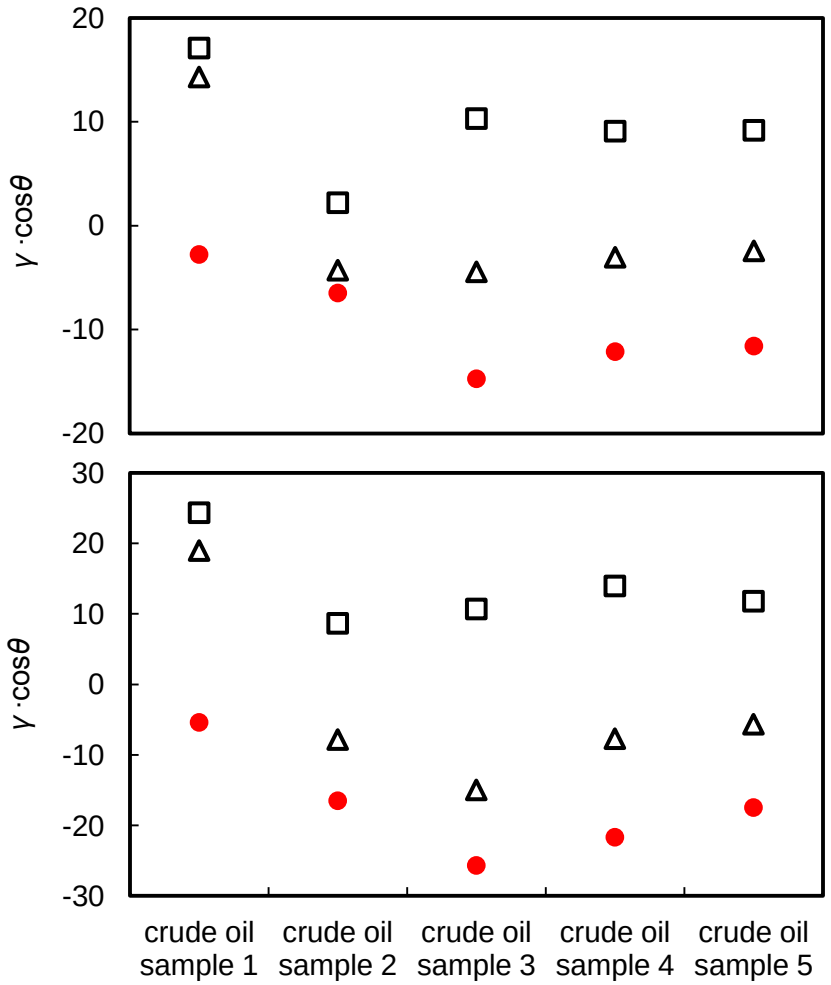

Figure 76. Adhesion tension dependence on the salinity of brine and the type of crude oil
(a), top, NaCl system; (b), bottom, Na_2SO_4 system. Symbols: □, low salinity brine; △, high salinity brine; ●, the difference

Chapter 6. Molecular Dynamics simulations of contact angle

Molecular dynamics simulations of contact angle were carried with the objective of gaining a deeper understanding of the underlying mechanism relating to brine salinity and wettability. The hypothesis from these experiment was that the low salinity effect is due to the reduction of IFT between brine and calcite when the brine salinity decreases. Experimentally, it has been found that a reduction in brine salinity enhances the wetting of calcite surfaces by the aqueous brine phase.

6.1 Contact angle simulation by molecular dynamics

Molecular Dynamics simulations of contact angle have been carried out by several authors [197-206]. Most of these investigations are related with nanomaterial wetting behaviours with water. But,, information on contact angle simulations between water/CO_2 and a calcite crystal surface are rare in the literature. However, the liquid-solid interfacial phenomena between water and calcite surfaces have been investigated [100, 207-213].

Kerisit *et al*. carried out Molecular Dynamics simulation in 2003 and 2005[208-210]. Their investigation found that water is strongly bound to the (10, 4) surface of calcite. The atom-based simulations on the calcite-water interface suggested that water lost its hydrogen-bonding network when adsorbing on the surface and that this causes an oscillation of water density in the vicinity of the surface.

Vandervoort *et al*. have reported calculated interfacial tensions between water and a calcite cleaved rhombohedron [214].

While Raiteri *et al.* developed a new force-field, based on rigid carbonate ions, which accurately describes the thermodynamics of the aqueous calcium carbonate system using molecular dynamics simulations [212].

6.2 Models for intermolecular potentials

6.2.1 Force field selection

In this research, the interactions between the typical water model (TIP4P) [181] or CO_2 (EPM2) model [150, 165, 174, 176, 182-184] and the calcite surface (10, 4) were studied. The TIP4P water model has been selected for this study since it has been shown to provide a better estimate of water vapour-liquid IFT [187]., The EPM2 model for carbon dioxide was chosen because of its good prediction of the vapor-liquid coexistence curve [183]. As discussed in chapter 4, the EPM2 CO_2 molecules were treated in the simulation by adding two dummy sites to the molecules carrying the total mass of the molecule[183], while the carbon and oxygen atoms have zero mass but carry the 6-12 Lennard-Jones parameters and the atoms are charged. The 6-12 Lennard-Jones parameters of the ions explored in this study are obtained from the OPLS-AA all-atom force field [188], as discussed in chapter 4. The parameters for calcite crystal used in this study are summarized in Table 15.

Table 15. Lennard-Jones parameters of calcite atoms

atoms	σ (nm)	ε (kJ·mol^{-1})	charge (e)	mass (g·mol^{-1})
Ions				
Ca^{2+}	0.241203	1.88136	2.000	40.0780
C	0.375000	0.43932	1.2850	12.0107
O	0.300000	0.71128	-1.0950	15.9994

6.2.2 Simulation methods

This study was performed with the GROMACS 4.4.5 MD simulation code [114] using periodical boundary conditions. For the aqueous solution and

calcite system, $CaCl_2$ with molarity of 3.46 mol·kg^{-1} was studied with calcite.

It has been shown that the (10.4) face is the dominant crystal face on the macroscopic calcite crystal. In this study, the same approach as described in a paper published by Headen and Boek [215] was used to generate the calcite system. We started from a crystal cell of 4 X 4 X 4, containing 64 $CaCO_3$ units. Then, this cell was doubled in x, y and z directions to obtain an 8 X 8 X 8 cell, containing 512 calcite molecules. Water and ions were then added to the system. Freezing atom method was applied to the calcite crystals, while no special control was applied to water/brine or CO_2 molecules.

The simulation was initialized by placing all the particles in a control box for NVT simulation. After reaching a dynamic equilibrium, a further 10 ns NVT simulation was performed, from which the final results were obtained.

During the simulation, the Nose-Hoover extended ensemble was used for temperature coupling. For this NVT simulation, the long-range coulomb intermolecular forces are treated using the cut-off assumption.

6.3 Results and discussion

In Figure 77, a snapshot of the simulation domain of the water and calcite system at 293 K and 30 MPa is presented. In the control box, 1500 TIP4P water and 512 $CaCO_3$ units are present. The system has dimensions of 3.2382×3.9917×8.0000 nm in *x, y* and *z* directions, respectively. The phase in the centre is calcite crystal and the other phase is water.

With the same simulation approach, the IFT obtained for the water and calcite system at 293 K and 100 MPa is -581 mN·m^{-1}, (-556 mN·m^{-1} from reference [216]) which is smaller than -567 mN·m^{-1} of the $CaCl_2$(aq) and

calcite system. This negative sign states that the atoms at an interface are pulled by those in the neighbouring phase which, as identified by Shuttleworth 1949 [217], results in a decrease of molecular density near the surface, which could be identified as a negative surface tension. As stated by Gibbs, “the quantity interfacial tension evidently represents the tendency to contraction in that portion of the surface of the fluid which is in contact with the solid. It may be called the superficial tension of the fluid in contact with the solid. Its value may be either positive or negative.” However, information and experimental data on this topic is lacking in the literature and should be the topic of additional research since the physical meaning of a negative interfacial tension is not completely resolved. For more information on this topic please refer to Wu and Goerge 1999 [218].

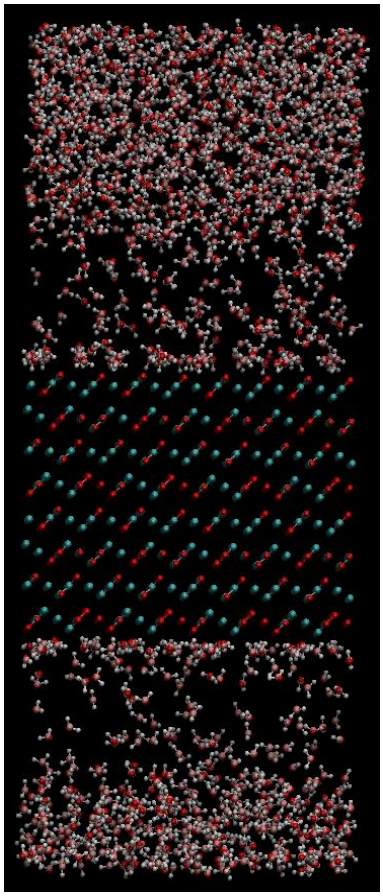

Figure 77. Snapshot of the simulation domain of a brine-calcite system equilibrated at T = 293 K, p = 100 MPa. Particle numbers: Water TIP4P: 1500; Calcite: 512

A detailed density profile of the interface is calculated from the GROMACS simulations, as shown in Figure 78. This density profile yields a 2 nm interface. An oscillation of the water density near the interface can be observed. Similar phenomena were found for $CaCl_2$(aq) and calcite systems at the same temperatures and pressures conditions.

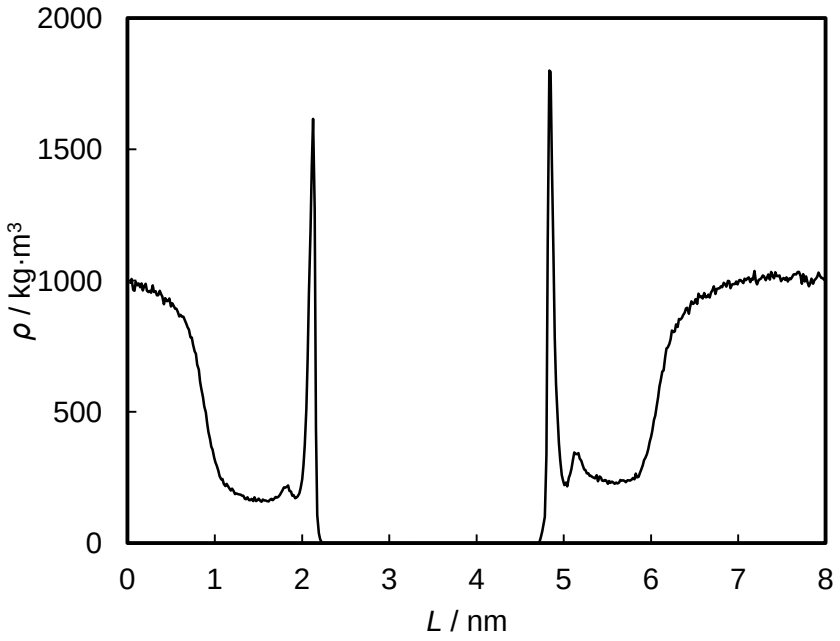

Figure 78. Snapshot of the simulation domain of a brine-calcite system equilibrated at T = 293 K, p = 30 MPa. Particle numbers: Water TIP4P: 1500; Calcite: 512

In Figure 79, a snapshot of the simulation domain of the CO_2 and calcite system at 293 K and 30 MPa is presented. In the control box, 1232 EPM2 CO_2 and 512 $CaCO_3$ units are present. The system has dimensions of 3.2382×3.9917×8.6000 nm in *x, y* and *z* directions respectively. The phase in the centre is calcite crystal and the other phase is CO_2 solution.

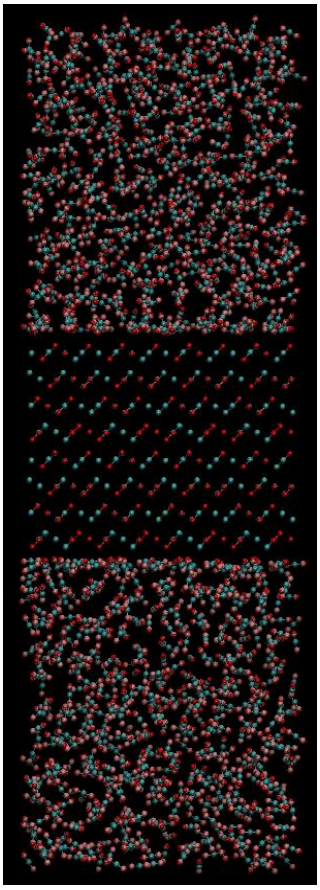

Figure 79. Snapshot of the simulation domain of a brine-calcite system equilibrated at T = 293 K, p = 30 MPa. Particle numbers: EPM2 CO_2: 1232; Calcite: 512

A detailed density profile of the interface is calculated from the GROMACS simulations, as shown in Figure 80. This density profile yields a thinner interface of only 1 nm compared to the water and calcite interface. An oscillation of the CO_2 density near the interface can be observed.

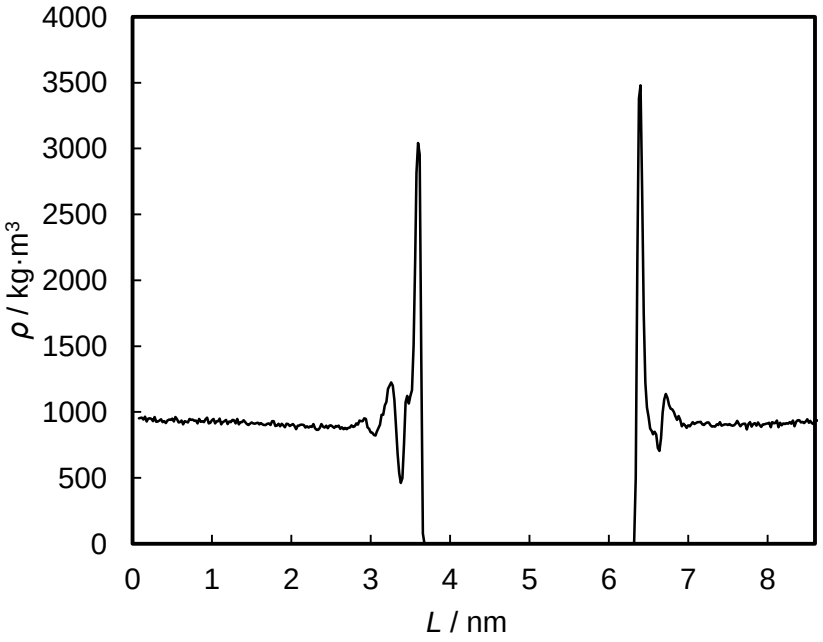

Figure 80. Snapshot of the simulation domain of a brine-calcite system equilibrated at T = 293 K, p = 30 MPa. Particle numbers: EPM2 CO_2: 1232; Calcite: 512

At 30 MPa, 293 K, the interfacial tension between water and calcite system is -271 $mN \cdot m^{-1}$, the IFT between $CaCl_2$ solution and calcite is -268 $mN \cdot m^{-1}$, while the IFT between CO_2 and calcite is -250 $mN \cdot m^{-1}$. Together with the experimental IFT between brine/water with CO_2 with the same molality, the contact angle (indicated from aqueous phase) of CO_2 and water on a calcite surface is 24.5°, while the contact angle of CO_2 and $CaCl_2$ solution on a calcite surface is 55.8°.

In this chapter, instead of directly simulating the contact angle of a three phases system, the interfacial tensions between brine or water and a calcite surface were simulated. The ions involved in this study were Ca^{2+} and Cl^-. By using this fluid-solid IFT and the fluid-fluid IFTs simulated earlier in the Young-Laplace equation, the contact angle of CO_2, brine and a calcite surface was calculated. To my knowledge, this was the first attempt to simulate the contact angle by the interfacial tensions

simulations. Together with the experimental evidence, it can be concluded that increasing the salinity of brine result in an increase of the interfacial tension between calcite and brine.

Chapter 7. Conclusions

7.1 Research Achievements

The ultimate goal of this research was to understand the interfacial phenomena between CO_2, brine/hydrocarbon, and carbonate rock. With limited time, the greater part of my Ph.D. studies focused on the experimental investigation and molecular modelling of interfacial tension between CO_2 and brine under a range of reservoir conditions. This information is of primary importance for both CO_2-EOR and CO_2 storage, which is data that is lacking in the open literature. While some research has been conducted on the contact angle of crude oil and brine on calcite surfaces significantly more information is required on the interfacial phenomena between CO_2, brine/hydrocarbon, and carbonate rock.

7.1.1 Experimental measurement of IFT

- A new apparatus for carrying out IFT measurements on corrosive fluids at high temperatures (up to 473 K) and high pressures (up to 50 MPa) was designed and constructed. Another apparatus for measuring the saturated phase reservoir fluids densities was also constructed.

Experimental measurements of interfacial tension were made on carbon dioxide systems with aqueous solutions of different salts with salt molalities between 0.98 and 4.95 $mol \cdot kg^{-1}$. Temperatures studied were between 298 and 473 K and at various pressures up to 50 MPa. The apparatus used was a pendant drop of CO_2-saturated brine surrounded by a water-saturated CO_2 phase. The expanded uncertainties at 95 % confidence are 0.05 K in temperature, 70 kPa in pressure and the larger of $0.016 \cdot \gamma$ and 0.6 $mN \cdot m^{-1}$ for interfacial tension.

- The results show that for the same type of ions, the interfacial tension increases linearly with molality of the salt solution.
- For strong electrolyte brines, IFTs were found to depend on the positive charge concentration.
- However, for the weak electrolyte, such as HCO_3^-, different behaviour was found.

Empirical models have been developed to represent the presented results as a function of temperature, pressure, and molality with an absolute average relative deviation of 2% to 6%.

7.1.2 MD simulation of IFT

Molecular Dynamic (MD) simulations were used to investigate the interfacial tension of CO_2-brine systems for a range of temperatures between 303 and 393 K and pressures from 2 to 50 MPa. The ions involved in MD study were Na^+, Ca^{2+} and Cl^-.

- Results show that interfacial tension decreases with increasing of pressure under any temperature condition, but increases linearly with the molality of the salt solutions tested.
- The density profiles calculated from the MD simulation demonstrate a positive excess of CO_2 and a negative excess of ions at the interface.
- Ionic charge is found to have a larger influence on interfacial tension than ionic size, which is consistent with experimental findings.

7.1.3 Empirical model of IFT

- We achieve a nearly complete understanding of the interfacial behaviour between CO_2 and brines by experimental measurement and MD simulations. With given temperature (293 K ≤ T ≤ 473 K), pressure (p ≤ 50 MPa) and brine salinity, we can predictthe IFT of any brine and CO_2

system by empirical models based on the experimental fact and molecular scale interfacial phenomena without further measurement.
We measured the IFTs of four different brines, NaCl(aq) and Na_2SO_4(aq) with molality from 0.05 to 4.40 mol·kg^{-1}, and five crude oils samples at ambient pressure and elevated temperature (323 K).

- The results prove that both crude oil properties and brine salinity have a strong effect on interfacial tension.

7.1.4 Experimental measurement of Contact angle

Contact angles of NaCl(aq) and Na_2SO_4(aq) with molality from 0.05 to 4.40 mol·kg^{-1}, and five crude oil samples in contact with carbonate rocks were measured at 323 K and ambient pressure.

- We came to the conclusion that a reduction of the brine salinity always leads to increased water wetting behaviour on carbonates. This effect is stronger with divalent ions (Na_2SO_4) than with monovalent ions (NaCl), when both are considered under identical ionic strength.
- Based on the interfacial tensions of brines and crude oils measured in this research, we further conclude that for the same type of salt, high concentration brines always have lower adhesion tensions, independent from the type of crude oil used.

Reservoir condition contact angle was measured with NaCl(aq) at molarity of 0.07 mol·kg^{-1} and two crude oil samples.

- The experimental results suggest that the contact angle of the same system changes with temperature and pressure. However, by increasing the temperature, the effect of pressure change on the same isotherm was found to diminish.

Contact angle measurements were carried out on CO_2 saturated NaCl(aq), with molarity of 0.07 mol·kg^{-1}, and crude oil sample 1 and 3 on a calcite surface pre-exposed to either brine or crude oil.

- We find that the presence of CO_2 reduces the contact angle (measured form the water side) at the same thermodynamic conditions.

7.1.5 Correlation between contact angle and wettability index

- A correlation between contact angle and wettability index, NMR, Amott/USBM was established by combining the wettability index measurement on the same brines with crude oils, as mentioned above but in contact with porous calcite outcrop rocks. By fully understanding therelationship, we could provide the measurement of contact angle as an effective tool for wettablity identification of reservoir rocks.
- The analysis of contact angle data combined with brine-oil interfacial tension in brine, crude oil and calcite systems further manifest that for the same type of salt, high concentration brine always has lower adhesion tension, which is independent from the type of crude oil used.

7.1.6 MD simulation of contact angle

MD simulation of contact angle was carried out for a deeper understanding of the underlying mechanism of brine salinity effect on wettability.

- Instead of directly simulating the contact angle in a three phase system, we simulated the interfacial tension between brine/water or CO_2 and calcite surface with a variation of brine salinity. This was the first attempt to simulate contact angle via IFT simulations on binary systems.
- Together with the experimental evidence, we conclude that increased brine salinity resulted in a reduction ofinterfacial tension between calcite and brine. The experimental measurement and MD simulations indicated that reducing the salinity of brine could generally reduce the adhesion tension of crude oil in brine and calcite systems. In conclusion, low salinity water flooding could potentially increase oil recovery in carbonate reservoirs.

Reviewing the literature, these results are the first attempt to explain low salinity EOR effect and they provide a better fundamental understanding of the interactions between calcite, brines, and crude oils. More generally, high salinity saline reservoirs are more favourable for CO_2 trapping.

7.2 Future Research

From the experience of interfacial tension measurement on brine and CO_2, we found that the impurities, either dissolved or present at the interface, have a large influence on interfacial tension. Our measurements were carried out with ideal CO_2 and brine solutions. However, in practical terms, pure CO_2 does not exist. Further research on CO_2 and brine interfacial tension with typical impurities, such as H_2S, SO_2, and N_2 seems to be essential.

This research proved that HCO_3^- behaves differently than Cl^- and SO_4^{2-}, ions on the IFT of brine and CO_2. Due to time limitation, MD simulations were only carried out on strong electrolytes in our research. A molecular-scale investigation on weak electrolytes would be helpful to understand the behaviour of anions on the interface. A classical MD simulation could be applied to a CO_2 and $NaHCO_3$(aq) system. Furthermore, a Quantum simulation of the same system can be conducted to investigate the temperature and pressure influence of the equilibrium below,

$$HCO_3^- = CO_3^{2-} + H^+$$

and,

$$CO_2 + H_2O = HCO_3^- + H^+$$

We have calculated the interfacial tension of CO_2 and brine/water, the density profile of brine and CO_2 interface, and predicted solubility of CO_2 in brine by applying MD simulation. There are some other thermal physical properties, such as the viscosity and the diffusion coefficient that

could be studied by molecular dynamic simulation. It is significant to completely understand these properties at molecular scale.

The current MD simulation approach could predict interfacial tension with an uncertainly less than 5%. In the academia circle, a few authors [219-221] use Particle-Particle Particle-Mesh (PPPM) method to calculate the long range molecular interaction instead of PME. The surface tension of water simulated by this algorithm coincides with the experiment results. In order to predicate accurate interfacial tensions, different algorithms should be applied and compared in the future.

The contact angles measured at ambient pressure and 323 K were different than the results for reservoir conditions. This indicates that the field conditions contact angle should be measured to predict reservoir wetting correctly. A systematic study of contact angle dependency on temperature, pressure, and brine salinity will be significant to proceed.

Contact angle measurement of brine, CO_2,and calcite system could be analyzed together with the IFT data from this research to achieve a complete understanding of the wetting behaviour and capillary pressure of the system.

The MD simulations of contact angle provide a new tool for investigating the wetting behaviour of a ternary system. Nevertheless, it will be worth going through an uncertainty estimation of the approach, which applied the assumptions for liquid-liquid IFT calculation to solid-liquid phase. Additionally, a comparison between the presented approach and results from a direct contact angle MD simulation, as mentioned in the literature, would be beneficial.

Reference

1. Countries, O.o.t.P.E., *World Oil Outlook 2010.* 2010.
2. Countries, O.o.t.P.E., *World Oil Outlook 2011.* 2011.
3. *Enhanced Oil Field Recovery Survey-Worldwide-EOR.* Oil Gas J., 2010.
4. Shedid A, S., *Influences of Fracture Orientation on Oil Recovery by Water and Polymer Flooding Processes: An Experimental Approach.* J. Pet. Sci. Eng., 2006. **50**(3-4): p. 285-292.
5. Blunt, M., F.J. Fayers, and F.M. Orr Jr, *Carbon Dioxide in Enhanced Oil Recovery.* Energy Convers. Manage., 1993. **34**(9-11): p. 1197-1204.
6. Rogers, J.D. and R.B. Grigg, *A Literature Analysis of the WAG Injectivity Abnormalities in the CO_2 Process.* SPE Reservoir Evaluation & Engineering, 2001. **4**(5): p. 375-386.
7. Parker, M.E., J.P. Meyer, and S.R. Meadows, *Carbon Dioxide Enhanced Oil Recovery Injection Operations Technologies (Poster Presentation).* Energy Procedia, 2009. **1**(1): p. 3141-3148.
8. Jessen, K., A.R. Kovscek, and F.M. Orr, *Increasing CO_2 Storage in Oil Recovery.* Energy Convers. Manage., 2005. **46**(2): p. 293-311.
9. Blom, S.M.P. and J. Hagoort, *The Combined Effect of Near-Critical Relative Permeability and non-Darcy Flow on Well Impairment by Condensate drop out.* Spe Reservoir Evaluation & Engineering, 1998. **1**(5): p. 421-429.
10. Blom, S.M.P., J. Hagoort, and D.P.N. Soetekouw, *Relative Permeability at Near-Critical Conditions.* Spe Journal, 2000. **5**(2): p. 172-181.
11. Grattoni, C.A., X.D. Jing, and R.A. Dawe, *Dimensionless Groups for three-phase Gravity Drainage Flow in Porous Media.* J. Pet. Sci. Eng., 2001. **29**(1): p. 53-65.
12. Alotaibi, M.B., R. Azmy, and H.A. Nasr-El-Din, *A Comprehensive EOR Study Using Low Salinity Water in Sandstone Reservoirs*, in *SPE Improved Oil Recovery Symposium*. 2010, Society of Petroleum Engineers: Tulsa, Oklahoma, USA.
13. Bachu, S. and B. Bennion, *Effects of in-situ Conditions on Relative Permeability Characteristics of CO_2 and Brine Systems.* Environ. Geol., 2008. **54**(8): p. 1707-1722.
14. Bennion, D.B. and S. Bachu, *The Impact of Interfacial Tension and Pore Size Distribution/Capillary Pressure Character on CO_2 Relative Permeability at Reservoir Conditions in CO_2-Brine Systems*, in *SPE/DOE Symposium on Improved Oil Recovery*. 2006: Tulsa, Oklahoma, USA.
15. Jaeger, P.T., M.B. Alotaibi, and H.A. Nasr-El-Din, *Influence of Compressed Carbon Dioxide on the Capillarity of the Gas-Crude Oil-Reservoir Water System.* J. Chem. Eng. Data, 2010. **55**(11): p. 5246-5251.

16. Karimaie, H. and O. Torsæter, *Low IFT Gas-oil Gravity Drainage in Fractured Carbonate Porous Media.* J. Pet. Sci. Eng., 2010. **70**(1-2): p. 67-73.
17. Sun, C.-Y. and G.-J. Chen, *Measurement of Interfacial Tension for the CO_2 Injected Crude Oil + Reservoir Water System.* J. Chem. Eng. Data, 2005. **50**(3): p. 936-938.
18. Yang, D.Y., P. Tontiwachwuthikul, and Y.G. Gu, *Dynamic interfacial tension method for measuring gas diffusion coefficient and interface mass transfer coefficient in a liquid.* Ind. Eng. Chem. Res., 2006. **45**(14): p. 4999-5008.
19. Yang, D., P. Tontiwachwuthikul, and Y. Gu, *Interfacial Tensions of the Crude Oil + Reservoir Brine + CO_2 Systems at Pressures up to 31 MPa and Temperatures of 27 °C and 58 °C.* Journal of Chemical and Engineering Data, 2005. **50**(4): p. 1242-1249.
20. Jarrell, P.M., et al., *Practical Aspects of CO_2 Flooding*. SPE Monograph Series, ed. R.T. Johns. Vol. 22. 2002, Dallas: Society of Petroleum Engineers.
21. Stenger, B.A., et al., *Short-Term and Long-Term Aspects of a Water Injection Strategy.* SPE Reservoir Evaluation & Engineering, 2009(12): p. pp. 841-852.
22. Webb, K.J., C.J.J. Black, and H. Al-Ajeel, *Low Salinity Oil Recovery - Log-Inject-Log*, in *SPE/DOE Symposium on Improved Oil Recovery*. 2004, Society of Petroleum Engineers: Tulsa, Oklahoma.
23. McGuire, P.L., et al., *Low Salinity Oil Recovery: An Exciting New EOR Opportunity for Alaska□s North Slope*, in *SPE Western Regional Meeting*. 2005, Society of Petroleum Engineers: Irvine, California.
24. Manrique, E.J., V.E. Muci, and M.E. Gurfinkel, *EOR Field Experiences in Carbonate Reservoirs in the United States.* SPE Reservoir Evaluation & Engineering, 2007(12): p. pp. 667-686.
25. Vledder, P., et al., *Low Salinity Water Flooding: Proof Of Wettability Alteration On A Field Wide Scale*, in *SPE Improved Oil Recovery Symposium*. 2010, Society of Petroleum Engineers: Tulsa, Oklahoma, USA.
26. Alotaibi, M.B., R.M. Azmy, and H.A. Nasr-El-Din, *Wettability Studies Using Low-Salinity Water in Sandstone Reservoirs*, in *Offshore Technology Conference*. 2010: Houston, Texas, USA.
27. Austad, T., A. Rezaeidoust, and T. Puntervold, *Chemical Mechanism of Low Salinity Water Flooding in Sandstone Reservoirs*, in *SPE Improved Oil Recovery Symposium*. 2010, Society of Petroleum Engineers: Tulsa, Oklahoma, USA.
28. Alotaibi, M.B., R.A. Nasralla, and H.A. Nasr-El-Din, *Wettability Studies Using Low-Salinity Water in Sandstone Reservoirs.* SPE Reservoir Evaluation & Engineering, 2011. **14**(6): p. 713-725.

29. Nasralla, R.A., M.B. Alotaibi, and H.A. Nasr-El-Din, *Efficiency of Oil Recovery by Low Salinity Water Flooding in Sandstone Reservoirs*, in *SPE Western North American Region Meeting*. 2011, Society of Petroleum Engineers: Anchorage, Alaska, USA.
30. Nasralla, R.A. and H.A. Nasr-El-Din, *Coreflood Study of Low Salinity Water Injection in Sandstone Reservoirs*, in *SPE/DGS Saudi Arabia Section Technical Symposium and Exhibition*. 2011, Society of Petroleum Engineers: Al-Khobar, Saudi Arabia.
31. Yousef, A.A., et al., *Laboratory Investigation of the Impact of Injection-Water Salinity and Ionic Content on Oil Recovery From Carbonate Reservoirs.* SPE Reservoir Evaluation & Engineering, 2011(10): p. pp. 578-593.
32. Aksulu, H., et al., *Evaluation of Low-Salinity Enhanced Oil Recovery Effects in Sandstone: Effects of the Temperature and pH Gradient.* Energy Fuel., 2012. **26**(6): p. 3497-3503.
33. Al-adasani, A., B. Bai, and Y.-S. Wu, *Investigating Low-Salinity Waterflooding Recovery Mechanisms in Sandstone Reservoirs*, in *SPE Improved Oil Recovery Symposium*. 2012, Society of Petroleum Engineers: Tulsa, Oklahoma, USA.
34. Cissokho, M., et al., *Low Salinity Oil Recovery on Clayey Sandstone: Experimental Study.* PetroPhysics, 2010. **51**(5): p. 305-313.
35. Skreffingland, K., et al., *Snorre Low-Salinity-Water Injection-Coreflooding Experiments and Single-Well Field Pilot.* SPE Reservoir Evaluation & Engineering, 2011. **14**(2): p. 182-192.
36. Brady, P.V. and J.L. Krumhansl, *A surface complexation model of oil-brine-sandstone interfaces at 100 degrees C: Low salinity waterflooding.* Journal of Petroleum Science and Engineering, 2012. **81**: p. 171-176.
37. Cense, A., et al., *Direct Visualization of Designer Water Flooding in Model Experiments*, in *SPE Enhanced Oil Recovery Conference*. 2011, Society of Petroleum Engineers: Kuala Lumpur, Malaysia.
38. Hassenkam, T., et al., *Pore scale observation of low salinity effects on outcrop and oil reservoir sandstone.* Colloids and Surfaces A: Physicochemical and Engineering Aspects, 2011. **390**(1–3): p. 179-188.
39. Rezaeidoust, A., T. Puntervold, and T. Austad, *A Discussion of the Low Salinity EOR Potential for a North Sea Sandstone Field*, in *SPE Annual Technical Conference and Exhibition*. 2010, Society of Petroleum Engineers: Florence, Italy.
40. Fogden, A., *Removal of crude oil from kaolinite by water flushing at varying salinity and pH.* Colloids and Surfaces a-Physicochemical and Engineering Aspects, 2012. **402**: p. 13-23.
41. Hartland, S., Hartley, Richard W., *Axisymmetric Fluid-Liquid Interfaces: Tables Giving the Shape of Sessile and Pendant Drops and External Menisci, with Examples of their use.* Elsevier, Amsterdam, 1976.

42. Tweheyo, M.T., T. Holt, and O. Torsæter, *An Experimental Study of the Relationship between Wettability and Oil Production Characteristics.* J. Pet. Sci. Eng., 1999. **24**(2–4): p. 179-188.
43. Alotaibi, M.B., H.A. Nasr-El-Din, and J.J. Fletcher, *Electrokinetics of Limestone and Dolomite Rock Particles.* SPE Reservoir Evaluation & Engineering, 2011(10): p. pp. 594-603.
44. Idowu, J., et al., *Effect of Salinity Changes of the Injected Water on Water Flooding Performance in Carbonate Reservoirs*, in *Nigeria Annual International Conference and Exhibition*. 2011, Society of Petroleum Engineers: Abuja, Nigeria.
45. Zahid, A., A.A. Shapiro, and A. Skauge, *Experimental Studies of Low Salinity Water Flooding Carbonate: A New Promising Approach*, in *SPE EOR Conference at Oil and Gas West Asia*. 2012, Society of Petroleum Engineers: Muscat, Oman.
46. Core Writing Team, P., R.K. and Reisinger, A. (Eds.), *Contribution of Working Groups I, II and III to the Fourth Assessment Report of the Intergovernmental Panel on Climate Change.* IPCC Fourth Assessment Report 2007: p. pp 104.
47. Bachu, S., W.D. Gunter, and E.H. Perkins, *Aquifer Disposal of CO_2: Hydrodynamic and Mineral Trapping.* Energy Convers. Manage., 1994. **35**(4): p. 269-279.
48. Gunter, W.D., E.H. Perkins, and T.J. McCann, *Aquifer disposal of CO_2-rich gases: Reaction design for added capacity.* Energy Convers. Manage., 1993. **34**(9–11): p. 941-948.
49. Butt, H.-J., K. Graf, and M. Kappl, *Introduction*. Physics and Chemistry of Interfaces. 2004: Wiley-VCH Verlag GmbH & Co. KGaA. 1-3.
50. Chang, J., et al., *Structure and Properties of Polymethylene Melt Surfaces from Molecular Dynamics Simulations.* J. Chem. Phys., 2001. **115**(6): p. 2831-2840.
51. Rowlinson, J.S. and B. Widom, *Molecular Theory of Capillarity*. 2002: Dover Publ.
52. Rowlinson, J.S., *Molecular theory of capillarity*. 2002.
53. Young, T., *An Essay on the Cohesion of Fluids.* Philosophical Transactions of the Royal Society of London, 1805. **95**(ArticleType: research-article / Full publication date: 1805 /): p. 65-87.
54. Brooks, R.H. and A.T. Corey, *Hydraulic Properties of Porous Media*. 1964: Colorado State University.
55. Cheng, P., et al., *Automation of axisymmetric drop shape analysis for measurements of interfacial tensions and contact angles.* Colloids and Surfaces, 1990. **43**(2): p. 151-167.
56. Susnar, S.S., et al., *Pressure-Dependence of the Density of Normal-Alkanes.* Int J Thermophys, 1992. **13**(3): p. 443-452.

57. Lyklema, J., et al., *Liquid-Fluid Interfaces*. Chemical, Petrochemical & Process. 2000: Academic Press. 1-751.
58. Fainerman, V.B. and R. Miller, *The Maximum Bubble Pressure Tensiometry*, in *Studies in Interface Science*, D. MÖbius and R. Miller, Editors. 1998, Elsevier. p. 279-326.
59. Liggieri, L. and F. Ravera, *Capillary pressure tensiometry and applications in microgravity*, in *Studies in Interface Science*, D. MÖbius and R. Miller, Editors. 1998, Elsevier. p. 239-278.
60. Nguyen, A.V. and H. Stechemesser, *Dynamics of the impact interaction between a fine solid sphere and a plane Gas-Liquid interface*, in *Studies in Interface Science*, D. MÖbius and R. Miller, Editors. 1998, Elsevier. p. 525-562.
61. MÖbius, D. and R. Miller, *Subject Index*, in *Studies in Interface Science*. 1998, Elsevier. p. 707-715.
62. Seifert, A.M., *Spinning Drop Tensiometry*, in *Studies in Interface Science*, D. MÖbius and R. Miller, Editors. 1998, Elsevier. p. 187-238.
63. Da Rocha, S.R.P., K.L. Harrison, and K.P. Johnston, *Effect of Surfactants on the Interfacial Tension and Emulsion Formation between Water and Carbon Dioxide.* Langmuir, 1998. **15**(2): p. 419-428.
64. Georgiadis, A., et al., *Interfacial Tension Measurements and Modelling of (Carbon Dioxide + n-Alkane) and (Carbon Dioxide + Water) Binary Mixtures at Elevated Pressures and Temperatures.* J. Supercrit. Fluids, 2010. **55**(2): p. 743-754.
65. Apostolos Georgiadis, F.L., Alexander Bismarck, Felipe J. Blas, Amparo Galindo, Geoffrey C. Maitland, J.P.Martin Trusler, George Jackson, *Interfacial tension measurements and modelling of (carbon dioxide + n-alkane) and (carbon dioxide +water) binary mixtures at elevated pressures and temperatures.* The Journal of Supercritical Fluids, 2010. **55**: p. 743-754.
66. *Subject Index*, in *Studies in Interface Science*, D. MÖbius and R. Miller, Editors. 1998, Elsevier. p. 707-715.
67. Chen, P., et al., *Axisymmetric Drop Shape Analysis (ADSA) and its Applications*, in *Studies in Interface Science*, D. MÖbius and R. Miller, Editors. 1998, Elsevier. p. 61-138.
68. Dukhin, S.S., R. Miller, and G. Loglio, *Physico-chemical hydrodynamics of rising bubble*, in *Studies in Interface Science*, D. MÖbius and R. Miller, Editors. 1998, Elsevier. p. 367-432.
69. Fletcher, P.D.I., *Interactions of emulsion drops*, in *Studies in Interface Science*, D. MÖbius and R. Miller, Editors. 1998, Elsevier. p. 563-592.
70. Gaydos, J., *The Laplace equation of capillarity*, in *Studies in Interface Science*, D. MÖbius and R. Miller, Editors. 1998, Elsevier. p. 1-59.

71. Herold, R., et al., *Pulmonary Surfactant and Biophysical Function*, in *Studies in Interface Science*, D. MÖbius and R. Miller, Editors. 1998, Elsevier. p. 433-474.
72. McMillan, N.D., et al., *From Stalagmometry to multianalyser tensiography: the definition of the instrumental, software and analytical requirements for a new departure in drop analysis*, in *Studies in Interface Science*, D. MÖbius and R. Miller, Editors. 1998, Elsevier. p. 593-705.
73. Miller, R. and V. Fainerman, *The Drop Volume Technique*, in *Studies in Interface Science*, D. MÖbius and R. Miller, Editors. 1998, Elsevier. p. 139-186.
74. Möbius, D. and R. Miller, *Foreword*, in *Studies in Interface Science*, D. MÖbius and R. Miller, Editors. 1998, Elsevier. p. v-ix.
75. Passerone, A. and E. Ricci, *High temperature tensiometry*, in *Studies in Interface Science*, D. MÖbius and R. Miller, Editors. 1998, Elsevier. p. 475-524.
76. Wantke, K.D. and H. Fruhner, *The oscillating bubble method*, in *Studies in Interface Science*, D. MÖbius and R. Miller, Editors. 1998, Elsevier. p. 327-365.
77. Bashforth, F., 1819-1912; Adams, John Couch, 1819-1892, *An attempt to test the theories of capillary action by comparing the theoretical and measured forms of drops of fluid. With an explanation of the method of integration employed in constucting the tables which give the theoretical forms of such drops.* Cambridge [Eng.], 1883.
78. Hartland, S., Hartley, Richard W., *Axisymmetric fluid-liquid interfaces: Tables giving the shape of sessile and pendant drops and external menisci, with examples of their use.* Elsevier, Amsterdam 1976.
79. Rotenberg, Y., L. Boruvka, and A.W. Neumann, *Determination of Surface Tension and Contact Angle from the Shapes of Axisymmetric Fluid Interfaces.* J. Colloid Interface Sci., 1983. **93**(1): p. 169-183.
80. Thiessen, D. and K. Man, *Surface Tension Measurement*, in *The Measurement, Instrumentation and Sensors Handbook on CD-ROM*. 1999, CRC Press.
81. Hansen, F.K., *Surface Tension by Image Analysis: Fast and Automatic Measurements of Pendant and Sessile Drops and Bubbles.* Journal of Colloid and Interface Science, 1993. **160**(1): p. 209-217.
82. Hansen, F.K. and G. Rødsrud, *Surface Tension by Pendant Drop : I. A Fast Standard Instrument using Computer Image Analysis.* J. Colloid Interface Sci., 1991. **141**(1): p. 1-9.
83. Fordham, S., *On the Calculation of Surface Tension from Measurements of Pendant Drops.* Proceedings of the Royal Society of London. Series A, Mathematical and Physical Sciences, 1948. **194**(1036): p. 1-16.

84. Hull, T.E., W.H. Enright, and K.R. Jackson, *Runge-Kutta research at Toronto.* Applied Numerical Mathematics, 1996. **22**(1-3): p. 225-236.
85. Gasem, K.A.M., et al., *Equilibrium Phase Compositions, Phase Densities, and Interfacial Tensions for Carbon Dioxide + Hydrocarbon Systems. 5. Carbon Dioxide + n-Tetradecane.* J. Chem. Eng. Data, 1989. **34**(2): p. 191-195.
86. Hsu, J.J.C., N. Nagarajan, and R.L. Robinson, *Equilibrium Phase Compositions, Phase Densities, and Interfacial Tensions for Carbon Dioxide + Hydrocarbon Systems. 1. Carbon Dioxide + n-Butane.* J. Chem. Eng. Data, 1985. **30**(4): p. 485-491.
87. Nagarajan, N., K.A.M. Gasem, and R.L. Robinson, *Equilibrium Phase Compositions, Phase Densities, and Interfacial Tensions for Carbon Dioxide + Hydrocarbon Systems. 6. Carbon Dioxide + n-Butane + n-Decane.* J. Chem. Eng. Data, 1990. **35**(3): p. 228-231.
88. Nagarajan, N. and R.L. Robinson, *Equilibrium Phase Compositions, Phase densities, and Interfacial Tensions for Carbon Dioxide + Hydrocarbon Systems. 2. Carbon Dioxide + n-Decane.* J. Chem. Eng. Data, 1986. **31**(2): p. 168-171.
89. Nagarajan, N. and R.L. Robinson, *Equilibrium Phase Compositions, Phase Densities, and Interfacial Tensions for Carbon Dioxide + Hydrocarbon Systems. 3. CO_2 + Cyclohexane. 4. CO_2 + Benzene.* J. Chem. Eng. Data, 1987. **32**(3): p. 369-371.
90. Yang, D. and Y. Gu, *Interfacial phenomena of the oil–fluid–rock systems in carbon dioxide flooding reservoirs.* In Recent Developments in Colloids & Interface R, 2003. **1**.
91. Nobakht, M., S. Moghadam, and Y. Gu, *Effects of Viscous and Capillary Forces on CO2 Enhanced Oil Recovery under Reservoir Conditions.* Energy & Fuels, 2007. **21**(6): p. 3469-3476.
92. Georgiadis, A., et al., *Interfacial tension measurements and modelling of (carbon dioxide + n-alkane) and (carbon dioxide + water) binary mixtures at elevated pressures and temperatures.* The Journal of Supercritical Fluids, 2010. **55**(2): p. 743-754.
93. Chun, B.-S. and G.T. Wilkinson, *Interfacial tension in high-pressure carbon dioxide mixtures.* Ind Eng Chem Res, 1995. **34**(12): p. 4371-4377.
94. Hebach, A., et al., *Interfacial Tension at Elevated PressuresMeasurements and Correlations in the Water + Carbon Dioxide System.* J. Chem. Eng. Data, 2002. **47**(6): p. 1540-1546.
95. Park, J.-Y., et al., *Effect of a Fluorinated Sodium Bis(2-ethylhexyl) Sulfosuccinate (Aerosol-OT, AOT) Analogue Surfactant on the Interfacial Tension of CO_2 + Water and CO_2 + Ni-Plating Solution in Near- and Supercritical CO_2.* J. Chem. Eng. Data, 2005. **50**(2): p. 299-308.
96. Yang, D.Y., P. Tontiwachwuthikul, and Y.G. Gu, *Interfacial Tensions of the Crude Oil plus Reservoir Brine + CO_2 Systems at Pressures up to 31*

MPa and Temperatures of 27 °C and 58 °C. J. Chem. Eng. Data, 2005. **50**(4): p. 1242-1249.

97. Georgiadis, A., et al., *Interfacial Tension Measurements of the (H_2O + CO_2) System at Elevated Pressures and Temperatures.* J. Chem. Eng. Data, 2010. **55**(10): p. 4168-4175.
98. Bachu, S. and D.B. Bennion, *Interfacial Tension between CO_2, Freshwater, and Brine in the Range of Pressure from (2 to 27) MPa, Temperature from (20 to 125) degrees C, and Water Salinity from (0 to 334 000) mg.L^{-1}.* J. Chem. Eng. Data, 2009. **54**(3): p. 765-775.
99. Bachu, S. and D.B. Bennion, *Dependence of CO_2-Brine Interfacial Tension on Aquifer Pressure, Temperature and Water Salinity*, in *9th International Conference on Greenhouse Gas Control Technologies* J. Gale, H. Herzog, and J. Braitsch, Editors. 2009, Elsevier Science BV: Washington, D.C. p. 3157-3164.
100. Yang, D.Y., P. Tontiwachwuthikul, and Y.G. Gu, *Interfacial Interactions Between Reservoir Brine and CO_2 at high Pressures and elevated Temperatures.* Energy Fuel., 2005. **19**(1): p. 216-223.
101. Park, J.-Y., et al., *Effect of a Fluorinated Sodium Bis(2-ethylhexyl) Sulfosuccinate (Aerosol-OT, AOT) Analogue Surfactant on the Interfacial Tension of CO2 + Water and CO2 + Ni-Plating Solution in Near- and Supercritical CO2.* Journal of Chemical & Engineering Data, 2005. **50**(2): p. 299-308.
102. Hebach, A., et al., *Interfacial Tension at Elevated PressuresMeasurements and Correlations in the Water + Carbon Dioxide System.* Journal of Chemical & Engineering Data, 2002. **47**(6): p. 1540-1546.
103. Aggelopoulos, C.A., et al., *CO_2/$CaCl_2$ Solution Interfacial Tensions under CO_2 Geological Storage Conditions: Influence of Cation Valence on Interfacial Tension.* Adv. Water Resour., 2010. **33**(6): p. 691-697.
104. Chalbaud, C., et al., *Brine/CO_2 Interfacial Properties and Effects on CO_2 Storage in Deep Saline Aquifers.* Oil & Gas Science and Technology, 2010. **65**(4): p. 541-555.
105. Chalbaud, C., et al., *Interfacial Tension Measurements and Wettability Evaluation for Geological CO_2 Storage.* Adv. Water Resour., 2009. **32**(1): p. 98-109.
106. Chiquet, P., et al., *CO_2/water Interfacial Tensions under Pressure and Temperature Conditions of CO_2 Geological Storage.* Energy Convers. Manage., 2007. **48**(3): p. 736-744.
107. Massoudi, R. and A.D. King, *Effect of Pressure on the Surface Tension of Aqueous Solutions. Adsorption of Hydrocarbon Gases, Carbon Dioxide, and Nitrous Oxide on Aqueous Solutions of Sodium Chloride and Tetrabutylammonium Bromide at 25.deg.* J. Phys. Chem., 1975. **79**(16): p. 1670-1675.

108. Ali, K., H. Anwar ul, et al, *Concentration and Temperature Dependence of Surface Parameters of Some Aqueous Salt Solutions.* Colloids Surf. Physicochem. Eng. Aspects, 2006. **272**(1-2): p. 105-110.
109. Johansson, K.a.J.C.E., *γ and dγ/dT Measurements on Aqueous Solutions of 1,1-electrolytes.* J. Colloid Interface Sci., 1974. **49**(3): p. 469-480.
110. Michaels, A.S. and E.A. Hauser, *Interfacial Tension at Elevated Pressure and Temperature. II. Interfacial Properties of Hydrocarbon–Water Systems.* J. Phys. Chem., 1951. **55**(3): p. 408-421.
111. Harvey, R.R., *The Effect of Pressure on the Interfacial Tension of the Benzene-Water System.* J. Phys. Chem., 1958. **62**(3): p. 322-324.
112. Cai, B.-Y., J.-T. Yang, and T.-M. Guo, *Interfacial Tension of Hydrocarbon + Water/Brine Systems under High Pressure.* J. Chem. Eng. Data, 1996. **41**(3): p. 493-496.
113. Wiegand, G. and E.U. Franck, *Interfacial Tension between Water and non-Polar Fluids up to 473 K and 2800 bar.* Berichte der Bunsengesellschaft für physikalische Chemie, 1994. **98**(6): p. 809-817.
114. Susnar, S.S., H.A. Hamza, and A.W. Neumann, *Pressure-Dependence of Interfacial-Tension of Hydrocarbon Water-Systems Using Axisymmetrical Drop Shape-Analysis.* Colloids and Surfaces a-Physicochemical and Engineering Aspects, 1994. **89**(2-3): p. 169-180.
115. Gaonkar, A.G., *Effects of Salt, Temperature, and Surfactants on the Interfacial-Tension Behavior of a Vegetable Oil-Water System.* J. Colloid Interface Sci., 1992. **149**(1): p. 256-260.
116. Aveyard, R., et al., *Interfacial-Tension Minima in Oil + Water + Surfactant Systems - Effects of Salt and Temperature in Systems Containing Non-Ionic Surfactants.* Journal of the Chemical Society-Faraday Transactions I, 1985. **81**: p. 2155-2168.
117. Bartell, F.E. and F.L. Miller, *A Methold for the Measurement of Interfacial Tension of Liquid-Liquid System.* J. Am. Chem. Soc., 1928. **50**(7): p. 1961-1967.
118. Bartell, F.E. and F.L. Miller, *Displacement of Crude Oil and Benzene from Silica by Aqueous Solutions.* Industrial & Engineering Chemistry, 1932. **24**(3): p. 335-338.
119. Co, C.R.H.H.O.a.R., *Interfacial Tension between Water and Oil under Reservoir Conditions* Petroleum Transactions, AIME, 1939. **132**: p. 184-190.
120. Freer, E.M., et al., *Interfacial Rheology of Globular and Flexible Proteins at the Hexadecane/Water Interface: Comparison of Shear and Dilatation Deformation.* J. Phys. Chem. B, 2004. **108**(12): p. 3835-3844.
121. Ghannam, M.T., *Experimental Investigation of Dynamic Interfacial Tension of Crude Oil - Different Aqueous Solutions.* J. Adhes. Sci. Technol., 2008. **41**(2008): p. 121-129.

122. Good, R.J., *Contact Angle, Wetting and Adhesion - a Critical Review* J. Adhes. Sci. Technol., 1993. **7**(9): p. 1015-1015.
123. Chau, T.T., et al., *A Review of Factors that Affect Contact Angle and Implications for Flotation Practice.* Adv. Colloid Interface Sci., 2009. **150**(2): p. 106-115.
124. Krishnan, A., et al., *An Evaluation of Methods for Contact Angle Measurement.* Colloids Surf. B. Biointerfaces, 2005. **43**(2): p. 95-98.
125. Rao, D.N., *Measurements of dynamic contact angles in solid-liquid-liquid systems at elevated pressures and temperatures.* Colloids and Surfaces a-Physicochemical and Engineering Aspects, 2002. **206**(1-3): p. 203-216.
126. Xie, X. and N.R. Morrow, *Contact Angles on Quartz induced by Adsorption of Heteropolar Hydrocarbons.* J. Adhes. Sci. Technol., 1999. **13**(10): p. 1119-1135.
127. Xie, X. and N.R. Morrow, *Contact Angles on Quartz induced by Adsorption of Heteropolar Hydrocarbons*. Apparent and Microscopic Contact Angles, ed. J. Drelich, J.S. Laskowski, and K.L. Mittal. 2000. 129-145.
128. Xie, X., N.R. Morrow, and J.S. Buckley, *Contact Angle Hysteresis and the Stability of Wetting Changes induced by Adsorption from Crude Oil.* J. Pet. Sci. Eng., 2002. **33**(1-3): p. 147-159.
129. Rao, D.N., *The concept, characterization, concerns and consequences of contact angles in solid-liquid-liquid systems*. Contact Angle, Wettability and Adhesion, Vol 3, ed. K.L. Mittal. 2003. 191-210.
130. Shedid, S.A. and M.T. Ghannam, *Factors Affecting Contact-Angle Measurement of Reservoir Rocks.* J. Pet. Sci. Eng., 2004. **44**(3-4): p. 193-203.
131. Shedid, S.A. and M.T. Ghannam, *Influences of Droplet Volume on Contact Angle of Reservoir Rocks.* Energy Sources, 2005. **27**(11): p. 1085-1097.
132. Standal, S., et al., *Effect of Polar Organic Components on Wettability as Studied by Adsorption and Contact Angles.* J. Pet. Sci. Eng., 1999. **24**(2-4): p. 131-144.
133. Rao, D.N. and R.S. Karyampudi, *Application of the dual-drop dual-crystal contact angle technique to characterize heavy oil reservoir wettability.* Journal of Adhesion Science and Technology, 2002. **16**(5): p. 579-596.
134. Heneghan, J. and R.D. Wilson, *The use of Dynamic Contact Angle Measurement to Assess NAPL Wetting Hysteresis*, in *Gq10: Groundwater Quality Management in a Rapidly Changing World*, M. Schirmer, E. Hoehn, and T. Vogt, Editors. 2011. p. 148-151.

135. Rodriguez-Valverde, M.A., et al., *Contact Angle Measurements on two (Wood and Stone) non-Ideal Surfaces.* Colloids and Surfaces a-Physicochemical and Engineering Aspects, 2002. **206**(1-3): p. 485-495.
136. Keller, D.S. and P. Luner, *Surface Energetics of Calcium Carbonate Powders by Inverse Gas Chromatography (IGC) and Cleaved Crystals by Contact Angle Measurement*. Fundamentals of Papermaking Materials, Vol 2, ed. C.F. Baker. 1997. 911-953.
137. Gomari, K.A.R., et al., *Study of the Effect of Acidic Species on Wettability Alteration of Calcite Surfaces by Measuring Partitioning Coefficients, IFT and Contact Angles*. Contact Angle, Wettability and Adhesion, Vol 4, ed. K.L. Mittal. 2006. 351-367.
138. Hansen, G., A.A. Hamouda, and R. Denoyel, *The Effect of Pressure on Contact Angles and Wettability in the Mica/Water/n-Decane System and the Calcite Plus Stearic Acid/Water/n-Decane System.* Colloids and Surfaces a-Physicochemical and Engineering Aspects, 2000. **172**(1-3): p. 7-16.
139. Amott, E., *Observations Relating to the Wettability of Porous Rock*. 1959.
140. Boneau, D.F. and R.L. Clampitt, *A Surfactant System for the Oil-Wet Sandstone Of the North Burbank Unit.* SPE Journal of Petroleum Technology, 1977. **29**(5): p. 501-506.
141. Donaldson, E.C., R.D. Thomas, and P.B. Lorenz, *Wettability Determination and Its Effect on Recovery Efficiency*. 1969.
142. Looyestijn, W.J. and J. Hofman, *Wettability-Index Determination by Nuclear Magnetic Resonance.* SPE Reservoir Evaluation & Engineering, 2006(04): p. pp. 146-153.
143. Allen, M.P. and D.J. Tildesley, *Computer Simulation of Liquids*. 1989: Oxford University Press, USA.
144. Frenkel, D. and B. Smit, *Understanding Molecular Simulation: From Algorithms to Applications*. 2002: Elsevier Science.
145. Rapaport, D.C., *The Art of Molecular Dynamics Simulation*. 2004: Cambridge University Press.
146. Fowler, R.H., *A Tentative Statistical Theory of Macleod's Equation for Surface Tension, and the Parachor.* Proceedings of the Royal Society of London. Series A, Mathematical and Physical Sciences, 1937. **159**(897): p. 229-246.
147. Harris, J.G., *Liquid-Vapor Interfaces of Alkane Oligomers: Structure and Thermodynamics from Molecular Dynamics Simulations of Chemically Realistic Models.* J. Phys. Chem., 1992. **96**(12): p. 5077-5086.
148. Kirkwood, J.G. and F.P. Buff, *The Statistical Mechanical Theory of Surface Tension.* J. Chem. Phys., 1949. **17**(3): p. 338-343.

149. Alejandre, J., D.J. Tildesley, and G.A. Chapela, *Molecular Dynamics Simulation of the Orthobaric Densities and Surface Tension of Water.* J. Chem. Phys., 1995. **102**(11): p. 4574-4583.
150. Kuznetsova, T. and B. Kvamme, *Thermodynamic Properties and Interfacial Tension of a Model Water-Carbon Dioxide System.* PCCP, 2002. **4**(6): p. 937-941.
151. Smith, W., *Modern Optical Engineering: the Design of Optical Systems*. 2008: McGraw Hill.
152. Chan, C.K., N.Y. Liang, and W.C. Liu, *Measurement of the Shape of a Liquid-Liquid Interface by the Method of Light-Reflection.* Rev. Sci. Instrum., 1993. **64**(3): p. 632-637.
153. Thomas, L.P., et al., *Droplet Profiles Obtained from the Intensity Distribution of Refraction Patterns.* Appl. Opt., 1995. **34**(25): p. 5840-5848.
154. Rutten, H., et al., *Telescope Optics: Evaluation and Design*. 1988: Willmann-Bell.
155. Fordham, S., *On the Calculation of Surface Tension from Measurements of Pendant Drops.* Proc. R. Soc. London, A, 1948. **194**(1036): p. 1-16.
156. Pallas, N.R. and Y. Harrison, *An automated drop shape apparatus and the surface tension of pure water.* Colloids Surf., 1990. **43**(2): p. 169-194.
157. Hoorfar, M. and A. W. Neumann, *Recent progress in Axisymmetric Drop Shape Analysis (ADSA).* Adv. Colloid Interface Sci., 2006. **121**(1-3): p. 25-49.
158. Jasper, J.J., et al., *Interfacial tensions against water of some C_{10}-C_{15} hydrocarbons with aromatic or cycloaliphatic rings.* J. Phys. Chem., 1970. **74**(7): p. 1535-1539.
159. Hebach, A., A. Oberhof, and N. Dahmen, *Density of Water + Carbon Dioxide at Elevated Pressures: Measurements and Correlation.* J. Chem. Eng. Data, 2004. **49**(4): p. 950-953.
160. Duan, Z.H., et al., *An improved model for the calculation of CO2 solubility in aqueous solutions containing Na+, K+, Ca2+, Mg2+, Cl-, and SO42-.* Mar. Chem., 2006. **98**(2-4): p. 131-139.
161. Pruess, K. and N. Spycher, *ECO2N - A fluid property module for the TOUGH2 code for studies of CO2 storage in saline aquifers.* Energy Conv. Mgmt, 2007. **48**(6): p. 1761-1767.
162. Al Ghafri, S., Maitland, G. C., Trusler, J. P. M., (to be published).
163. Span, R. and W. Wagner, *A new equation of state for carbon dioxide covering the fluid region from the triple-point temperature to 1100 K at pressures up to 800 MPa.* J. Phys. Chem. Ref. Data, 1996. **25**(6): p. 1509-1596.
164. Tewes, F. and F. Boury, *Thermodynamic and Dynamic Interfacial Properties of Binary Carbon Dioxide−Water Systems.* J. Phys. Chem. B, 2004. **108**(7): p. 2405-2412.

165. Aggelopoulos, C.A., M. Robin, and O. Vizika, *Interfacial Tension Between CO_2 and Brine (NaCl + $CaCl_2$) at Elevated Pressures and Temperatures: The Additive Effect of Different Salts.* Adv. Water Resour., 2011.
166. Li, X., et al., *Interfacial tension of (brines + CO_2). I. (0.864 NaCl + 0.136 KCl) at temperatures between (298 and 448) K, pressures between (2 and 50) MPa, and total molalities of (1 to 5) mol·kg^{-1}.* J. Chem. Eng. Data, 2012. DOI 10.1021/je201062r.
167. Johansson, K. and J.C. Eriksson, *Determination of dγ/dT for Water by means of a Differential Technique.* J. Colloid Interface Sci., 1972. **40**(3): p. 398-405.
168. Leroy, P., et al., *Predicting the Surface Tension of Aqueous 1:1 Electrolyte Solutions at High Salinity.* Geochim. Cosmochim. Acta, 2010. **74**(19): p. 5427-5442.
169. Ralston, J. and T.W. Healy, *Specific Cation Effects on Water Structure at the Air-Water and Air-Octadecanol Monolayer-Water Interfaces.* J. Colloid Interface Sci., 1973. **42**(3): p. 629-644.
170. Weissenborn, P.K. and R.J. Pugh, *Surface Tension of Aqueous Solutions of Electrolytes: Relationship with Ion Hydration, Oxygen Solubility, and Bubble Coalescence.* J. Colloid Interface Sci., 1996. **184**(2): p. 550-563.
171. Shu-Xin Hou, G.C.M., and J. P. Martin Trusler, *Measurement and Modeling of the Phase Behavior of the (Carbon Dioxide + Water) Mixture at Temperatures From 298.15 K to 448.15 K.* Journal of Supercritical Fluids. In review.
172. Li, X., et al., *Interfacial Tension of (Brines + CO_2): (0.864 NaCl + 0.136 KCl) at Temperatures between (298 and 448) K, Pressures between (2 and 50) MPa, and Total Molalities of (1 to 5) mol·kg^{-1}.* J. Chem. Eng. Data, 2012. **57**(4): p. 1078-1088.
173. Li, X., et al., *Interfacial Tension of (Brines + CO_2): $CaCl_2$(aq), $MgCl_2$(aq), and Na_2SO_4(aq) at Temperatures between (343 and 423) K, Pressures between (2 and 50) MPa, and Molalities of (0.5 to 5) mol·kg^{-1}.* J. Chem. Eng. Data, 2012. **57**(5): p. 1369-1375.
174. Kvamme, B., et al., *Measurements and Modelling of Interfacial Tension for Water+Carbon Dioxide Systems at Elevated Pressures.* Computational Materials Science, 2007. **38**(3): p. 506-513.
175. M. In Het Panhuis C. H. Patterson R. M, L.-B., *A Molecular Dynamics Study of Carbon Dioxide in Water: Diffusion, Structure and Thermodynamics.* Mol. Phys., 1998. **94**(6): p. 963-972.
176. Nieto-Draghi, C., et al., *Thermodynamic and Transport Properties of Carbon Dioxide from Molecular Simulation.* J. Chem. Phys., 2007. **126**(6): p. 064509-8.
177. Zhang, Z. and Z. Duan, *An Optimized Molecular Potential for Carbon Dioxide.* J. Chem. Phys., 2005. **122**(21): p. 214507-15.

178. Chen, F., *Simulated Surface Tensions of Common Water Models.* J. Chem. Phys., 2007. **126**(22): p. 221101.
179. Nielsen, L.C., I.C. Bourg, and G. Sposito, *Predicting CO_2–Water Interfacial Tension under Pressure and Temperature Conditions of Geologic CO_2 Storage.* Geochim. Cosmochim. Acta, 2012. **81**(0): p. 28-38.
180. Berendsen, H.J.C., J.R. Grigera, and T.P. Straatsma, *The Missing Term in Effective Pair Potentials.* J. Phys. Chem., 1987. **91**(24): p. 6269-6271.
181. Abascal, J.L.F. and C. Vega, *A General Purpose Model for the Condensed Phases of Water: TIP4P/2005.* J. Chem. Phys., 2005. **123**(23): p. 234505-12.
182. Da Rocha, S.R.P., et al., *Molecular Structure of the Water–Supercritical CO2 Interface.* J. Phys. Chem. B, 2001. **105**(48): p. 12092-12104.
183. Harris, J.G. and K.H. Yung, *Carbon Dioxide's Liquid-Vapor Coexistence Curve And Critical Properties as Predicted by a Simple Molecular Model.* J. Phys. Chem., 1995. **99**(31): p. 12021-12024.
184. Tegze, G., et al., *Multiscale approach to CO_2 hydrate formation in aqueous solution: Phase field theory and molecular dynamics. Nucleation and growth.* J. Chem. Phys., 2006. **124**(23): p. 234710-12.
185. Wasserman, E., B. Wood, and J. Brodhol, *The Static Dielectric Constant of Water at Pressures up to 20 kbar and Temperatures to 1273 K: Experiment, Simulations, and Empirical Equations.* Geochim. Cosmochim. Acta, 1995. **59**(1): p. 1-6.
186. Duan, Z. and Z. Zhang, *Equation of state of the H_2O, CO_2, and H_2O–CO_2 systems up to 10 GPa and 2573.15 K: Molecular dynamics simulations with ab initio potential surface.* Geochim. Cosmochim. Acta, 2006. **70**(9): p. 2311-2324.
187. Vega, C. and E. de Miguel, *Surface Tension of the most Popular Models of Water by using the Test-Area Simulation Method.* J. Chem. Phys., 2007. **126**(15): p. 154707-10.
188. Jorgensen, W.L., D.S. Maxwell, and J. Tirado-Rives, *Development and Testing of the OPLS All-Atom Force Field on Conformational Energetics and Properties of Organic Liquids.* J. Am. Chem. Soc., 1996. **118**(45): p. 11225-11236.
189. Matsumoto, M. and Y. Kataoka, *Molecular Orientation Near Liquid--Vapor Interface of Methanol: Simulational Study.* J. Chem. Phys., 1989. **90**(4): p. 2398-2407.
190. Lemmon, E., M.L. Huber, and M.O. McLinden, *NIST Standard Reference Database 23: Reference Fluid Thermodynamic and Transport Properties - REFPROP*. 2010.
191. Duan, Z. and R. Sun, *An improved Model Calculating CO_2 Solubility in Pure Water and Aqueous NaCl Solutions from 273 to 533 K and from 0 to 2000 bar.* Chem. Geol., 2003. **193**(3–4): p. 257-271.

192. http://www.kruss.de/en/home.html.
193. Rezaei Gomari, K.A. and A.A. Hamouda, *Effect of Fatty Acids, Water Composition and pH on the Wettability Alteration of Calcite Surface.* J. Pet. Sci. Eng., 2006. **50**(2): p. 140-150.
194. Zhang, P., M.T. Tweheyo, and T. Austad, *Wettability alteration and improved oil recovery by spontaneous imbibition of seawater into chalk: Impact of the potential determining ions Ca^{2+}, Mg^{2+}, and SO_4^{2-}.* Colloids Surf. Physicochem. Eng. Aspects, 2007. **301**(1–3): p. 199-208.
195. Austad, T., et al., *Seawater in Chalk: An EOR and Compaction Fluid.* SPE Reservoir Evaluation & Engineering, 2008(08): p. pp. 648-654.
196. Chukwudeme, E.A. and A.A. Hamouda, *Oil Recovery from Polar Components (asphaltene and SA) Treated Chalk Rocks by Low Salinity Water and Water Containing SO_4^{2-} and Mg_2^{+} at Different Temperatures.* Colloids Surf. Physicochem. Eng. Aspects, 2009. **336**(1–3): p. 174-182.
197. Ahadian, S. and Y. Kawazoe, *Evaluation of the Cox Equation to Derive Dynamic Contact Angle at Nanopores Imbibition: A Molecular Dynamics Study.* Materials Transactions, 2009. **50**(5): p. 1157-1160.
198. Fei, K., C.P. Chiu, and C.W. Hong, *Molecular Dynamics Prediction of Nanofluidic Contact Angle offset by an AFM.* Microfluid. Nanofluid., 2008. **4**(4): p. 321-330.
199. Hong, S.D., M.Y. Ha, and S. Balachandar, *Static and Dynamic Contact Angles of Water Droplet on a Solid Surface using Molecular Dynamics Simulation.* J. Colloid Interface Sci., 2009. **339**(1): p. 187-195.
200. Koishi, T., et al., *Measurement of Contact-Angle Hysteresis for Droplets on Nanopillared Surface and in the Cassie and Wenzel States: A Molecular Dynamics Simulation Study.* Acs Nano, 2011. **5**(9): p. 6834-6842.
201. Nijmeijer, M.J.P., et al., *A Visual Measurement of Contact Angles in a Molecular-Dynamics Simulation.* Physica A, 1989. **160**(2): p. 166-180.
202. Ohler, B. and W. Langel, *Molecular Dynamics Simulations on the Interface between Titanium Dioxide and Water Droplets: A New Model for the Contact Angle.* Journal of Physical Chemistry C, 2009. **113**(23): p. 10189-10197.
203. Sergi, D., G. Scocchi, and A. Ortona, *Molecular Dynamics Simulations of the Contact Angle between Water Droplets and Graphite Surfaces.* Fluid Phase Equilib., 2012. **332**: p. 173-177.
204. Shi, B. and V.K. Dhir, *Molecular Dynamics Simulation of the Contact Angle of Liquids on Solid Surfaces.* J. Chem. Phys., 2009. **130**(3).
205. Weijs, J.H., J.H. Snoeijer, and D. Lohse, *Formation of Surface Nanobubbles and the Universality of Their Contact Angles: A Molecular Dynamics Approach.* Phys. Rev. Lett., 2012. **108**(10).

206. Werder, T., et al., *Molecular Dynamics Simulation of Contact Angles of Water Droplets in Carbon Nanotubes.* Nano Lett., 2001. **1**(12): p. 697-702.
207. Cooke, D.J., et al., *Interaction of Ethanol and Water with the {10(1)over-bar4} Surface of Calcite.* Langmuir, 2010. **26**(18): p. 14520-14529.
208. Kerisit, S. and S.C. Parker, *Free Energy of Adsorption of Water and Calcium on the {10(1)/-4} Calcite Surface.* Chem. Commun., 2004(1): p. 52-53.
209. Kerisit, S. and S.C. Parker, *Free Energy of Adsorption of Molecules and Ions at the Calcite-Water Interface.* Geochim. Cosmochim. Acta, 2005. **69**(10): p. A481-A481.
210. Kerisit, S., S.C. Parker, and J.H. Harding, *Atomistic Simulation of the Dissociative Adsorption of Water on Calcite Surfaces.* J. Phys. Chem. B, 2003. **107**(31): p. 7676-7682.
211. Liang, Y., et al., *Dissolution Kinetics at the Calcite-Water Interface.* Geochim. Cosmochim. Acta, 1996. **60**(23): p. 4883-4887.
212. Raiteri, P., et al., *Derivation of an Accurate Force-Field for Simulating the Growth of Calcium Carbonate from Aqueous Solution: A New Model for the Calcite-Water Interface.* Journal of Physical Chemistry C, 2010. **114**(13): p. 5997-6010.
213. Williford, R.E., et al., *Dissolution and Growth of (10(1)over-bar4) Calcite in Flowing Water: Estimation of Back Reaction Rates via Kinetic Monte Carlo Simulations.* J. Cryst. Growth, 2004. **262**(1-4): p. 503-518.
214. Vandervoort, E. and P. Hartman, *Calculated Interfacial-Tensions for the Calcite Cleavage Rhombohedron and Water.* J. Cryst. Growth, 1988. **89**(4): p. 603-607.
215. Headen, T.F. and E.S. Boek, *Potential of Mean Force Calculation from Molecular Dynamics Simulation of Asphaltene Molecules on a Calcite Surface†.* Energy Fuel., 2010. **25**(2): p. 499-502.
216. Van der Voort, E. and P. Hartman, *Calculated Interfacial Tensions for the Calcite Cleavage Rhombohedron and Water.* J. Cryst. Growth, 1988. **89**(4): p. 603-607.
217. Shuttleworth, R., *The Surface Tension of Solids.* Proceedings of the Physical Society. Section A, 1950. **63**(5): p. 444.
218. Wu, W. and G.H. Nancollas, *Determination of interfacial tension from crystallization and dissolution data: a comparison with other methods.* Adv. Colloid Interface Sci., 1999. **79**: p. 229-279.
219. Shi, B., *Molecular Dynamics Simulation of the Surface Tension and Contact Angle of Argon and Water.* PhD thesis, 2006.
220. Shi, B., S. Sinha, and V.K. Dhir, *Molecular Dynamics Simulation of the Density and Surface Tension of Water by Particle-Particle Particle-Mesh Method.* J. Chem. Phys., 2006. **124**(20): p. 204715-7.

221. Sinha, S., *Molecular Dynamics Simulation of Interfacial Tension and Contact angle of Lennard-Jones Fluid.* PhD thesis, 2004.
222. Guggenheim, E.A., *The thermodynamics of interfaces in systems of several components.* Trans. Faraday Soc., 1940. **36**: p. 397-412.
223. McGuire, P.L., et al., *Low Salinity Oil Recovery: An Exciting New EOR Opportunity for Alaska's North Slope*, in *SPE Western Regional Meeting*. 2005, Society of Petroleum Engineers: Irvine, California.
224. Kristensen, M.R., et al., *Feasibility of an EOR MicroPilot for Low-Salinity Water Flooding*, in *International Petroleum Technology Conference*. 2011, International Petroleum Technology Conference: Bangkok, Thailand.
225. Austad, T., et al., *Conditions for a Low-Salinity Enhanced Oil Recovery (EOR) Effect in Carbonate Oil Reservoirs.* Energy Fuel., 2012. **26**(1): p. 569-575.
226. Graue, A. and M.A. Fernø, *Water Mixing During Spontaneous Imbibition at Different Boundary and Wettability Conditions.* J. Pet. Sci. Eng., 2011. **78**(3–4): p. 586-595.
227. Bradford, S.A., L.M. Abriola, and F.J. Leij, *Wettability Effects on two- and three-Fluid Relative Permeabilities.* J. Contam. Hydrol., 1997. **28**(1–2): p. 171-191.
228. Graue, A., et al., *Systematic Wettability Alteration by Aging Sandstone and Carbonate Rock in Crude Oil.* J. Pet. Sci. Eng., 1999. **24**(2–4): p. 85-97.
229. Wu, S. and A. Firoozabadi, *Effect of Salinity on Wettability Alteration to Intermediate Gas-Wetting.* SPE Reservoir Evaluation and Engineering, 2010(04): p. pp. 228-245.
230. Yadali Jamaloei, B., et al., *The Influence of Pore Wettability on the Microstructure of Residual Oil in Surfactant-Enhanced Water Flooding in Heavy Oil Reservoirs: Implications for Pore-Scale Flow Characterization.* J. Pet. Sci. Eng., 2011. **77**(1): p. 121-134.
231. Rezaeidoust, A., et al., *Smart Water as Wettability Modifier in Carbonate and Sandstone: A Discussion of Similarities/Differences in the Chemical Mechanisms.* Energy Fuel., 2009. **23**(9): p. 4479-4485.
232. Hadia, N.J., et al., *Influence of Crude Oil Components on Recovery by High and Low Salinity Waterflooding.* Energy Fuel., 2012. **26**(7): p. 4328-4335.
233. Fjelde, I., S.M. Asen, and A.V. Omekeh, *Low Salinity Water Flooding Experiments and Interpretation by Simulations*, in *SPE Improved Oil Recovery Symposium*. 2012, Society of Petroleum Engineers: Tulsa, Oklahoma, USA.
234. Hoeiland, S., et al., *The Effect of Crude Oil Acid Fractions on Wettability as Studied by Interfacial Tension and Contact Angles.* J. Pet. Sci. Eng., 2001. **30**(2): p. 91-103.

235. Omekeh, A.V., et al., *Modeling of Ion-Exchange and Solubility in Low Salinity Water Flooding*, in *SPE Improved Oil Recovery Symposium*. 2012, Society of Petroleum Engineers: Tulsa, Oklahoma, USA.
236. Fogden, A., *Effect of Water Salinity and pH on the Wettability of a Model Substrate.* Energy Fuel., 2011. **25**(11): p. 5113-5125.
237. Drummond, C. and J. Israelachvili, *Surface Forces and Wettability.* J. Pet. Sci. Eng., 2002. **33**(1–3): p. 123-133.
238. Drummond, C. and J. Israelachvili, *Fundamental Studies of Crude Oil–Surface Water Interactions and its Relationship to Reservoir Wettability.* J. Pet. Sci. Eng., 2004. **45**(1–2): p. 61-81.
239. Hassenkam, T., et al., *The Low Salinity Effect Observed on Sandstone Model Surfaces.* Colloids Surf. Physicochem. Eng. Aspects, 2012. **403**(0): p. 79-86.
240. Jerauld, G.R., et al., *Modeling Low-Salinity Waterflooding.* SPE Reservoir Evaluation & Engineering, 2008. **11**(6): p. 1000-1012.
241. Tripathi, I. and K.K. Mohanty, *Instability due to Wettability Alteration in Displacements through Porous Media.* Chem. Eng. Sci., 2008. **63**(21): p. 5366-5374.
242. Wu, Y.-S. and B. Bai, *Efficient Simulation for Low Salinity Waterflooding in Porous and Fractured Reservoirs*, in *SPE Reservoir Simulation Symposium*. 2009, Society of Petroleum Engineers: The Woodlands, Texas.
243. Morrow, N. and J. Buckley, *Improved Oil Recovery by Low-Salinity Waterflooding.* SPE Journal of Petroleum Technology, 2011. **63**(5): p. 106-112.
244. Ayirala, S.C., et al., *A Designer Water Process for Offshore Low Salinity and Polymer Flooding Applications*, in *SPE Improved Oil Recovery Symposium*. 2010, Society of Petroleum Engineers: Tulsa, Oklahoma, USA.
245. Alagic, E., et al., *Effect of Crude Oil Ageing on Low Salinity and Low Salinity Surfactant Flooding.* J. Pet. Sci. Eng., 2011. **78**(2): p. 220-227.
246. Alipour Tabrizy, V., R. Denoyel, and A.A. Hamouda, *Characterization of Wettability Alteration of Calcite, Quartz and Kaolinite: Surface Energy Analysis.* Colloids Surf. Physicochem. Eng. Aspects, 2011. **384**(1–3): p. 98-108.

Appendix A

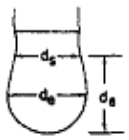

Arithmetic tabulation of H-S function for pendant drops

$$S = \frac{d_s}{d_e} \qquad S \text{ vs. } 1/H \qquad \gamma = \frac{(\rho_1 - \rho_2)\, g d_e^2}{H}$$

Interpolation is unwarranted

S	0	1	2	3	4	5	6	7	8	9
0.70	0.797	0.795	0.792	0.790	0.787	0.785	0.782	0.780	0.777	0.775
0.71	0.772	0.770	0.767	0.765	0.762	0.759	0.757	0.754	0.752	0.749
0.72	0.747	0.744	0.742	0.739	0.737	0.735	0.732	0.730	0.727	0.725
0.73	0.722	0.720	0.718	0.715	0.713	0.711	0.709	0.706	0.704	0.702
0.74	0.699	0.697	0.695	0.692	0.690	0.688	0.685	0.683	0.681	0.679
0.75	0.676	0.674	0.672	0.670	0.668	0.665	0.663	0.661	0.659	0.657
0.76	0.655	0.652	0.650	0.648	0.646	0.644	0.642	0.640	0.637	0.635
0.77	0.633	0.631	0.629	0.627	0.625	0.623	0.621	0.619	0.617	0.615
0.78	0.613	0.611	0.609	0.607	0.605	0.603	0.601	0.599	0.597	0.595
0.79	0.593	0.591	0.589	0.587	0.585	0.583	0.581	0.579	0.577	0.575
0.80	0.573	0.571	0.570	0.568	0.566	0.564	0.562	0.561	0.559	0.557
0.81	0.555	0.553	0.551	0.550	0.548	0.546	0.544	0.542	0.540	0.539
0.82	0.537	0.535	0.533	0.532	0.530	0.528	0.526	0.524	0.523	0.521
0.83	0.519	0.518	0.516	0.515	0.513	0.511	0.509	0.507	0.506	0.504
0.84	0.502	0.501	0.499	0.498	0.496	0.494	0.493	0.491	0.490	0.488
0.85	0.486	0.485	0.483	0.482	0.480	0.479	0.477	0.476	0.474	0.473
0.86	0.471	0.470	0.468	0.467	0.465	0.464	0.462	0.461	0.459	0.458
0.87	0.457	0.455	0.454	0.452	0.451	0.450	0.448	0.447	0.446	0.444
0.88	0.443	0.441	0.440	0.439	0.437	0.436	0.434	0.433	0.431	0.430
0.89	0.429	0.428	0.426	0.425	0.423	0.422	0.420	0.419	0.418	0.417
0.90	0.415	0.414	0.413	0.411	0.410	0.409	0.408	0.406	0.405	0.404
0.91	0.403	0.401	0.400	0.399	0.398	0.396	0.395	0.394	0.393	0.391
0.92	0.390	0.389	0.388	0.386	0.385	0.384	0.383	0.382	0.381	0.379
0.93	0.378	0.377	0.376	0.375	0.373	0.372	0.371	0.370	0.369	0.368
0.94	0.366	0.365	0.364	0.363	0.362	0.361	0.359	0.358	0.357	0.356
0.95	0.355	0.354	0.353	0.352	0.351	0.350	0.349	0.348	0.346	0.345
0.96	0.344	0.343	0.342	0.341	0.340	0.339	0.338	0.337	0.335	0.334
0.97	0.333	0.332	0.331	0.330	0.329	0.328	0.327	0.326	0.325	0.324
0.98	0.323	0.322	0.321	0.320	0.319	0.318	0.317	0.316	0.315	0.314
0.99	0.313	0.312	0.311	0.310	0.309	0.308	0.307	0.306	0.305	0.304
1.00	0.303									

Appendix B

The variation of interfacial tension with temperature and pressure may be deduced following Guggenheim's analysis[222] in which the interfacial region is treated as a microphase of small but finite thickness. The Gibbs-Duhem equation applied to this surface phase in a two-component system is:

$$-Ad\gamma = S^{\sigma}dT - V^{\sigma}dp + n_1^{\sigma}d\mu_1 + n_2^{\sigma}d\mu_2 \qquad \text{(B.1)}$$

Here, A is the area of the interface, S denotes entropy, V is volume, n_i is the amount of component i, μ_i is the chemical potential of component i and superscript σ denotes properties of the surface phase. Similarly, for the two bulk phases, denotes α and β, we have:

$$0 = S^{\alpha}dT - V^{\alpha}dp + n_1^{\alpha}d\mu_1 + n_2^{\alpha}d\mu_2 \qquad \text{(B.2)}$$

and

$$0 = S^{\beta}dT - V^{\beta}dp + n_1^{\beta}d\mu_1 + n_2^{\beta}d\mu_2 \qquad \text{(B.3)}$$

Combining these equations at constant pressure to eliminate of the chemical potentials, one finds:

$$-Ad\gamma = n^{\sigma}\left[S_{\mathrm{m}}^{\sigma} - \frac{z_1(y_2S_{\mathrm{m}}^{\alpha} - x_2S_{\mathrm{m}}^{\beta}) + z_2(x_1S_{\mathrm{m}}^{\beta} - y_1S_{\mathrm{m}}^{\alpha})}{x_1y_2 - y_1x_2}\right]dT \qquad \text{(B.4)}$$

where x_i, y_i and z_i denote mole fractions of component i in phases α, β and σ respectively, subscript m denotes molar properties, and n^{σ} is the total amount of substance in the surface phase. When the two components are only sparingly soluble in each other, we have (assuming α to be the phase rich in component 1) $x_1 \approx y_2 \approx 1$ and hence $x_2 \approx 0$ and $y_1 \approx 0$ so that

$$(\partial\gamma/\partial T)_p = -(n^\sigma/A)(S_m^\sigma - z_1 S_1 - z_2 S_2) \quad \text{(B.5)}$$

where S_1 and S_2 are the molar entropies of the pure components 1 and 2 at the temperature and pressure of the system. Similarly, for the variation with pressure, one finds

$$(\partial\gamma/\partial p)_T = (n^\sigma/A)(V_m^\sigma - z_1 V_1 - z_2 V_2) \quad \text{(B.6)}$$

where V_1 and V_2 are the molar volume of the pure components 1 and 2. Thus, $-(\partial\gamma/\partial T)_p$ is proportional to the excess molar entropy of the surface phase, while $(\partial\gamma/\partial p)_T$ is proportional to the excess molar volume of the surface phase

Appendix C

Risk assessment

Hazard	Details	Probability	Control measures
Over pressure	Failure of windows Main vessel explosion Failure of Valves/fittings Failure in CO_2 Bottle/regulator	Medium Low Low Low	Safety margin; safety head burst disc; barricade; away for sources of ignition; regulator checked regularly; high pressure warnings signage
Over temperature	Leakage/splashing of hot fluids Exposed hot surfaces	Low Medium	Fluid discharge into closed container; high temperature warning signage
Gas bottle falling object	Personal damage Gas leak Piping and regulator damaged	Low Low Low	Bottle restrained on the bench
Electrical	Shock	low	Socket raised above floor level; regular PAT testing
Hazardous substances: CO_2 and brines	CO_2 asphyxiation at high concentrations Brines: Health warnings (eye and skin contact, ingestion)	Low Low	See COSHH assessment
Manual handling CO_2 bottle	Bad lifting techniques	Low	Handling of gas bottle following Manual Handling Regulations 1992; use a trolley; valves closed; pigtails and regulator disconnected

Appendix D

Table 16. Major IFT component with their operating limits

No.	Components	Manufacturer / material	Ref. Number	Limits (*T*/K, *p*/MPa)
C1	Optical Cell	Sitec / HC276; sapphire	740.2225-1	473K, 50MPa
	Reducers 1/4HP-1/16LHP	Sitec / HC276	625.2321-HC276	100 MPa
	Safety Head Body	Sitec / HC276	720.5432-2-HC276	100 MPa
	Safety Head Burst disc			60 MPa
V1 V2	Type 2 LHP Valve	Sitec / HC276	610.3220-HC276	100 MPa
	Tee 1/16 LHP	Sitec / HC276	620.1323-HC276	100 MPa
	Tee 1/4	Sitec / HC276	720.1433-1-276	200 MPa
	Plug 1/4 HP	Sitec / HC276	720.0330-HC276	
P1, P2, P3	Quizix Pump	Strata Technology Ltd/HC276	Q28418	293 K, 68 MPa
V4	5-way Ball Valve	Swagelok/Stainless steel	SS-43ZFS2	338 K, 17 MPa
V3, V5, V6	3-Way Ball Valve	Swagelok/Stainless steel	SS-41GXS2	420 K, 17 MPa
T	Temperature Sensor	Sensing Devices Ltd		473 K
	1/16 Tubing	Hi-Pro / HC276		80 MPa
	1/4 Tubing	Staffordshire hydraulic services / HC276		80 MPa
	1/8 Tubing	Polyflon/PTFE		298 K, 2.8 MPa

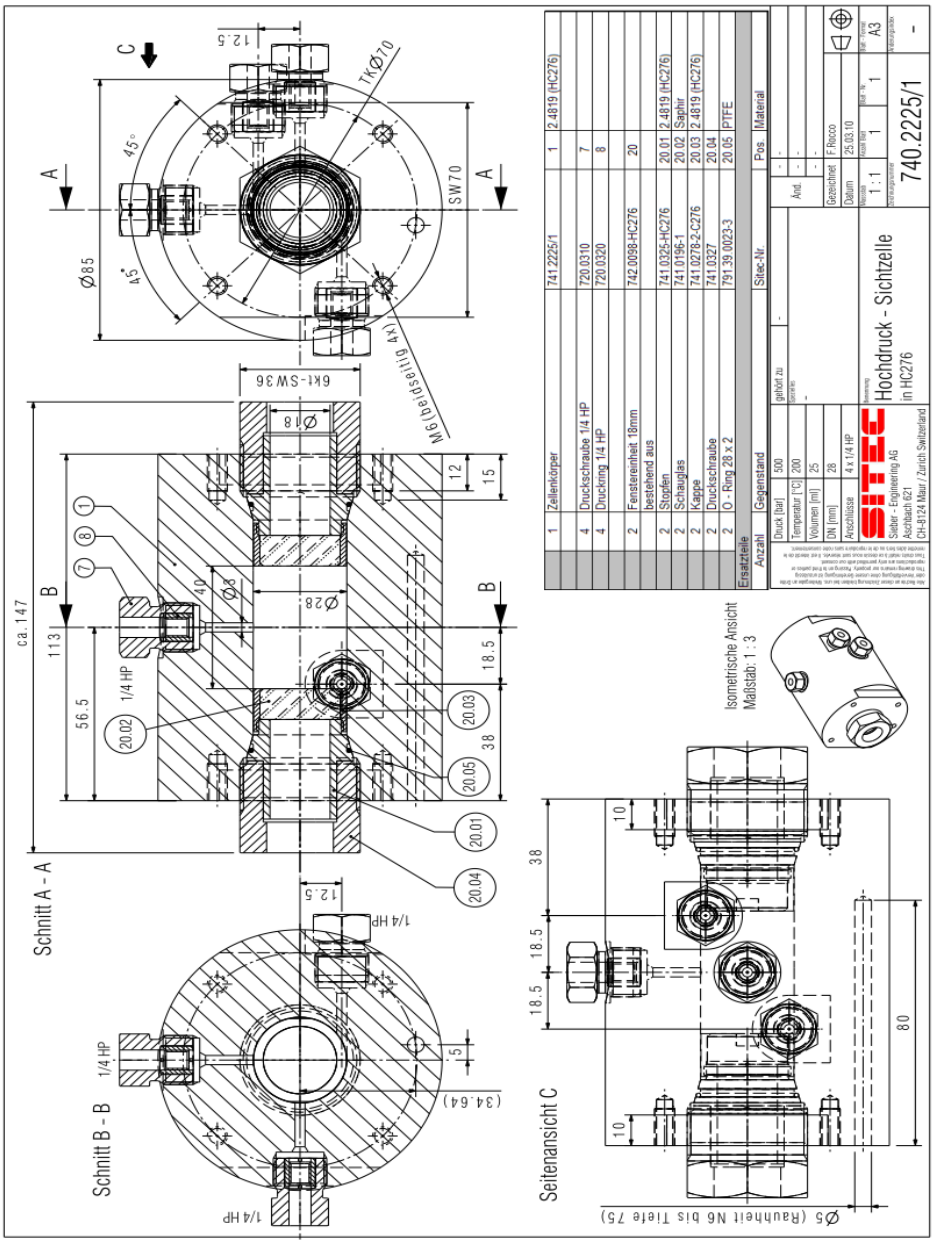
Schnitt A - A
Schnitt B - B
Seitenansicht C
Isometrische Ansicht
Maßstab: 1 : 3
Hochdruck - Sichtzelle
in HC276
740.2225/1
Sitec-Nr.
Material
Gegenstand
Ersatzteile
Zellenkörper
Druckschraube 1/4 HP
Druckring 1/4 HP
Fenstereinheit 18mm
bestehend aus
Stopfen
Schauglas
Kappe
Druckschraube
O - Ring 28 x 2
PTFE
Saphir
F. Rocco
26.03.10
1 : 1
A3
Sieber - Engineering AG
Aschlacht 621
CH-8124 Maur / Zurich Switzerland

Appendix E

Table 17. Composition of Qatari brine sample 1

SAMPLE 1	Reservoir A		Reservoir B	
Specific gravity at 60/60 ºF	1.022		1.043	
pH at 25 0C	7.500		7.100	
Resistivity @ 75 ºF (ohm-meter)	0.210		0.120	
Total Dissolved Solids (mg/L)	30093.0		56882.0	
Cations	Mg/L	Meq/l	Mg/L	Meq/l
Sodium	8320	361.73	14204	617.55
Calcium	1483	74.15	5109	255.45
Magnesium	316	26.01	1128	92.84
Iron	<1	<.0.10	2	0.072
Barium	ND	ND	ND	ND
Potassium	1574	40.36	800	20.51
Strontium	40	0.91	159	3.63
Anions, Mg/l	Mg/L	Meq/l	Mg/L	Meq/l
Chloride	16632	469.17	33969	958.22
Bicarbonate	315	5.16	258	4.23
Sulphate	1340	27.92	1147	23.9
Carbonate	Zero	Zero	Zero	Zero
Hydroxide	Zero	Zero	Zero	Zero
Single phase compresibility , 1/psi	Not measured		Not measured	
Formation water viscosity , cp	Not measured		Not measured	
Organic acid analysis				
Formate, mg/l	not measured		not measured	
Acetate, mg/l	not measured		not measured	
Oxalate, mg/l	not measured		not measured	
Butyrate, mg/l	not measured		not measured	

Table 18. Composition of Qatari brine sample 2

SAMPLE 2	Reservoir A		Reservoir B	
Specific gravity at 60/60 ºF	1.024		1.019	
pH at 25 0C	7.29		8.48	
Resistivity @ 75 ºF (ohm-meter)	0.262		0.341	
Total Dissolved Solids (mg/L)	31570.0		24970.0	
Cations	Mg/L	Meq/l	Mg/L	Meq/l
Sodium	9930	430	7180	310
Calcium	1200	60	1500	75
Magnesium	425	35	345	28
Iron	N/D	-	N/D	-
Barium	< 0.05	< 0.00	0.23	0.00
Potassium	365	9.3	300	7.6
Strontium	63	1.4	48	1.1
Anions, Mg/l	Mg/L	Meq/l	Mg/L	Meq/l
Chloride	17880	505	13660	385
Bicarbonate	475	7.8	390	6.4
Sulphate	1230	26	1520	32
Carbonate	NIL	NIL	32	1.1
Hydroxide	NIL	NIL	NIL	NIL
Single phase compresibility at 3500 psia /135 F, 1/psi	2.72 E- 06		2.65 E-06	
Formation water viscosity at 3500 psia/ 135 F, cp	0.561		0.490	
Organic acid analysis				
Formate, mg/l	not measured		not measured	
Acetate, mg/l	not measured		not measured	
Oxalate, mg/l	not measured		not measured	
Butyrate, mg/l	not measured		not measured	

Table 19. Composition of Qatari brine sample 3

SAMPLE 3	Reservoir A		Reservoir B	
Specific gravity at 60/60 ºF	1.037		1.082	
pH at 25 0C	6.500		6.200	
Resistivity @ 75 ºF (ohm-meter)	0.136		0.069	
Total Dissolved Solids (mg/L)	48830.0		124335.0	
Cations	Mg/L	Meq/l	Mg/L	Meq/l
Sodium	14177	614.07	33838	1471.87
Calcium	3240	162	10586	529.3
Magnesium	624	51.36	1851	152.35
Iron	0.4	0.01	3	0.11
Barium	ND	ND	ND	ND
Potassium	484	12.41	460	11.79
Strontium	98	2.24	299	6.83
Anions, Mg/l	Mg/L	Meq/l	Mg/L	Meq/l
Chloride	28795	812.27	76113	2147.05
Bicarbonate	277	4.54	170	2.79
Sulphate	1194	24.88	1015	21.15
Carbonate	Zero	Zero	Zero	Zero
Hydroxide	Zero	Zero	Zero	Zero
Single phase compresibility , 1/psi	Not measured		Not measured	
Formation water viscosity , cp	Not measured		Not measured	
Organic acid analysis				
Formate, mg/l	13		15	
Acetate, mg/l	53		1	
Oxalate, mg/l	27		<0.10	
Butyrate, mg/l	0		<0.10	

(The low concentration Qatari brine which measured in this study is the average of 5 low salinity brine samples, and the high concentration Qatari brine is the same as Qatari brine sample 2 from reservoir B.)

Appendix F

Table 20. Interfacial tension γ for CO_2 + (0.864 NaCl + 0.136 KCl)(aq) at temperatures T, pressures p and total salt molality m = 0.98 mol·kg^{-1}.[a]

T K	p MPa	$\Delta\rho$ (kg·m^{-3})	γ (mN·m^{-1})	T K	p MPa	$\Delta\rho$ (kg·m^{-3})	γ (mN·m^{-1})
298.15	2	1008.0	55.3	373.15	2	971.7	55.4
298.15	4	955.4	43.9	373.15	4	941.1	51.0
298.15	6	859.1	32.4	373.15	6	906.1	46.8
298.15	8	274.1	28.8	373.15	8	866.2	43.1
298.15	10	234.3	27.7	373.15	10	820.4	39.7
298.15	12	207.2	27.3	373.15	12	768.4	37.0
298.15	14	186.5	26.7	373.15	14	710.5	34.7
298.15	16	169.5	26.1	373.15	16	649.4	33.6
298.15	18	155.0	25.8	373.15	18	589.5	32.6
298.15	20	142.3	25.7	373.15	20	534.8	31.9
298.15	25	115.8	25.0	373.15	25	429.8	30.5
298.15	30	94.6	23.7	373.15	30	358.6	29.1
298.15	35	76.6	22.2	373.15	35	308.0	28.3
298.15	40	61.3	20.8[b]	373.15	40	268.6	27.6
298.15	45	47.7	20.2[c]	373.15	45	237.5	27.2
298.15	50	35.6	19.3[d]	373.15	50	211.0	26.7
323.15	2	1000.5	59.6	423.15	2	935.9	46.3
323.15	4	958.2	51.7	423.15	4	911.0	43.7
323.15	6	902.9	45.0	423.15	6	884.1	41.2
323.15	8	820.0	39.5	423.15	8	855.3	39.2
323.15	10	655.8	36.9	423.15	10	825.0	37.0
323.15	12	456.4	34.8	423.15	12	792.1	34.7
323.15	14	370.0	33.6	423.15	14	758.0	32.4
323.15	16	321.0	33.1	423.15	16	722.7	30.8
323.15	18	286.9	32.8	423.15	18	686.9	29.0
323.15	20	260.6	32.4	423.15	20	651.5	27.5
323.15	25	213.1	31.6	423.15	25	566.1	25.4
323.15	30	178.9	30.6	423.15	30	493.4	23.9
323.15	35	152.6	30.3	423.15	35	432.7	22.7
323.15	40	130.3	29.2	423.15	40	384.3	21.7
323.15	45	112.1	29.1	423.15	45	343.3	21.2
323.15	50	95.4	29.8[b]	423.15	50	310.0	20.9
343.15	2	988.0	58.2	448.15	2	915.4	42.5
343.15	4	952.4	52.4	448.15	4	892.5	40.7
343.15	6	908.7	46.9	448.15	6	868.3	38.6
343.15	8	853.6	42.1	448.15	8	842.8	36.4
343.15	10	780.9	38.5	448.15	10	816.2	34.6
343.15	12	684.1	36.4	448.15	12	788.1	32.0

343.15	14	574.6	34.9	448.15	14	759.3	29.9
343.15	16	484.6	33.5	448.15	16	729.8	28.1
343.15	18	421.1	32.7	448.15	18	699.9	27.3
343.15	20	375.3	32.3	448.15	20	670.4	26.5
343.15	25	299.9	31.3	448.15	25	597.3	24.5
343.15	30	251.1	30.6	448.15	30	531.9	22.5
343.15	35	215.2	30.0	448.15	35	474.0	20.9
343.15	40	186.8	29.7	448.15	40	425.9	20.2
343.15	45	163.3	29.2	448.15	45	383.9	19.4
343.15	50	143.3	29.3	448.15	50	349.3	18.9

[a] Standard uncertainties u are $u(T)$ = 0.025 K, $u(p)$ = 35 kPa and $u(\gamma)$ = Max(0.008·γ, 0.3 mN·m^{-1}).

[b] $u(\gamma)$ = 0.4 mN·m^{-1}. [c] $u(\gamma)$ = 0.5 mN·m^{-1}. [d] $u(\gamma)$ = 0.6 mN·m^{-1}.

Table 21. Interfacial tension γ for CO_2 + (0.864 NaCl + 0.136 KCl)(aq) at temperatures T, pressures p and total salt molality m = 1.98 mol·kg^{-1}. [a]

T K	p MPa	$\Delta\rho$ (kg·m^{-3})	γ (mN·m^{-1})	T K	p MPa	$\Delta\rho$ (kg·m^{-3})	γ (mN·m^{-1})
323.15	2	1031.6	61.0	373.15	18	620.3	34.4
323.15	4	989.3	53.4	373.15	20	565.2	33.5
323.15	6	933.9	46.5	373.15	25	460.1	32.0
323.15	8	850.8	40.0	373.15	30	388.6	30.8
323.15	10	686.5	37.1	373.15	35	337.9	30.1
323.15	12	487.1	35.4	373.15	40	298.1	29.7
323.15	14	400.6	35.0	373.15	45	267.2	29.1
323.15	16	351.6	34.5	373.15	50	240.2	28.4
323.15	18	317.4	33.7	393.15	2	991.7	54.1
323.15	20	290.9	33.4	393.15	4	963.2	50.5
323.15	25	243.4	32.5	393.15	6	931.7	47.0
323.15	30	208.8	31.9	393.15	8	897.0	43.9
323.15	35	182.6	31.9	393.15	10	858.8	40.8
323.15	40	159.9	30.5	393.15	12	817.2	38.5
323.15	45	141.8	30.7	393.15	14	772.3	36.5
323.15	50	124.7	29.8	393.15	16	725.2	35.1
343.15	2	1020.3	59.2	393.15	18	677.5	33.8
343.15	4	984.2	53.3	393.15	20	631.0	32.7
343.15	6	940.2	48.5	393.15	25	529.2	30.7
343.15	8	884.8	43.8	393.15	30	452.0	29.5
343.15	10	811.9	40.2	393.15	35	394.1	28.7
343.15	12	715.0	37.9	393.15	40	349.1	27.9
343.15	14	605.3	36.8	393.15	45	312.8	27.5
343.15	16	515.1	35.6	393.15	50	282.7	27.0
343.15	18	451.6	34.8	423.15	2	970.2	48.9
343.15	20	405.8	34.2	423.15	4	944.8	45.5
343.15	25	330.1	33.1	423.15	6	917.5	43.1
343.15	30	281.2	31.9	423.15	8	888.3	41.1
343.15	35	245.2	31.2	423.15	10	857.9	38.8
343.15	40	216.7	30.9	423.15	12	824.4	36.8
343.15	45	193.1	30.3	423.15	14	790.1	35.0
343.15	50	173.0	29.9	423.15	16	754.5	34.0
373.15	2	1004.4	57.0	423.15	18	718.4	32.0
373.15	4	973.3	52.4	423.15	20	683.3	30.8
373.15	6	938.1	48.3	423.15	25	596.9	28.7
373.15	8	897.9	44.6	423.15	30	524.2	27.4
373.15	10	851.7	41.5	423.15	35	462.7	26.2
373.15	12	799.7	38.9	423.15	40	414.4	25.4
373.15	14	741.6	37.0	423.15	45	372.6	24.8
373.15	16	680.3	35.6	423.15	50	339.5	24.3

[a] Standard uncertainties u are $u(T) = 0.025$ K, $u(p) = 35$ kPa and $u(\gamma) = \text{Max}(0.008 \cdot \gamma, 0.3\ \text{mN} \cdot \text{m}^{-1})$.

Table 22. Interfacial tension γ for CO_2 + (0.864 NaCl + 0.136 KCl)(aq) at temperatures T, pressures p and total salt molality m = 2.97 mol·kg^{-1}. [a]

T K	p MPa	$\Delta\rho$ (kg·m^{-3})	γ (mN·m^{-1})	T K	p MPa	$\Delta\rho$ (kg·m^{-3})	γ (mN·m^{-1})
298.15	2	1078.0	62.0	373.15	2	1043.3	58.2
298.15	4	1025.2	51.0	373.15	4	1011.8	53.5
298.15	6	928.7	38.5	373.15	6	976.3	48.7
298.15	8	343.4	35.3	373.15	8	935.9	45.4
298.15	10	303.7	34.7	373.15	10	889.4	42.5
298.15	12	276.2	34.3	373.15	12	837.3	40.3
298.15	14	255.3	34.1	373.15	14	779.1	38.2
298.15	16	238.1	33.9	373.15	16	717.7	36.7
298.15	18	223.3	34.0	373.15	18	657.5	35.2
298.15	20	210.8	34.0	373.15	20	602.2	34.7
298.15	25	183.5	33.2	373.15	25	497.0	33.7
298.15	30	162.2	32.6	373.15	30	425.0	32.3
298.15	35	143.6	31.7	373.15	35	374.5	31.2
298.15	40	128.0	32.3	373.15	40	334.2	30.6
298.15	45	113.8	31.6	373.15	45	303.4	30.1
298.15	50	101.6	30.8	373.15	50	275.9	29.6
323.15	2	1069.2	63.5	393.15	2	1031.1	56.2
323.15	4	1026.8	54.9	393.15	4	1002.2	52.7
323.15	6	971.3	48.0	393.15	6	970.4	49.4
323.15	8	888.2	41.5	393.15	8	935.5	46.2
323.15	10	723.8	38.5	393.15	10	897.1	43.3
323.15	12	524.4	37.7	393.15	12	855.2	40.7
323.15	14	437.8	36.6	393.15	14	810.1	38.7
323.15	16	388.7	35.8	393.15	16	762.9	37.2
323.15	18	354.5	35.8	393.15	18	715.0	35.7
323.15	20	327.8	35.5	393.15	20	668.3	34.6
323.15	25	280.3	34.8	393.15	25	566.3	32.3
323.15	30	245.3	33.5	393.15	30	488.8	30.9
323.15	35	219.2	32.9	393.15	35	430.6	30.3
323.15	40	196.0	32.7	393.15	40	385.4	29.5
323.15	45	178.2	32.1	393.15	45	349.0	28.8
323.15	50	160.5	31.5	393.15	50	318.7	28.3
343.15	2	1058.8	62.2	423.15	2	1010.9	51.6
343.15	4	1022.3	56.7	423.15	4	985.1	48.5
343.15	6	978.0	51.3	423.15	6	957.5	45.8
343.15	8	922.4	43.8	423.15	8	927.9	43.5
343.15	10	849.3	40.8	423.15	10	897.6	41.1
343.15	12	752.3	39.0	423.15	12	863.5	39.1
343.15	14	642.4	37.9	423.15	14	828.8	37.4
343.15	16	552.2	36.6	423.15	16	793.1	35.8
343.15	18	488.6	36.2	423.15	18	756.8	34.4

343.15	20	442.7	35.7	423.15	20	721.8	33.5
343.15	25	366.9	34.8	423.15	25	634.6	31.5
343.15	30	317.9	34.1	423.15	30	562.0	30.1
343.15	35	281.8	33.4	423.15	35	499.6	28.9
343.15	40	253.2	33.0	423.15	40	451.6	28.1
343.15	45	229.5	32.4	423.15	45	408.8	27.3
343.15	50	209.3	32.2	423.15	50	376.2	26.9

[a] Standard uncertainties u are $u(T) = 0.025$ K, $u(p) = 35$ kPa and $u(\gamma) = \mathrm{Max}(0.008 \cdot \gamma, 0.3\ \mathrm{mN \cdot m^{-1}})$.

Table 23. Interfacial tension γ for CO_2 + (0.864 NaCl + 0.136 KCl)(aq) at temperatures T, pressures p and total salt molality m = 4.95 mol·kg^{-1}. [a]

T K	p MPa	$\Delta\rho$ (kg·m^{-3})	γ (mN·m^{-1})	T K	p MPa	$\Delta\rho$ (kg·m^{-3})	γ (mN·m^{-1})
323.15	2	1117.5	65.8	373.15	2	1092.8	61.3
323.15	4	1075.0	57.2	373.15	4	1061.0	57.8
323.15	6	1019.4	50.7	373.15	6	1025.1	53.2
323.15	8	936.2	44.8	373.15	8	984.5	49.4
323.15	10	771.6	41.8	373.15	10	937.6	46.1
323.15	12	572.2	40.1	373.15	12	885.5	43.9
323.15	14	485.5	39.3	373.15	14	827.1	42.1
323.15	16	436.4	38.9	373.15	16	765.6	40.6
323.15	18	402.1	38.4	373.15	18	705.2	39.5
323.15	20	375.2	38.0	373.15	20	649.5	38.0
323.15	25	327.7	37.0	373.15	25	544.4	36.7
323.15	30	292.2	36.6	373.15	30	471.8	35.3
323.15	35	266.3	36.2	373.15	35	421.4	34.8
323.15	40	242.5	35.6	373.15	40	380.6	34.2
323.15	45	225.1	35.4	373.15	45	350.1	33.8
323.15	50	206.6	34.7	373.15	50	321.9	33.2
343.15	2	1107.9	64.9	423.15	2	1062.8	55.7
343.15	4	1070.9	58.6	423.15	4	1036.5	52.4
343.15	6	1026.3	52.9	423.15	6	1008.5	49.8
343.15	8	970.5	47.7	423.15	8	978.6	46.8
343.15	10	897.3	44.3	423.15	10	948.3	44.3
343.15	12	800.1	42.3	423.15	12	913.4	42.6
343.15	14	690.1	40.8	423.15	14	878.5	40.9
343.15	16	599.8	39.7	423.15	16	842.5	39.6
343.15	18	536.1	38.8	423.15	18	805.9	38.2
343.15	20	490.1	38.3	423.15	20	771.3	37.4
343.15	25	414.2	37.2	423.15	25	683.0	35.3
343.15	30	365.0	36.3	423.15	30	610.6	34.0
343.15	35	328.8	35.5	423.15	35	547.1	32.8
343.15	40	300.1	34.8	423.15	40	499.5	31.9
343.15	45	276.3	34.3	423.15	45	455.7	31.5
343.15	50	256.0	33.5	423.15	50	423.6	31.0

[a] Standard uncertainties u are $u(T)$ = 0.025 K, $u(p)$ = 35 kPa and $u(\gamma)$ = Max(0.008·γ, 0.3 mN·m^{-1}).

Table 24. Interfacial tension γ for CO_2 + $CaCl_2$(aq) at temperatures T, pressures p and molality m = 2.5 mol·kg^{-1}.

T	p	$\Delta\rho$	γ	T	p	$\Delta\rho$	γ
K	MPa	(kg·m^{-3})	(mN·m^{-1})	K	MPa	(kg·m^{-3})	(mN·m^{-1})
343.15	2	1134.2	65.7	393.15	2	1108.3	60.6
343.15	4	1096.9	59.6	393.15	4	1078.9	56.9
343.15	6	1052.2	53.6	393.15	6	1046.7	53.5
343.15	8	996.2	48.5	393.15	8	1011.5	49.6
343.15	10	922.9	44.8	393.15	10	972.8	46.9
343.15	12	825.6	42.4	393.15	12	930.7	44.8
343.15	14	715.5	41.3	393.15	14	885.4	42.9
343.15	16	625.2	40.7	393.15	16	838.0	41.4
343.15	18	561.4	40.2	393.15	18	790.0	39.8
343.15	20	515.3	39.7	393.15	20	743.2	38.9
343.15	25	439.2	38.3	393.15	25	640.7	36.6
343.15	30	389.9	37.4	393.15	30	562.9	35.4
343.15	35	353.4	36.9	393.15	35	504.5	34.7
343.15	40	324.5	36.5	393.15	40	459.0	33.8
343.15	45	300.5	35.8	393.15	45	422.2	33.1
343.15	50	279.9	35.2	393.15	50	391.7	32.5
373.15	2	1119.7	62.2	423.15	2	1089.4	55.1
373.15	4	1087.7	58.2	423.15	4	1063.2	52.4
373.15	6	1051.8	54.2	423.15	6	1035.3	49.5
373.15	8	1011.0	50.0	423.15	8	1005.5	47.0
373.15	10	964.6	46.8	423.15	10	973.9	45.2
373.15	12	911.9	44.4	423.15	12	940.6	42.9
373.15	14	853.5	42.5	423.15	14	905.8	41.1
373.15	16	791.9	40.6	423.15	16	869.8	39.8
373.15	18	731.5	39.6	423.15	18	833.3	38.8
373.15	20	676.5	38.9	423.15	20	797.0	37.6
373.15	25	570.5	37.2	423.15	25	710.7	35.0
373.15	30	498.9	36.0	423.15	30	636.3	33.5
373.15	35	447.3	35.1	423.15	35	575.1	32.1
373.15	40	407.6	34.5	423.15	40	525.1	31.1
373.15	45	375.6	34.0	423.15	45	483.9	30.6
373.15	50	349.0	33.5	423.15	50	449.2	29.8

[a] Standard uncertainties u are $u(T)$ = 0.025 K, $u(p)$ = 35 kPa and $u(\gamma) = 0.008 \cdot \gamma$.

Table 25. Interfacial tension γ for CO_2 + $CaCl_2$(aq) at temperatures T, pressures p and molality m = 5.0 mol·kg^{-1}.

T	p	$\Delta\rho$	γ	T	p	$\Delta\rho$	γ
K	MPa	(kg·m^{-3})	(mN·m^{-1})	K	MPa	(kg·m^{-3})	(mN·m^{-1})
343.15	2	1273.9	74.8	393.15	2	1247.3	69.2
343.15	4	1236.3	68.7	393.15	4	1217.6	65.5
343.15	6	1191.2	63.0	393.15	6	1185.1	62.1
343.15	8	1135.0	57.0	393.15	8	1149.5	58.4
343.15	10	1061.4	50.9	393.15	10	1110.6	55.5
343.15	12	964.0	49.9	393.15	12	1068.2	53.0
343.15	14	853.8	49.3	393.15	14	1022.8	50.9
343.15	16	763.2	48.6	393.15	16	975.1	49.5
343.15	18	699.3	48.0	393.15	18	926.9	48.8
343.15	20	653.1	47.2	393.15	20	880.0	48.0
343.15	25	576.7	46.5	393.15	25	777.1	46.2
343.15	30	527.2	45.6	393.15	30	699.0	44.5
343.15	35	490.5	44.5	393.15	35	640.2	43.7
343.15	40	461.4	44.2	393.15	40	594.4	42.9
343.15	45	437.1	43.9	393.15	45	557.4	42.4
343.15	50	416.3	43.6	393.15	50	526.6	42.3
373.15	2	1258.6	72.0	423.15	2	1229.5	64.9
373.15	4	1226.2	67.4	423.15	4	1202.8	62.2
373.15	6	1189.9	63.1	423.15	6	1174.5	58.7
373.15	8	1148.9	58.6	423.15	8	1144.4	54.9
373.15	10	1102.3	55.1	423.15	10	1112.5	52.3
373.15	12	1049.4	52.0	423.15	12	1078.9	50.7
373.15	14	990.7	50.5	423.15	14	1043.8	49.1
373.15	16	929.0	49.4	423.15	16	1007.7	48.2
373.15	18	868.5	48.9	423.15	18	970.9	47.4
373.15	20	813.3	48.2	423.15	20	934.4	46.7
373.15	25	707.0	46.6	423.15	25	847.6	44.9
373.15	30	635.1	45.5	423.15	30	772.8	43.4
373.15	35	583.2	44.8	423.15	35	711.2	42.4
373.15	40	543.2	44.2	423.15	40	660.9	41.6
373.15	45	511.0	43.1	423.15	45	619.3	41.1
373.15	50	484.1	42.4	423.15	50	584.2	40.8

[a] Standard uncertainties u are $u(T)$ = 0.025 K, $u(p)$ = 35 kPa and $u(\gamma) = 0.008 \cdot \gamma$.

Table 26. Interfacial tension γ for CO_2 + $MgCl_2$(aq) at temperatures T, pressures p and molality m = 2.5 mol·kg^{-1}.

T	p	$\Delta\rho$	γ	T	p	$\Delta\rho$	γ
K	MPa	(kg·m^{-3})	(mN·m^{-1})	K	MPa	(kg·m^{-3})	(mN·m^{-1})
343.15	2	1112.3	65.5	393.15	2	1090.5	60.6
343.15	4	1074.8	59.6	393.15	4	1060.7	56.9
343.15	6	1030.3	53.9	393.15	6	1028.9	53.3
343.15	8	974.3	49.3	393.15	8	993.6	50.3
343.15	10	901.0	45.5	393.15	10	954.9	47.2
343.15	12	803.6	42.9	393.15	12	912.8	44.5
343.15	14	693.6	41.6	393.15	14	867.5	42.5
343.15	16	603.1	40.7	393.15	16	820.0	40.7
343.15	18	539.3	39.7	393.15	18	771.9	39.4
343.15	20	493.2	39.3	393.15	20	725.1	38.4
343.15	25	417.0	38.2	393.15	25	622.5	36.1
343.15	30	367.6	37.2	393.15	30	544.7	35.4
343.15	35	331.1	36.7	393.15	35	486.2	34.0
343.15	40	302.1	36.1	393.15	40	440.6	33.4
343.15	45	278.0	35.7	393.15	45	403.8	33.1
343.15	50	257.4	35.1	393.15	50	373.2	32.2
373.15	2	1100.3	62.5	423.15	2	1074.1	55.9
373.15	4	1068.0	58.5	423.15	4	1047.5	53.0
373.15	6	1032.3	54.3	423.15	6	1019.8	50.6
373.15	8	991.5	50.4	423.15	8	990.0	47.9
373.15	10	945.1	47.3	423.15	10	958.4	45.0
373.15	12	892.4	43.9	423.15	12	925.1	42.9
373.15	14	833.9	41.7	423.15	14	890.2	41.1
373.15	16	772.3	40.2	423.15	16	854.3	39.3
373.15	18	711.9	38.9	423.15	18	817.8	38.1
373.15	20	656.9	38.1	423.15	20	781.4	37.0
373.15	25	550.7	37.2	423.15	25	695.0	35.3
373.15	30	479.0	35.3	423.15	30	620.5	33.6
373.15	35	427.3	34.4	423.15	35	559.2	32.2
373.15	40	387.6	34.1	423.15	40	509.2	31.5
373.15	45	355.6	33.4	423.15	45	467.8	30.8
373.15	50	328.9	32.9	423.15	50	433.0	30.1

[a] Standard uncertainties u are $u(T)$ = 0.025 K, $u(p)$ = 35 kPa and $u(\gamma) = 0.008 \cdot \gamma$.

Table 27. Interfacial tension γ for CO_2 + $MgCl_2$(aq) at temperatures T, pressures p and molality m = 5.0 mol·kg^{-1}.

T K	p MPa	$\Delta\rho$ (kg·m^{-3})	γ (mN·m^{-1})	T K	p MPa	$\Delta\rho$ (kg·m^{-3})	γ (mN·m^{-1})
343.15	2	1247.2	76.1	343.15	18	671.9	48.4
343.15	4	1209.5	69.9	343.15	20	625.6	47.5
343.15	6	1164.3	60.6	343.15	25	549.0	46.1
343.15	8	1108.0	56.7	343.15	30	499.3	45.2
343.15	10	1034.4	51.3	343.15	35	462.4	44.4
343.15	12	936.8	50.0	343.15	40	433.1	44.2
343.15	14	826.6	49.6	343.15	45	408.6	44.1
343.15	16	735.9	48.6	343.15	50	387.6	43.6

[a] Standard uncertainties u are $u(T)$ = 0.025 K, $u(p)$ = 35 kPa and $u(\gamma)$ = 0.008·γ.

Table 28. Interfacial tension γ for CO_2 + Na_2SO_4(aq) at temperatures T, pressures p and molality m = 0.49 mol·kg^{-1}.

T K	p MPa	$\Delta\rho$ (kg·m^{-3})	γ (mN·m^{-1})	T K	p MPa	$\Delta\rho$ (kg·m^{-3})	γ (mN·m^{-1})
373.15	2	993.3	54.6	373.15	18	610.4	33.1
373.15	4	962.3	49.7	373.15	20	555.8	32.2
373.15	6	927.3	45.8	373.15	25	450.5	31.0
373.15	8	887.3	40.1	373.15	30	379.7	28.9
373.15	10	841.5	37.5	373.15	35	328.8	28.9
373.15	12	789.4	37.1	373.15	40	289.8	27.8
373.15	14	731.5	35.6	373.15	45	258.5	27.4
373.15	16	670.3	34.3	373.15	50	232.5	27.0

[a] Standard uncertainties u are $u(T)$ = 0.025 K, $u(p)$ = 35 kPa and $u(\gamma)$ = 0.008·γ.

Table 29. Interfacial tension γ for CO_2 + Na_2SO_4(aq) at temperatures T, pressures p and molality m = 0.98 mol·kg^{-1}.

T K	p MPa	$\Delta\rho$ (kg·m^{-3})	γ (mN·m^{-1})	T K	p MPa	$\Delta\rho$ (kg·m^{-3})	γ (mN·m^{-1})
343.15	2	1057.2	60.6	343.15	10	848.1	39.0
343.15	4	1020.7	54.1	343.15	12	751.1	36.7
343.15	6	976.5	47.8	343.15	14	641.4	36.2
343.15	8	921.0	42.2	343.15	16	551.3	35.3

[a] Standard uncertainties u are $u(T)$ = 0.025 K, $u(p)$ = 35 kPa and $u(\gamma)$ = 0.008·γ.

Table 30. Interfacial tension γ for CO_2 + $NaHCO_3$(aq) at temperatures T, pressures p and molality m = 0.98 mol·kg^{-1}.

T / K	p / MPa	$\Delta\rho$ / (kg·m^{-3})	γ / (mN·m^{-1})	T / K	p / MPa	$\Delta\rho$ / (kg·m^{-3})	γ / (mN·m^{-1})
343.15	2	1033.4	59.9	393.15	2	1007.6	54.0
343.15	4	995.9	53.6	393.15	4	977.9	50.4
343.15	6	951.0	46.0	393.15	6	945.6	46.7
343.15	8	894.9	38.8	393.15	8	910.1	43.0
343.15	10	821.4	35.8	393.15	10	871.3	40.4
343.15	12	724.0	35.5	393.15	12	829.1	38.1
343.15	14	613.9	35.4	393.15	14	783.7	36.5
343.15	16	523.5	34.8	393.15	16	736.2	35.0
343.15	18	459.7	34.2	393.15	18	688.0	33.1
343.15	20	413.6	33.5	393.15	20	641.2	32.3
343.15	25	337.4	33.1	393.15	25	538.6	30.6
343.15	30	288.1	32.8	393.15	30	460.7	29.8
343.15	35	251.6	32.7	393.15	35	402.2	28.6
343.15	40	222.7	32.5	393.15	40	356.6	27.8
343.15	45	198.6	32.2	393.15	45	319.8	27.5
343.15	50	178.1	32.0	393.15	50	289.3	26.9
373.15	2	1019.0	57.1	423.15	2	988.7	49.7
373.15	4	986.8	52.3	423.15	4	962.2	46.6
373.15	6	950.6	47.5	423.15	6	934.0	44.0
373.15	8	909.7	43.3	423.15	8	904.0	40.8
373.15	10	863.1	39.9	423.15	10	872.3	38.5
373.15	12	810.3	37.9	423.15	12	838.8	36.7
373.15	14	751.8	36.7	423.15	14	803.8	35.1
373.15	16	690.1	35.1	423.15	16	767.7	33.5
373.15	18	629.7	34.4	423.15	18	731.2	32.2
373.15	20	574.7	33.8	423.15	20	694.7	30.7
373.15	25	468.5	32.4	423.15	25	608.2	28.5
373.15	30	396.9	31.1	423.15	30	533.7	27.2
373.15	35	345.2	30.7	423.15	35	472.3	25.9
373.15	40	305.5	30.2	423.15	40	422.3	25.1
373.15	45	273.5	29.8	423.15	45	381.0	24.6
373.15	50	246.8	29.6	423.15	50	346.2	23.9

[a] Standard uncertainties u are $u(T)$ = 0.025 K, $u(p)$ = 35 kPa and $u(\gamma)$ = 0.008·γ.

Table 31. Interfacial tension γ for CO_2 + Qatar brine low at temperatures T and pressures p.

T K	p MPa	$\Delta\rho$ (kg·m^{-3})	γ (mN·m^{-1})	T K	p MPa	$\Delta\rho$ (kg·m^{-3})	γ (mN·m^{-1})
343	2	963.4	56.8	393	2	934.3	50.6
343	10	752.0	35.8	393	10	798.9	37.4
343	20	344.9	30.5	393	20	569.6	29.2
343	30	220.1	27.9	393	30	390.1	25.9
343	40	155.3	26.9	393	40	286.8	24.0

[a] Standard uncertainties u are $u(T)$ = 0.025 K, $u(p)$ = 35 kPa and $u(\gamma)$ = 0.008·γ.

Table 32. Interfacial tension γ for CO_2 + Qatar brine high at temperatures T and pressures p.

T K	p MPa	$\Delta\rho$ (kg·m^{-3})	γ (mN·m^{-1})	T K	p MPa	$\Delta\rho$ (kg·m^{-3})	γ (mN·m^{-1})
343	2	1030.2	60.1	393	2	1002.5	54.1
343	10	818.5	39.0	393	10	866.6	40.9
343	20	411.0	33.2	393	20	636.9	32.6
343	30	285.7	31.7	393	30	456.9	29.4
343	40	220.6	30.5	393	35	398.6	28.5
				393	40	353.2	27.7

[a] Standard uncertainties u are $u(T)$ = 0.025 K, $u(p)$ = 35 kPa and $u(\gamma)$ = 0.008·γ.

Table 33. Interfacial tension γ for CO_2 + NaCl(aq) at temperatures T, pressures p and molality m = 1.0 mol·kg^{-1}.

T / K	p / MPa	$\Delta\rho$ / (kg·m^{-3})	γ / (mN·m^{-1})	T / K	p / MPa	$\Delta\rho$ / (kg·m^{-3})	γ / (mN·m^{-1})
473	2	890.2	38.1	473	20	664.3	24.4
473	4	867.7	37.1	473	30	539.2	20.0
473	6	844.3	34.3	473	40	437.4	17.3
473	10	795.3	30.9				

[a] Standard uncertainties u are $u(T)$ = 0.025 K, $u(p)$ = 35 kPa and $u(\gamma)$ = 0.008·γ.

Appendix G

Sample holder for HPHT contact angle measurement

IFT apparatus can be used for these measurements, by placing the substrate into the high pressure cell. Without firmed support, rock samples don't stay immovably when fluid is injected into the cell. Considering two different densities conditions will occur on the drop phase, heavier or lighter than the bulk phase, the holders of the substrates made from PEEK were designed in two ways. See Figure 81 and Figure 82.

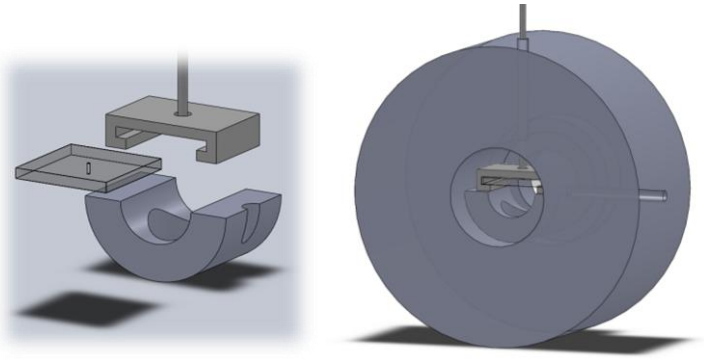

Figure 81. Mineral holders for contact angle measurement for lighter drops

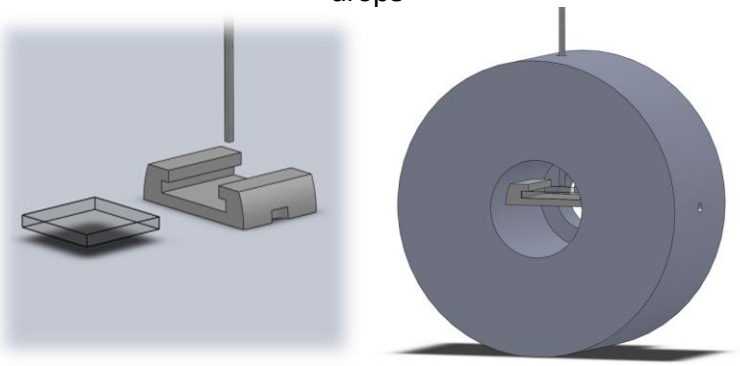

Figure 82. Mineral holders for contact angle measurement for heavier drops

Appendix H

Configuration of the DSA100S

Dosing	Software-controlled single direct dosing system
Camera	Standard camera *61 fps (780×580 px) respectively* *311 fps (780×60 px)*
Optics	Manual zoom / focus
Illumination	Software controlled illumination
Axis	One manual z-axis Two manual x/y-axis with 100 mm movement range
Stage	Standard stage
Software	Software to determine static and dynamic contact angles Software to determine surface free energy of solids

Technical Data of the DSA100S

Max. sample size (WxDxH)	300 x ∞ x 150 mm (500 x ∞ x 150 mm for the long frame version)
Dimension of sample (LxW)	105 x 105 mm (Ø 300 mm) (500 x 500 mm for the long frame version)
Range of contact angle measurements *	• 0 to 180° • 0.1° resolution
Optics	• 7-fold zoom • FOV 4 -28.13 mm diagonal • Stray light compensation • Integrated focus module • High-performance-vario-field ilumination • Viewing angle alignment without shift of image • Patented construction of the optics
Video systems	• 61 fps (780×580 px), 311 fps (780×60 px) • *2200 fps optional* • Online max. 100 evaluations / second • Video sequences (duration depending on RAM) • Automatic software trigger for evaluation /

	recording
Software	5 different methods of drop shape analysis for Sessile Drop, automatic baseline for contact angle between 0 to 180°, option for curved baseline, video sequence, procedure definition, autodrop delivery, calculation of surface free energy according to Fowkes, extended Fowkes, Wu, Zisman, Owens-Wendt-Rabel, van Oss & Good, Neumann, calculation of Wetting envelopes, etc…
Temperature range	-60 to 400°C
Dimensions (WxDxH)	620 × 380 × 610mm (954 x 380 x 610 for the long frame version)
Weight	25 to 45 kg
Power supply	110 to 240 VAC
Interfaces	Optional connection to USB port of PC via adapter

Appendix I

Technical detail of HP3220LLH unit

Technical Description HP3220LLH

High Pressure View Cell

Max. pressure	50 MPa (7,500 psi)	*higher upon request*
Max. temperature	180°C (350°F)	*higher upon request*
Window material	sapphire	
Window Diameter	18 mm	
Wetted Material	Hastelloy C (C276 or C22 or similar)	*other upon request*
Volume	approx. 25 ml (∅: 28 mm, L: 40 mm)	*other upon request*

Valves and fittings

All valves and tubing are proven high pressure products.

Drop Formation and Pressure Variation Device

Two High Pressure Screw Piston Pumps with a capacity of approx. 30 ml (manual operation) allow variation of pressure and precise generation of a liquid drop. The drop liquid is pressed through a needle either from the top ("pendant drop") or the bottom ("rising bubble") into the view cell. The diameter of the needle can be chosen in accordance with the system specifications, different interchangeable sizes are available.

automatic metering pump upon request

Heating, Measuring

1 Electric heating jacket, 230 VAC/ 50Hz *other upon request*
1 PID controller with temperature sensor, accuracy of indication 1°C
1 Pressure indicator, analogous, max. 60 MPa, accuracy 1% of full scale, division 1 MPa
1 Pressure indicator, analogous, max. 60 MPa, accuracy 1.6% of full scale, division 2 MPa
1 Thermocouple inside view cell, hand held indicator with indication accuracy 0.1°C

High Pressure Fluid (Gas or Liquid) Supply

The view cell may be filled with a liquid and pressurized by the second hand pump included in the apparatus. The system does not include a high pressure pump for filling the view cell with gas, but it is ready for adaptation to a pressurized fluid supply like a gas cylinder or a pump.

A gas pumping system can be offered, according to your needs (media, max. pressure, speed of pressure increase, electric or air driven etc.)

Supporting facility

All equipment is firmly mounted on a stainless steel support. The KRÜSS DSA100 is positioned on top of this support. The approximate size of the steel support is 950 x 650 x 800 mm (L x W x H) and the total weight is approximately 80 kg.

Options, e.g.

HP3280H - Horizontal motion device to move solid samples inside the pressure cell
Other custom-made versions are possible

Technical specifications are subject to change without notice.

Appendix J

Literature review of low salinity water flooding as an EOR technique

Water flooding as a technique for oil recovery has been applied for decades, which increase oil production from a reservoir through the injection of water. But in recent year, increasing oil production by injection of designer water – also known as low salinity water – into a reservoir has recently attracted substantial attention from the oil producing community. It was seen as a highly cost-competitive approach compared to other conventional EOR methods [21]. Reviewing the literature, it can be seen a large amount of paper on low salinity water flooding studies emerged paper since 2007, which reflect the increasing interest of this technique.

Reviewing this researches it can be seen that most of the laboratory tests and field trials have shown that injecting chemically modified water instead of seawater can lead to incremental oil recoveries.

Successful field logs and trials [22, 24, 25, 223] indicate that low salinity water flooding is an economic competitive approach for enhanced oil recovery. These cases included both sandstone reservoir, reported by McGuire *et al*. (2005) [223], a recent successful field trials have led to serious evaluation of field-scale implementation of low salinity EOR. Promising future could be also seen from carbonate reservoir, which reported by Manrique *et al*. (2007) [24], a summary of EOR field experience in carbonate reservoirs in US.

The research by Kristensen *et al*. (2011) [224] indicated that injecting chemically modified water instead of seawater can lead to incremental oil recoveries from both laboratory tests and field trials.

The experiment done by Cissokho *et al*. (2010) [34] suggested that additional oil can be produced by low salinity water flooding on clayed sandstones.

However there are a few cases doesn't show obvious low salinity effect in oil recovery or with more conditions. For instance, the low salinity effect wasn't found from Skreffingland *et al*. (2011) [35]. The measured effect of tertiary lowsal flooding from core experiments in their research was in agreement with the SWCTT. Both measurements indicated only low or no effect from lowsal injection. Their work indicates that the initial wetting condition is a crucial property for the effect of low salinity injection. Two papers published by Austad *et al*. (2010, 2012) [27, 225] concluded that both spontaneous imbibition and forced displacement tests using chalk cores, which were free from sulfate, did not show a low-salinity EOR effect when exposed to diluted seawater. But anhydrite is present in the rock formation, diluted seawater or diluted produced water can act as an EOR injectant to improve recovery over that achieved with high-salinity brines.

It very obvious that most of the low salinity water flooding researches was focused on sandstones [12, 26, 28-33, 43]. Since the most of the sandstones reservoirs are covered by clay, a lot of researches were actually done on clayey sandstone [34, 35], and some of the researches directly investigated the interaction between clay mineral and reservoir fluid [27, 28, 30, 33, 34, 36, 37, 39, 40]. But the study on carbonate reservoir is comparability less.

Most of the laboratory research was done by means of coreflooding experiment. Most of the field research was done by onsite logging. All the researches were trying to find the underling mechanism of low salinity effect.

Graue, A. and M. A. Fernø (2011) [226].have done core flooding experiment on Chalk core, with different boundary conditions

Here temperature plays very important role, which has been studied by Brady, P. V. and J. L. Krumhansl (2012) [36] inverstigated the temperature effect on low salinity water flooding on sandstones.

Al-adasani *et al*. (2012) [33] Sandstone Lowsalinity water flooding summary, 411 coreflooding experiment. Evidence from reservoir simulation that LSWF recovery mechanisms are governed based on the initial and final wetting states.

Most of the researches proposed that low salinity effect is due to the change of reservoir wettability. Bradford *et al*. (1997) [227] have investigated the wettability effect on porous permeabilities of multiphase systems, with a predicting model they claimed that for both two- and three-fluid systems, an increase in the contact angle (measured through water) or organic-wet fraction of a medium will be accompanied by an increase in the water kr and a decrease in the organic kr. In three-fluid media, kr values for water and organic depend on both liquid saturations when the solid is imperfectly wetted. The model assumes that wettability variation has no influence on the air kr. The model assumes that wettability variation has no influence on the air kr. Model predictions are shown to be consistent with available experimental data.

The research by Graue *et al*. (1999)[228] have observed the alteration of wettability on rocks by spontaneous imbibitions with different aging procedure in crude oil.

Field experience has also proofed a wettability alteration by injecting low salinity water. Vledder *et al*. (2010) [25] has summarized this in his paper. This change in wettability is supported by the observation of dual steps in watercut development. In between the two steps the watercut was

constant. This behaviour is a known indicator of changing wettability. Which was also supported by spontaneous imbibition experiments in core material and a single well Log-Inject-Log test in an analogue field.

Wu and Firoozabadi (2010) [229] found that NaCl salinity increases water-wetting when a core is saturated with brine. NaCl also reduces gas absolute permeability, as reported in the literature. $CaCl_2$ salinity effect is dramatically different from that of NaCl brine and has a minor effect on permeability. The NaCl, KCl, and $CaCl_2$ brines have an adverse effect on wettability alteration. To alleviate the effect of salt on chemical treatment, they suggest pretreatment by displacement of brine with water and subsequent drainage by nitrogen.

Yousef *et al*. (2011) [31] after doing coreflooding and NMR experiment, suggested that the key mechanism for low salinity water flooding on carbonate reservoir is wettability alteration.
The influence of wettability on oil recovery has been widely recognized and it was investigated by some researchers, such as Yadali *et al*. (2011) [230] studied the relationship between pore wettability and effectiveness of water flooding.

Rezaei *et al*. (2009) [231] proposed the chemical mechanism behind the wettability alteration in carbonates and sandstones by smart water injection, which refers to the injection of seawater into high temperature chalk reservoirs and low salinity floods in sandstone reservoirs. They suggested that the different chemical bonding mechanisms of polar components from the crude oil onto the positively charged carbonate and the negatively charged quartz/clay indicates a different chemical mechanism for wettability modification by smart water in the two cases.
The coreflooding experiment done by Hadia *et al*. (2012) [232] on sandstone show that different oil components initiate varying wetting conditions and that the initial wetting conditions influence the

performance of a tertiary low salinity flood. In particular, a low salinity flood seems favorable when the initial wetting conditions are not water-wet.

Fjelde *et al*. (2012) [233] also proposed that the low salinity water altered the wetting state of the rock. The direction of alteration can be explained by ion exchange taking place on the clay surface.

Regarding the change of wettability, researchers have proposed different reasons. Both Tweheyo and Hoeiland [42, 234] studied the effect of acid composition in crude oil on wettability. They confirmed that the type of acid composition or pH number has strong influence to the wettability on sandstone and silicate glass.

The research of Tweheyo *et al*. (1999) [42] has related the wettability of sandstones with organic acid and organic base in oil by Amott, USBM and displacement experiment. They found that it is possible to modify the wettability characteristics of the two sandstones from water-wet to neutral-wet, and further to oil-wet, by addition of small amounts of organic acid or organic base to the oil. Wettability indices obtained by the Amott and USBM tests are consistent. Water injection into two composite sandstone cores with fluid systems giving the three different states of wettability mentioned above, responded as expected. The water-wet cores had the highest oil recoveries at water break through. The non-water-wet systems all exhibited a significant tail production of oil. The highest ultimate oil recoveries were obtained for the neutral-wet systems, and the lowest recoveries were given by the oil-wet systems. They said that the change in wettability by addition of organic acids or bases to the oil is likely to be due to adsorption of the additive on the surface of the rock. The mechanism of wettability alteration is thus similar to what can be obtained by the addition of a water-soluble surfactant to the brine. The only difference is that an additional interphase mass transfer step is

involved for the oil-soluble, practically water-insoluble, additive to reach the rock surface by diffusion.

Hoeiland *et al*. (2001) [234] also indicated a correspondence between the decrease in interfacial tension as a function of pH and the acid number of the original crude oils. Observations from both interfacial tension and contact angle experiments emphasize the importance of acid structures, or acid types, present in the fractions compared to the acid concentrations. Fractions enriched in alkyl acids, phenols and cyclic acids were found to have impact on the wetting properties of the silicate surface, whereas fractions enriched in more complicated aromatic ring structures with high degree of carboxylic compounds did not affect the contact angle.

Some authors explained the change of wettability is due to the ions exchange between H^+ in water and cations in the mineral. Austad *et al*. (2010) [27] also investigated the chemical mechanism of low salinity water flooding in sandstone seservoirs. They proposed that at reservoir conditions, the pH of formation water is about 5 due to dissolved acidic gases like CO_2 and H_2S. At this pH, the clay minerals, which act as cation exchange material, are adsorbed by acidic and protonated basic components from the crude oil, and cations, especially divalent cations from the formation water, like Ca^{2+}. Injection of a low saline fluid, which promotes desorption of Ca^{2+}, will create a local increase in pH close to the brine-clay interface because Ca^{2+} is substituted by H^+ from the water. A fast reaction between OH^- and the adsorbed acidic and protonated basic material will cause desorption of organic material from the clay. The water wetness of the rock is improved, and increased oil recovery is observed. To observe low salinity EOR effects in sandstones, a balanced initial adsorption of organic components and Ca^{2+} onto the clay is needed. Both the adsorption capacity and the pH-window for adsorption/desorption of organic material is somewhat different for

various types of clay minerals. A detailed knowledge of the chemical mechanism behind the low saline EOR process together with information on formation brine composition, oil properties and type of clay material present, will make it possible to evaluate the potential for increase in oil recovery by a low salinity water flood.

Similarly, The core flooding test from Nasralla *et al*. (2011) [29, 30] claim that the low salinity effect is an cations exchange, their experiment indicated that injection of deionized water in the secondary mode resulted in a significant improvement in oil recovery, up to 22%, compared to seawater. However, no additional oil was recovered in the tertiary mode. This paper contributes to the understanding of cation exchange caused by low salinity water injection, and how this exchange alters the wettability of the rock and reduces the electrostatic attraction forces bet.

Fjelde *et al*. (2012) [233] also concluded that the ion exchange between clay and brine as the mechanisum of low salinity water flooding. They concluded that the low salinity water altered the wetting state of the rock. The direction of alteration can be explained by ion exchange taking place on the clay surface.

When the formation water was replaced with the low salinity water, increase in the concentrations of divalent cations onto clay surfaces was predicted for the selected brine compositions. Higher concentrations of polar oil components can then be bonded to the clay surfaces by the divalent cations and make them less water-wet.

Omekeh *et al*. (2012) [235] also claimed an ion exchange in low salinity water flooding process. In their experiments, pH was found to increase during the interaction between low-salinity brine and reservoir rocks. The ion composition of the low salinity brine was also found to change due to interaction with the reservoir rocks. The model developed successfully

matched the experimental results. The simulation results show that dissolution of carbonate minerals can occur and this will then alter the composition of the injection water.

The research of Fogden, A. (2012) [40] have done on Koalinite indicated that the oil exhibiting greater surface precipitation was fairly unresponsive to flushing, with displacement of the bulk oil leaving residues substantially lining the kaolinite platelets and filling the pores between them. The oil which adsorbed by electrostatic attraction was more amenable to removal of residues, to partially reinstate the water-wetness of the pristine kaolinite, by flushing with salt solutions which weakened this attraction. In particular, higher salinity of the flush minimized the attractions between oppositely charged sites on the heterogeneous interfaces, and pH shift to higher or lower levels rendered the interfacial charges more similar and mutually repulsive.

Aksulu *et al*. (2012) [32] proposed that the change of pH was a key chemical mechanism for the low-salinity enhanced oil recovery (EOR) effect. The method can be used as a first screening test for possible low-salinity EOR potential.

Interestingly, different ions in low salinity water were found behaving differently from different researches.

Different effect factors on the wettability was investigated by Rezaei Gomari, K. A. and A. A. Hamouda (2006) [193] on Calcite (Island-spar) from India. However he claimed that the presence of SO_4^{2-} increases the water-wetness of calcite, which is different from our experiment observation. The presence of Mg^{2+} and SO_4^{2-} ions is shown to increase the water-wetness of the calcite. Both ions reduce the contact angle. Higher reduction is obtained in presence of SO_4^{2-} compared to Mg^{2+}.

The experimental study on chalk surface, a paper reported by Zhang *et al*. (2007) [194], which investigated three type of ions, Ca^{2+}, Mg^{2+} and SO_4^{2-} and the chalk surface concluded that to improve water wetness, SO_4^{2-} must act together with either Ca^{2+} or Mg^{2+}.

The field experience on chalk reservoir, reported by Austad *et al*. (2008) [195] confirmed that the seawater improves the water wetness of chalk, which increases the oil recovery by spontaneous imbibition and viscous displacement.

However, just the opposite, another research done by Chukwudeme, E. A. and A. A. Hamouda (2009) [196] on chalk found that the presence of SO_4^{2-} in DW is shown to be more effective than that for DW in imbibition experiments at temperatures up to 50 °C, but a large reduction in the potential oil recovery is observed when DW contains Mg2+ is used as an imbibing fluid for cores treated with asphaltene.

Different from the above authors, Fogden (2011) [236] investigated the wettability of silicate substrate by examining adhesion of crude oil on glasses surface with SEM. They found that the contact angles on flooded substrates depended on this residual adhering nanoscale oil and on the ability of bulk oil to adhere by reconnecting to it. Again, the pH dependence of these two factors was opposite. The results suggested a possible supplementary mechanism for enhanced recovery by low salinity flooding.

There are some authors attributed the change of wettability to surface force change between reservoir fluid and rocks.

The fundamental researches were done by Drummond, C. and J. Israelachvili in (2002) and (2004) [237, 238]. They investigated the wettability from an aspect of surface force with surface forces apparatus (SFA) between molecularly smooth mica and crude oil or brine under

different pH and salinity. It was further established that the concept of an intrinsically oil-wet or water-wet surface or reservoir cannot, in general, be correct: depending on the nature of the oil and brine, different species in a crude oil will adsorb on the mineral surfaces and at the oil–water interface, thereby determining the wetting behaviour of a reservoir or rock.

More recently, Hassenkam *et al*. (2011) [239], and they used a new method, atomic force mapping, where functionalised atomic force microscopy (AFM) tips feel a surface, to simulate the interaction between mineral, water and crude oil, under a variety of salinity conditions. We used contact mode AFM to image the internal pore surfaces from fresh outcrop sandstone and from reservoir sandstone that had been cleaned with strong solvents, the traditional treatment method for samples used in core plug testing. Adhesion decrease ranged from 0 to 57% with an average of about 30% when the salinity of brine decreased from 36,500 ppm to 1400 ppm. For most cases, the effect was reversible when the salinity was changed, even through several salinity change cycles, and the effect was consistent on several individual sand grains.

Hassenkam *et al*. (2012) [239] also investiged low salinity effect by atomic force microscopy on sandstones. They research shows that reduced salinities have little or no effect on illite adhesion; there is only a 0–2% change. Adhesion on the fresh, clean muscovite surface varies considerably and the CH3 tip records a 10–20% decrease in response to low salinity solutions. In contrast, the carboxylate tip records a distinct response to salinity decrease, with a 20–30% drop. On a clean SiO2 surface, the low salinity response is evident, reproducible and repeatable through two cycles of high to low salinity changes. The range in decreased adhesion for these model mineral surfaces corresponds well with what is observed for core plug and field tests.

Except atoms force determination, molecular level research was also done by scanning the surface charge, by means of zeta potential technique.

The low salinity effect on aandstone was investigated by Alotaibi, *et al*. (2010-2011) [12, 26, 28, 43] by the study of oil/water/rock interactions at different salinity level and elevated temperature conditions. Wettability is determined by a HTHP contact angle method and zeta potential technique A phase-analysis-light-scattering (PALS) technique was used to determine the zeta potential (surface charge). They claimed that low-salinity water expanded the double-layer thickness and eventually increased the zeta-potential magnitude. As a result of this expansion, it provides a greater opportunity to alter the wettability and enhance oil recovery. This study indicates that clay content in sandstone rocks can significantly alter the wettability either toward water-wet or intermediate. On the basis of the results obtained from this study, it is clear that low-salinity waterflooding can improve oil recovery in the field.

They found that Zeta potential of limestone particles was significantly affected by calcium ion. Low-salinity water created more negative charges on limestone and dolomite particles by expanding the thickness of the diffuse double layer. Individual divalent cations decreased the zeta potential of limestone particles in sodium chloride solutions, while sulfate ions showed a negligible effect. Limestone particles in high-salinity water had decreased zeta potential. The solubility of calcium ions increased as temperature was increased and thus created additional negative charges. The absence of sulfate in aquifer water strongly influenced the dolomite surface charge. In summary, surface-charge adjustment from positive to negative can alter the wettability of carbonate rock from preferentially oil-wet to water-wet. As a result, residual-oil saturation should be decreased.

Just a few authors related the low salinity effect with the change of capillary pressure rather than wettability. The capillary is determined by both the wettability of the solid surface and the interfacial tension between the fluids on certain porous medium.

Idowu *et al*. (2011) [44] seems the first who proposed that claimed that lowering the salinity or TDS of injected water results in lowering the oil-rock capillary pressure, reduction in oil-water interfacial tension, and finally a change in the relative permeability, which results into a wettability change, usually to a mixed-wet or water-wet state, for carbonate reservoirs

Zahid *et al*. (2012) [45] investigated the oil recovery potential of low salinity water flooding for carbonate rocks using both reservoir carbonate and outcrop chalk core plugs. They have took flow rate into account, however no low salinity effect was observed for the reservoir carbonate core plug at the ambient temperature, but increase of the pressure drop over the core plug was detected. On the contrary, a significant increase in oil recovery was observed under low salinity flooding of the reservoir carbonate core plugs at 90 °C. An increase in pressure drop was also observed in this case, possibly related to migration of fines or dissolution reactions. The outcrop Aalborg chalk core plugs did not show any low salinity effect, both at the room and at a high temperature.

Along with the growing interest on low salinity water flooding and some propose on designed water flooding, some of the modelling and reservoir simulations could be found from the literature.

The modelling of low salinity water flooding was done by a few authors. From Jerauld *et al*. (2008) [240], a cconnate-water banking occurs on some degrees. They also saw that the mixing of injected water with in-situ water delays the attainment of low salinity, potentially preventing attainment of low salinity all together if very small slugs of low-salinity

water are used. This could be the reason why low salinity water flooding is not always effective in some filed trails.

Tripathi, I. and K. K. Mohanty (2008) [241] indicated that Low-salinity floods are expected to be mildly unstable due to the low mobility ratio at adverse saturation shocks from their modelling. Wu, Y.-S. and B. Bai (2009) [242] at the mean time developed a reservoir simulator which can be used to quantify low-salinity water flooding processes.

Morrow, N. and J. Buckley (2011) [243] has done a general review of low salinity water flooding with considering connate water.

In practical, the brine salinity for designer water flooding falls within a narrow window of opportunity: when too high, no additional oil production is observed; when too low, clay swelling and/or deflocculation may result in formation damage in the field.
Ayirala *et al*. (2010) [244], Alagic *et al*. (2011) [245], Alipour Tabrizy, V., R. Denoyel, *et al*. (2011) [246] and Cense *et al*. (2011) [37] have proposed different approaches with designed low salinity water flooding by adding surfactant or sepearted water streams to avoid clay-swelling and/or deflocculation, mitigating other critical issues such as reservoir souring and unfavourable wettability modification, and further improve oil recovery.